

Dissertation

# **Probing the Spatial-temporal Properties of the Nuclear Pore Complex**

Graduate School of

Natural Science & Technology

Kanazawa University

Division of Natural System

Student ID No. (1524062013)

Name: **MAHMOUD SHAABAN MOHAMED ABDELRASOUL**

Chief advisor: **Prof. Richard Wong**

Date of Submission: 2018/06/29

# DEDICATION

To the spirit of my father-in-law. And to my father, my mother, my wife and my kids for their continued support prayers, and good wishes. It gave me the strength to persevere and warmed my heart. I particularly dedicate my thesis to my father who inspiring me always. He just does not know how his words and actions have a great impact on me.

# ACKNOWLEDGEMENTS

I would like to thank my supervisor, Prof. Richard Wong, for the guidance, encouragement and advice he has provided throughout my time as his student. I have been extremely lucky to have a supervisor who cared so much about my work, and who responded to my questions and queries so promptly. I strongly thank Dr. Hazawa for preparing shRNA-NUP214 KD cells. Also, I am grateful for Dr. Kobayashi for helping with cell biology experiments and cell preparations. Many Thanks extended for all my lab mates for their support.

*MAHMOUD*

<b>CONTENTS</b>	
<b>Dedication</b>	2
<b>Acknowledgments</b>	3
<b>List of abbreviations</b>	5
<b>General introduction</b>	6
<b>Hypothesis</b>	11
<b>Chapter I: Visualization of the native nuclear pore complex using High Speed Atomic Force Microscopy</b>	12
Abstract	12
Introduction	13
Materials and Methods	14
Results	23
Discussion	43
Conclusions	44
<b>Chapter II: Tracking of intrinsically disordered FG Nups inside the nuclear pore</b>	45
Abstract	45
Introduction	46
Materials and Methods	49
Results	51
Discussion	73
Conclusions	78
<b>References</b>	80

## **LIST OF ABBREVIATIONS**

**NPC:** Nuclear Pore Complex

**Nups:** Nucleoporins

**FG Nups:** phenylalanine-glycine Nucleoporins

**HS-AFM:** High Speed Atomic Force Microscopy

**NE:** Nuclear Envelope

**Nu:** Nucleus

**CRC:** Colorectal Cancer

**NLS:** Nuclear Localization Signal

**NTR:** Nuclear Transport Receptor

**PLL:** Poly-l-Lysine

**EBD:** Electron Beam Depositioning

**PI:** Protease Inhibitor

**FFT:** Fast Fourier Transform

**AML:** Acute Myeloid Leukemia

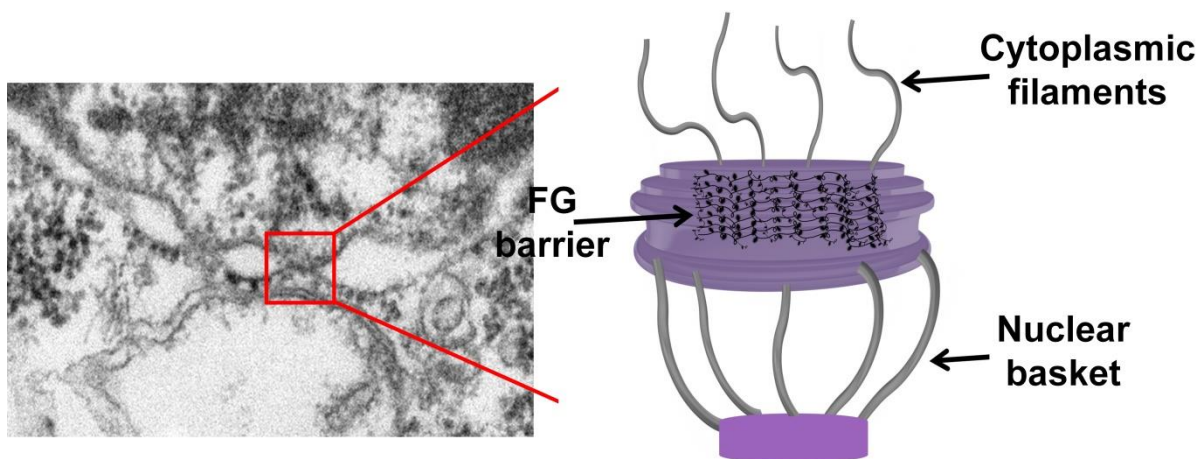
**CP:** Central Plug

## General introduction

### 1. Nuclear pore complex structure

One of the massive protein complexes inside the eukaryotic cell is the nuclear pore complex (NPC) which span the nuclear membrane, which is the double membrane surrounding the nucleus. The proteins that build up the nuclear pore complex are called nucleoporins (Nups) (1).

The NPC easily can be visualized using the electron microscope (EM). Previous EM reports determined eightfold rotational symmetrical structure for the NPC. In addition, the main NPC structure contains rings that are situated on its cytoplasmic and nucleoplasmic faces, giving the NPC a typical twofold symmetry through the nuclear envelope. In addition, NPC contains a structure, like a basket that extends into the nuclear side (the nuclear basket) and filaments that extend into the cytoplasm (known as cytoplasmic filaments), (Figure 1).



**Figure 1. Nuclear pore complex structure.** (a) Schematic diagram of the nuclear pore complex, NPC is anchored to the nuclear membrane by a membrane layer that surrounds the scaffold layer. This scaffold layer provides structure and serves as an anchor for Nups. The central channel exhibits eight-fold rotational symmetry and has eight cytoplasmic filaments as well as eight nuclear filaments protruding into the cytoplasm and nucleoplasm respectively. The nuclear filaments are bound via a ring, resulting in a basket shape.

The single nuclear pore complex has nearly 456 single protein molecules and is consisted of 30 distinct proteins (Nups) (2). Almost half of these Nups have "natively unfolded" or intrinsically disordered sequences, i.e. they are very flexible domains that lack stable tertiary structure (3). These kinds of disordered proteins called the FG nucleoporins (FG Nups), because their amino-acid sequence rich in phenylalanine-glycine repeats (4).

## **2. Nuclear transport**

The small cargoes such as ions and metabolism molecules that have a size below 40 kDa can pass freely via the NPC. However, larger macromolecules such as proteins, viruses and mRNA are not allowed to pass, instead they need to pass by active transport (5).

The transport through nuclear pore complexes is mediated by NTRs such as importins and exportins which can bind with the cargo in order to facilitate its translocation to the nucleus. Each cargo should carry a specific amino acid sequence known as the nuclear localization signal (NLS) (6 - 9).

Previous reports have shown that the translocation process through the pore is very fast which has the properties of first-order kinetics, which occurred at a rate of ~1000 single transport process every second (10). The transport through the pore seems to be random. The directionality of cargo-complex is mainly regulated by the nuclear RanGTP gradient (11, 12).

## **3. The FG flexible barrier**

How can the NPC regulate a barrier while regulating nuclear transport? This question still is a strong a debate in the field (13-17). One thing that is agreed upon is that the regulation of the NPC is done by specific part of Nups, known as FG-Nups. FG-Nups

contain a structured domain that works as an NPC tethering point, from which an unstructured, filamentous region emanates, which contains many (5–10) phenylalanine–glycines (FG)-repeats (18).

Previously, several models have been proposed to explain how the FG-Nups form the transport barrier (19 - 22). Recent study has provided strong evidence for the ‘hydrogel model’ (23, 24). Many FG-repeats can generate a hydrogel, in which the FG-repeats bind cohesively to form a ‘sieve-like network’ with mesh size of ~5 nm. However, this model has unclear parts because it does not explain the interaction between the different FG nucleoporins (25, 26).

#### **4. Dynamic nuclear pore complex**

Previous explanations of the NPC structure as a dynamic complex came from electron microscopy studies whereas the inner channel was observed different states such an opened and closed (27). The closed NPC was known as a central transporter or plug (28). However, major structural changes, might be related to transport status of the NPC. In another study, the cryo-EM results showed that NPC has two different NPC conformational patterns (29). These structures may explain the differences in the composition of Nups from one NPC to another can be related to differential interactions of Nups.

Previous EM results of the structure of NPC have come from reports determining changed distributions of individual Nup domains in different transport conditions (30-32). Other reports have shown that the cytoplasmic filaments are critical for in vitro steady-state importin  $\beta$  nuclear import process (33) and that all the FG domains in the cytoplasmic filaments and nuclear basket Nups can be depleted without significant impact on the import (34-37). Thus, these conformational changes may affect the import process.



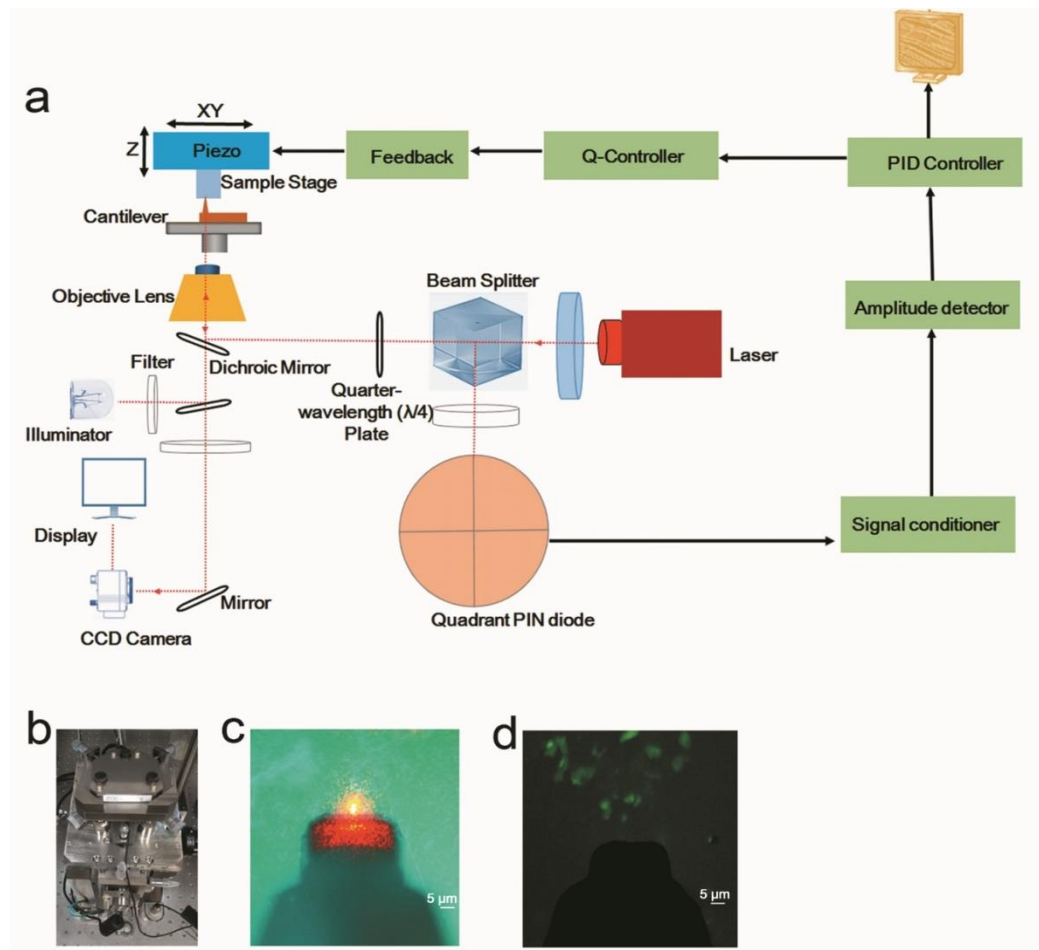
## **5. NPC Nano-dynamics resolving**

To be precise, nucleocytoplasmic transport in vivo happens through NPCs in a scale of microseconds (26, 38, 65). Therefore, only the dynamic spatial-temporal behaviour of FG Nups not the static behaviour that can regulate the NPC barrier. Yet very little is understood about the FG Nup structural dynamics - in time and space terms- due to the lack of techniques that can probe their time-dependent behaviour inside the native NPCs (39). Atomic force microscopy (AFM) can showed beneficial time-lapse observations of native NPCs (40) and also stiffness of the FG network (41-44). However, it is important to keep in mind that the FG Nups themselves still invisible even tagged with GFP.

Many advantages make high-speed AFM (HS-AFM) as strong tool for observing NPCs in the native environment. For example, the stability of tapping during imaging which reduces the forces to the minimum values and this keep the sample intact ([Figure 2](#)) (45-47).

## 6. NPC in cancer and metastasis

Metastasis is the main cause of mortality in many cancers, and all the signalling pathways that regulate it enter the via NPC (49, 50). Rae1 was involved in breast cancer progression (51). Also, Nup98 is an oncogene which upregulated in many leukaemia patients (52-54)



**Figure 2. Fluorescent HS-AFM.** (a) The HS-AFM system combined with a fluorescent CCD camera. (b) HS-AFM stage with a z-piezo scanner. (c) Bright field of the CCD camera showing HCT116 NEs, scale bar, 5 μm. (d) CCD camera display showing GFP-tagged NEs on the glass stage approached by a cantilever tip; scale bar, 5 μm.

## Hypothesis

The spatiotemporal dynamics of mammalian NPCs are not accessible within the previous studies due to technical limits; in the current study I used the HS-AFM to visualize the nano-topo-morphological conformations of native NPCs. Because, HS-AFM can record the individual protein complex dynamics on the nanoscale. Recent study used HS-AFM to visualize the nano-dynamics of NPCs in *Xenopus* eggs. However, NPC dynamics in mammalian and/or cancer cells yet to be revealed. Typically, all the signalling pathways which promote cancer metastasis and progression enter the nucleus through the NPC. Therefore, in the current study, I focused to use human cancer cells as a model to study the native dynamics of NPC. Also, FG barrier in cancer cells expected to possess different dynamic behaviour from *Xenopus*. In addition, previous studies have not reveal the structural dynamic differences between normal and cancer cells on the nano-sclae resolution. So, using the same methodology I compared the main structural differences between normal and cancer colon NPC. This comparison also showed the FG selective barrier of the pore. Furthermore, single FG Nup filaments work inside the NPC central channel in an integral pattern in a very fast and flexible way. However, the visualization of FG Nups in action in their native environments on the single filament scale is unveiled. Therefore, using HS-AFM, I proposed a tentative model for the single FG Nup filaments.

# **Chapter I: Visualization of the native nuclear pore complex using High Speed Atomic Force Microscopy**

## **ABSTRACT**

Nuclear pore complexes (NPCs) are biological nano-machines that mediate the bidirectional transport of macromolecules between the cytoplasm and nucleus. Nearly one-third of nucleoporins consist natively unfolded, intrinsically disordered phenylalanine-glycine repeats (FG-Nups), which mediate the transport process. NPC structure has been well-studied by different electron microscopy based approaches which gave static snapshots to reveal the typical structure. In addition, AFM has been used to visualize the nano-meter measurements of NPC. However, the nano-meter resolution and dynamic recording of NPCs in action in mammalian cells yet to be resolved. In this study, we demonstrated that high-speed atomic force microscopy (HS-AFM) can be a strong tool to directly visualize nano-topographical changes of the nuclear pore in mammalian cells including healthy and cancerous cells. Furthermore, using MLN8237/alisertib, which used as apoptosis and autophagy inducer, we revealed the structural and functional loss of nucleoporins. Therefore, we propose that the loss of this nanoscopic flexibility is an irreversible dying code in colon cancer cells. In addition, I show the native structural conformations of the nuclear basket which showed high flexible motion of its distal ring. Taken together, these data determined the native structural dynamics of nuclear pore complex in mammalian cells.

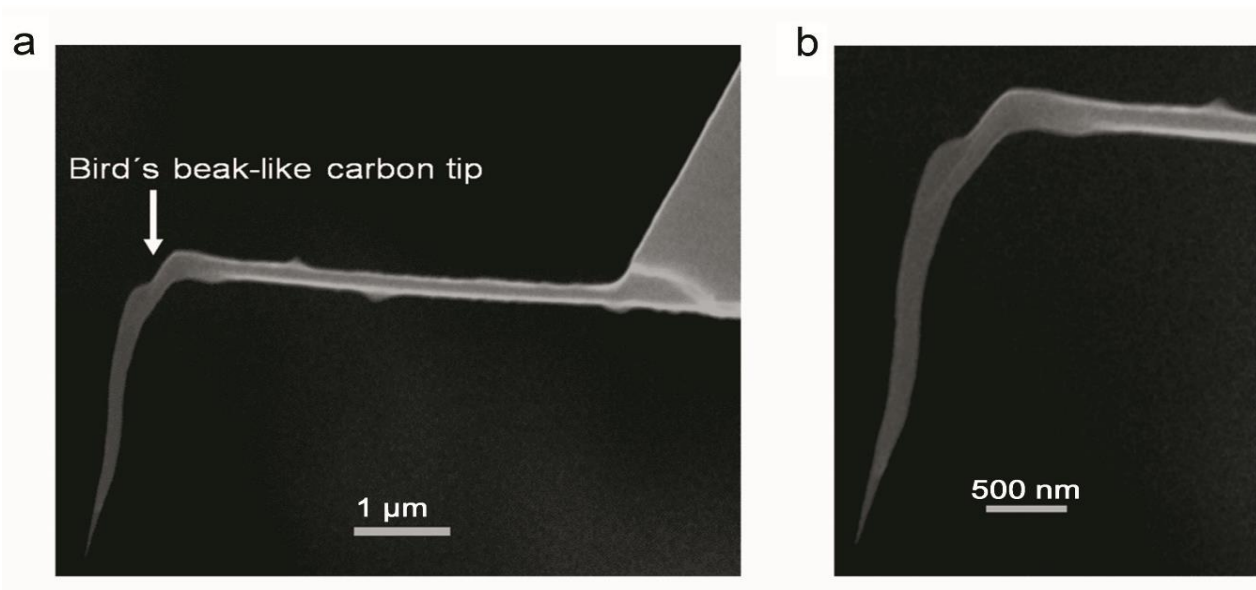
## INTRODUCTION

The NPC molecular weight is nearly ~125 MDa in vertebrates (1,2) and 66 MDa in yeast species (5). It has eight-fold symmetric cytoplasmic filaments. NPC has been well determined and is thought to have around 30 different types of proteins (called nucleoporins, or nups) (26). NPC structure has been determined by many microscopes previously including electron microscopy, Cryo-EM, high resolution fluorescent microscopy and atomic force microscopy. Recent study used HS-AFM to show the flexible motion and conformations of NPCs in action (65) in *Xenopus* eggs. However, still mammalian NPCs dynamic conformations and visualization in their native environments yet be investigated. Many factors belated the mammalian NPC nano-live visualization due to the small size of mammalian nuclei and the challenging purification procedures of the nuclear envelopes (26). In the current study, I have optimized different factors to study the native NPC structure and dynamics from different mammalian cells including cells cultured in 2D and 3D cultures. First, I have used GFP-tagged NEs to facilitate the first observations by HS-AFM. Second, I have prepared cantilevers with sharpened-long tips to improve the imaging quality. Thus, I visualised native NPCs dynamics in action in different cell types at the nano-scale.

## MATERIALS AND METHODS

### 1. Cantilever-tip fabrication

Very tiny cantilevers (BL-AC7DS-KU2 and BL- AC10DS, Olympus), custom-made with a spring constant  $k$  of  $\sim 0.2$  N/m and a resonance frequency  $f = 1.2$  MHz in water were used for the imaging in this study. The cantilever length, width, and thickness were 6–7  $\mu\text{m}$ , 2  $\mu\text{m}$ , and 90 nm, respectively. A very long, sharpened carbon tip was grown on the head part of each cantilever by EBD using a scanning electron microscope (ELS-7500, Elionix). Cleaning of cantilevers was achieved by UV/O<sub>3</sub> followed by piranha solution (also called piranha etch solution, which is prepared from a mixture of sulfuric acid and hydrogen peroxide). EBD was optimized by using a 30 kV as an accelerating voltage and an irradiation time of 2 min. The use of sharpened and long ( $\sim 2$   $\mu\text{m}$ ) carbon tips can improve HS-AFM imaging resolution (Figure 3) (26).



**Figure 3. Cantilever preparation.** Long carbon tip prepared on the cantilever top by EBD using Scanning Electron Microscope (SEM). (a) Side view of a cantilever body. (b) Side view of a cantilever sharpened tip with a length and radius of approximately 645 nm and 8 nm, respectively.

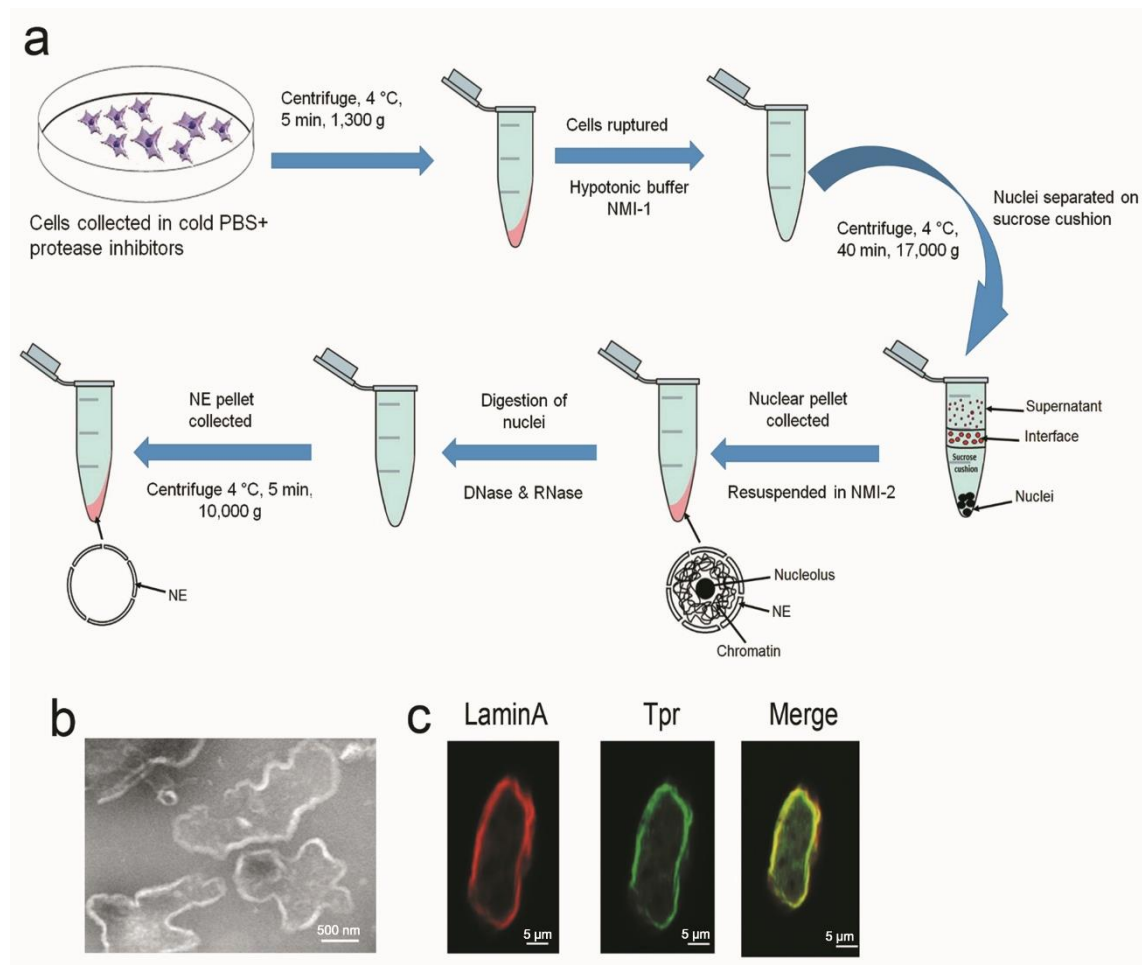
## **2. HS-AFM combined with fluorescence microscope**

HS-AFM was equipped with a wide-range scanner and was operated in a tapping mode (2 nm free amplitude, ~ 900 kHz) at the room temperature (55). The cantilever deflection was determined by detecting the position of the laser beam (670 nm) reflected by the cantilever with a position-sensing two-segmented photodiode. The laser beam focused onto the cantilever tip by using a 20× objective lens (CFI S Plan Fluor ELWD, Nikon). To combine HS-AFM with the fluorescence microscope, dichroic filters (MDF-GFP, Thorlabs), a CCD camera (DS-Fi2, Nikon) and an excitation lamp (M470LM, Thorlab), were installed below the HS-AFM system. A solution containing the GFP-labelled nuclear envelopes was applied on the PLL-coated glass stage and then used for fluorescence imaging as well as being subjected to nanometer imaging with HS-AFM. The free oscillation amplitude was ~ 2 nm, and the set-point amplitude was 80–90% of the free amplitude (Figure 3) (26).

## **3. Nuclear envelope purification**

HCT116 Cells were collected from plates by scraping in cold PBS containing protease inhibitors cocktail. Cells were collected by scraping and pelleted by centrifugation (4 °C, 5 min, 1,200 g). The pellet was washed with cold PBS, resuspended in 7 ml hypotonic Buffer NMI-1 and incubated on ice for 40 min. Cells were then ruptured by douncing and centrifuged (4 °C, 15 min, 2,200 g). Pellets were resuspended in Buffer NMI-2 and centrifuged (4 °C, 13 min, 2,100 g). Pellets were resuspended in 3.5 ml mixture of Buffer 2NMI-3:1NMI-2 and underlayered with 1.5 ml Buffer NMI-3 in an ultracentrifuge tube to form a sucrose bed under the cell lysate. The sample was ultra-centrifuged (45 min, 4 °C, 17,000g). Nuclear pellets were isolated from the bottom of the tube, nuclei were resuspended in Buffer NMI-2. Nuclear pellets were resuspended by addition of 1 ml Buffer NMI-4 drop-wise (containing DNase/RNase) with vortexing, followed by 4 ml of

Buffer NMI-5 and incubated at room temperature for 15 min. The digested nuclei were then underlayered with 4 ml of BufferNMI-6 and centrifuged (4 °C, 15 min, 3,500 g).



Nuclear envelope pellets were collected and resuspended in 200 μl Buffer NMI-7. The nuclei and NE pellets were prepared for EM analysis as previously described (95) (Figure 4).

**Figure 4. Nuclear envelope purification.** (a) Sucrose cushion method to isolate the NEs of HCT116 cells. (b) EM micrograph showing purified NEs (c) Confocal microscopy micrograph showing immune-stained NEs with anti-LaminaA and anti-Tpr antibodies.

## NE Extraction buffers

**Buffer NMI-1:** 50 mM Tris (pH 7.5), freshly added protease inhibitors.



**Buffer NMI-2:** 0.25 M Sucrose, 50 mM Tris (pH 7.5), 25 mM KCl, 5 mM MgCl<sub>2</sub>, 0.5 mM phenylmethylsulfonyl fluoride (PMSF), 2 mM Dithiothreitol (DTT), freshly added protease inhibitors.

**Buffer NMI-3:** 2.3 M Sucrose, 50 mM Tris (pH 7.5), 25 mM KCl, 5 mM MgCl<sub>2</sub>, 0.5 mM PMSF, 2 mM DTT, freshly added protease inhibitors.

**Buffer NMI-4:** 0.1 mM MgCl<sub>2</sub>, 0.2 mM PMSF, 1 mM DTT, 0.5 l DNase/1 ml and 0.5 l RNase/1 ml

**Buffer NMI-5:** 10 % Sucrose, 0.1 mM MgCl<sub>2</sub>, 0.2 mM PMSF, 1 mM DTT, 20 mM TEA (pH 8.5)

**Buffer NMI-6:** 30 % Sucrose, 0.1 mM MgCl<sub>2</sub>, 0.2 mM PMSF, 1 mM DTT, 20 mM TEA (pH 7.5)

**Buffer NMI-7:** 10 % Sucrose, 0.1 mM MgCl<sub>2</sub>, 0.2 mM PMSF, 1 mM DTT, 20 mM TEA (pH 7.5)

#### 4. Estimation of tapping force applied to the sample

Average tapping force, applied to the sample surface is expressed as;

$$\langle F \rangle = \frac{k_c A_0}{2Q_c} \sqrt{1 - r^2}$$

where  $k_c$  is the cantilever spring constant,  $Q_c$  is the quality factor of the cantilever resonance,  $A_0$  is the cantilever's free oscillation peak-to-peak amplitude,  $r$  represents the ratio of the amplitude set point,  $A_s$  of a force-feedback controller to  $A_0$  (i.e.,  $r = A_s/A_0$ ,  $0 < r < 1$ ). Using a typical imaging condition used in the present study (i.e.,  $k_c = 0.2$  N/m,  $Q_c = 2$  for the HS-AFM cantilevers (BL-AC7DS-KU2, Olympus),  $A_0 = 3 - 4$  nm,  $r = 0.9$ ),  $\langle F \rangle$  can be estimated to be 65 – 90 pN. In addition, we estimated  $F_{max}$  to be 70 – 80 pN in all

NPC experiments. However, in HS-AFM the impulse ( $= \text{Force} \times \text{time}$ ) is a more meaningful mechanical quantity because this describes the momentum transfer in the short time it takes the tip to make a single tap, which in the present study is less than  $0.1 \mu\text{s}$ . Thus, as demonstrated in many studies by HS-AFM (56), the expected effect on the NPC is very small which ensure that any disruption to the FG Nups is almost reduced.

	Gene name		Primer
ESCRTIII	CHMP7	F	gtctctcaaggccaagcaac
	CHMP7	R	tgtctgggaggcatagatcc
	CHMP4B	F	cgaaacctgtagggtttgga
	CHMP4B	R	ctgtttcgggtccactgatt
	CHMP2A	F	caggctgtgtccctcaagat
	CHMP2A	R	ggcaacttcagctgtctgt
	p97	F	gagctcctcaatgtgggtgt
	p97	R	ccaatcgcagacatagctga
	uFD1	F	gaacccgaaagacaagtcca
	uFD1	R	cccctttcttctttccatcc
FG-Nups	Nup358	F	aaacgagggtcaatggcaaac
	Nup358	R	gagaggcttcagggtcatcg
	Nup214	F	cacttcagcctgctgttgca
	Nup214	R	agacagaaaggctgatcg
	Nup153	F	gcagctctgcctttggaac
	Nup153	R	aagacaaatggggtgacagc
	Nup98/96	F	actgggacagcatttgaac
	Nup98/96	R	aaacagggctgaaccaacag
	Rae1	F	gctgctgggaagttcaagac
	Rae1	R	tcgtcactccagcagacatc
House keeping	beta-actin	F	tgacaggatcgagaaggaga
	beta-actin	R	cgctcaggaggagcaatg

**Table 1.** Sequences of PCR primers used in this study.

## **5. Image processing and data analysis**

HS-AFM image sequences were processed using ImageJ software ([imagej.nih.gov/ij/](http://imagej.nih.gov/ij/)). A fit polynomial filter was used with one order in x and y directions, and then by a 2-pixel median filter applied along the y-axis to reduce the horizontal noise. Cross-sectional analyses were performed to determine the characteristic sizes and height profiles (26).

The HS-AFM movies were processed to remove thermal drift in x, y and z-directions and to reduce the high frequency noise in x, y direction (z-scanner noise) by Image J software. First, the horizontal noise was reduced by the median filter with 2.0-radius. Second, the z-directional drift was removed by background subtraction of each frame with the primary functions in x- and y-directions, which resulted in no difference in average height between frames. At last, the horizontal drift was removed by using the template-match algorithm, where each frame was translated in xy-plane to maximize a normalized cross correlation coefficient between the frame being translated and the reference frame.

## **6. Cell Culture, Transfections, and Drug Treatments**

Human colorectal cancer HCT116 and SW480 cells were purchased from the American Type Culture Collection (ATCC) and were grown in Dulbecco's modified Eagle's medium (DMEM) supplied with 10% FBS (Life Technologies) and 50 U/mL penicillin–streptomycin (Nacalai Tesque). HCT116 and SW480 cells were established from the primary tumours of patients with adenocarcinoma in the right-side (ascending) and the left-side (sigmoid) colon, respectively, and characterized to represent the genotypes of microsatellite instability and chromosomal instability pathways, respectively (57, 58). These cell lines are considered among those most usually used in biomedical research for colorectal cancers. SW480 cells were used for live imaging experiments in this study. All

cell culture and transfection procedures were performed as previously described.(26, 59, 60).

## **7. Antibodies**

Anti-m414 (MMS-120R) antibody was purchased from COVANCE. Anti-Tpr rabbit antibody for confocal microscopy was a gift from Dr. Larry Gerace (The Scripps Research Institute). Anti-Tpr (sc-101294) (for immunoblotting) and anti-Tpr (sc-67116) antibodies (for immunoprecipitation) were purchased from Santa Cruz Biotechnology. Anti-GFP antibody (A-6455) was purchased from Life Technologies. Anti- $\alpha$ -tubulin (DM1A) antibody was purchased from Sigma-Aldrich. Antibodies to LC3, p53, and p21 were purchase from Cell Signaling Technology. Secondary antibodies (Alexa Fluor or rhodamine) were from purchased Molecular Probes (Life Technologies) (26).

## **8. Confocal, Total Internal Reflection Microscopy and Live Cell Imaging**

For confocal microscopy imaging, HCT116 or SW480 cells were used as described previously (61, 62) and were examined on a confocal microscope (FluoView FV10i, Olympus, objective 60 $\times$ /1.2). Similarly, for live cell imaging, HCT116 or SW480 GFP-Nups stable cells were imaged by confocal microscopy (FluoView FV10i, Olympus, objective 60 $\times$ /1.2) or a Nikon Ti-E total internal reflection (TIRF) inverted microscope. The Ti-E was equipped with a perfect focus motorized nosepiece, an additional emission filter wheel, and a CFI APO 100 $\times$  oil TIRF objective (NA = 1.49). This microscope was capable of detecting single-molecule fluorescence from the manufacturer (26).

## **9. Immunoprecipitation**

Immunoprecipitation assays were done as previously described.(59, 63).

## **10. Cell Cycle Analysis**

HCT116 or SW480 cells were transfected with siRNA, then trypsinized, washed twice with PBS, and fixed in 70% ethanol at  $-20^{\circ}\text{C}$  overnight. The fixed cells were then resuspended in PBS containing 50  $\mu\text{g/mL}$  RNase A (Nacalai Tesque) and 50  $\mu\text{g/mL}$  propidium iodide (Sigma-Aldrich). The cellular DNA analyzed using a FACSCanto II (BD Biosciences) with FACS Diva software (BD Biosciences) (26, 59).

### **11. Quantitative Real-time PCR (q)PCR**

RNA was extracted using TRIzol (Invitrogen), and cDNA was synthesized using the ThermoScript RT-PCR System (Invitrogen). Real-time PCR was done with the Thermal Cycler Dice real-time system with the SYBR Premix Ex Taq (Takara) (64). The primers used in this study is in [Table 1](#). The expression levels of genes analysed by qPCR were normalized relative to the levels of glyceraldehyde-3-phosphate dehydrogenase expression (26).

### **12. Electron Microscopy**

Transmission electron microscopy of HCT116 cells (with or without MLN8237 treatments) was performed as shown previously, and EM micrographs were recorded with a JEOL JEM-1200EX at 70–100 kV (26, 62, 64).

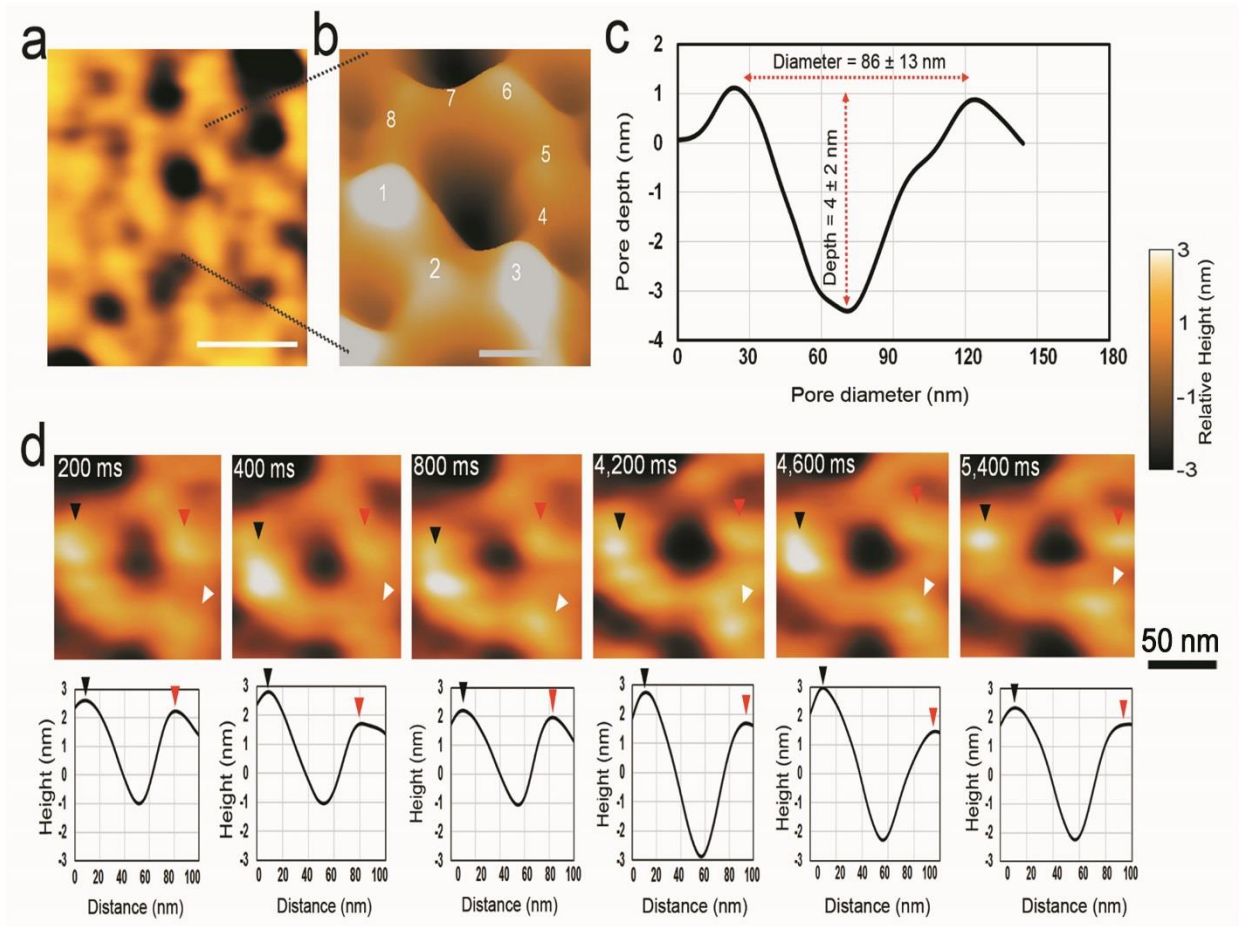
### **13. Statistical Analysis**

Statistical analyses were performed in Excel. Data are stated as mean  $\pm$  SD. Comparisons between different groups were analysed using the unpaired t student test.  $P < 0.05$  was considered as a statistically significant.

## RESULTS

### 1. Visualization of native NPCs in colorectal cancer cells (HCT116)

Figure 5a is showing a single HS-AFM frame captured from a movie of the cytoplasmic face of nuclear envelope with many NPCs. A single representative NPC is shown in Figure 1b. I found individual NPCs with eight globular-like pattern facing the cytoplasm (Figure 5a,b). Similar to recent study in *Xenopus* (65), I also observed pore-to-pore differences, I can observe a central plug inside the central channel of the NPC (Figure 7a,b). There are different models on the function and composition of those central granules as components of the NPC or “central plugs” or “transporter” (CP/T) or “cargoes in transit” (66, 67) or some peptides related to diseases that block the central channel of NPC (68, 69). To take an average, I analysed approximately 110 NPCs from HCT116 cells and summed out the mean values of NPCs measurements. They were  $4 \pm 2$  nm in depth, and the outer diameter of the outer scaffolding rings was  $86 \pm 13$  nm, which were quite similar to previous results of NPCs from other mammalian cells imaged by conventional AFM studies;(70-72) however, HCT116 cells’ NPCs were different in its depth compared with *Xenopus* oocyte NPCs (25) (Figure 5c). Figure 5d shows successive images of the same region of an outer ring, highlighting the sequential changes in the motion of cytoplasmic surfaces (26).

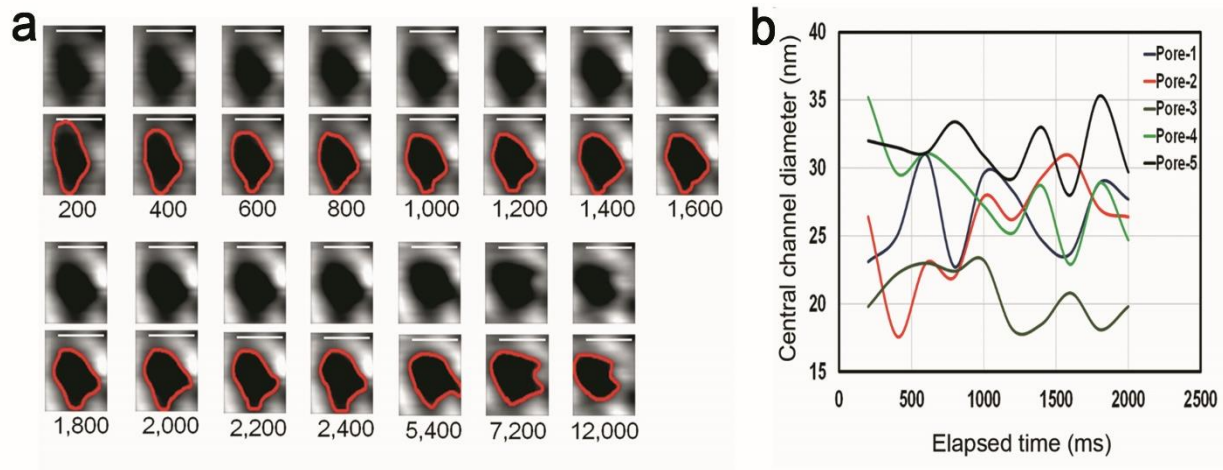


**Figure 5. HS-AFM observation of native human NPCs.** (a) HS-AFM frame showing the NE cytoplasmic face with many NPCs averaged from 74 frames (Z-scale = 6 nm, speed = 5 frames/s) with  $200 \times 200$  pixels; scale bar, 100 nm. (b) 3D view of a single representative NPC (Z-scale = 6 nm, speed = 5 frames/s) with  $200 \times 200$  pixels; scale bar, 50 nm. (c) Cross-section of human colon cancer NPCs with an overall diameter of  $86 \pm 13$  nm when measured from maxima of opposing filaments, where the central channel diameter is  $33 \pm 2$  nm and pore maxima depth is  $4 \pm 2$  nm ( $n = 110$ ). (d) Dynamic rapid changes of NPC cytoplasmic filaments in the shown HS-AFM frames at different time points at the millisecond scale (black, red, and white arrows) (Z-scale = 8 nm, speed = 5 frames/s) with  $200 \times 200$  pixels; scale bar, 50 nm.

which recorded at 200 ms/frame in another recording. I plotted their x–y directional displacement and height and then noticed that they have spontaneous extending or retracting dynamic spatial conformations (Figure 5d). Also, the inner nuclear central channel showed many successive changes in motion, probably caused by FG-Nups, under



the elapsed time of 200 ms/frame (Figure 6a). I further investigated these sequential HS-AFM frames and found a significant independent dynamic behaviour in five different representative inner channels (Figure 6b). Taken together, these data show that HS-AFM



**Figure 6. Inner channel dynamic changes.** (a) Sequential frames of a native NPC central channel showing the dynamic changes of the channel shape and diameter over time. The numbers below each frame correspond to the elapsed time (Z-scale = 6 nm, speed = 5 frames/s) with  $200 \times 200$  pixels; scale bar, 50 nm. (b) Central channel diameter changes over time plotted against the elapsed time (ms).

can be used to reveal the native nano-spatiotemporal dynamics of NPCs in colon cancer cells.

## 2. Effect of selective Aurora kinase A inhibitor on nuclear envelope structure

The structural and molecular consequential steps of NEs and NPCs in cell death are still unclear. To understand the cell dying process, we added MLN8237 drug (Alisertib), which is a known selective Aurora kinase A inhibitor that is being used in clinical trials (73) for cancer cures ([www.clinicaltrials.gov](http://www.clinicaltrials.gov)) (74) and has been determined to inhibit proliferation and induce autophagy, apoptosis, and senescence.(75) We analysed the mechanistic mechanisms of MLN8237-treated NPCs. MLN8237 treatment induced an arrest for the cell cycle and induced centrosome abnormalities and mitotic cell death in HCT116 cells (Figure 10b, Figure 15). In order to determine the changes happened in nuclear

morphology, we visualized the treated cells using EM, confocal microscope, and live imaging. As expected, we frequently nuclear deformation phenotypes occurred with many vacuoles after 48 h of MLN8237 treatment in HCT116 cells (Figure 9a). From the confocal and total internal reflection microscope and live maging of GFP-Nups or NE proteins (GFP-Lamin B1, GFP-Nup358, or GFP-Nup98 and GFP-Tpr), found that MLN8237 treatment also caused multinuclei pattern, nuclear fusion, nuclear budding, NE abnormality, and nuclear fragmentation (Figure 9b,Figure 11). Furthermore, MLN8237 treatment decreased NPC mRNA and protein expression (Figure 14a) before going to the cell death as a final step. The expression of Nup98 was significantly reduced, but Nup62 expression was not changed in the MLN8237-treated NEs (Figure 14a). These data are consistent with the previous ones that FG-Nup62 complexes can be replaceable for basic NPC function and that Nup98 is important for both passive and active transport.(76, 77). EM micrographs are showing that there were  $7.7 \pm 0.82$  nuclear pores/ $\mu\text{m}^2$  in HCT116 cells, which was similar to our previously data in HeLa cells(64). However, there were  $4.4 \pm 0.52$  nuclear pores/ $\mu\text{m}^2$  in MLN8237-treated cells (N = 90 pores from 3 sets of EM micrographs in control and MLN8237-treated cells respectively; Figure 16a). We also determined that NPC diameter was reduced by  $\sim 40\%$  after the treatment withMLN8237 (Figure 9c, N = 32 pores, micrographs in control and MLN8237-treated cells, respectively) (26).

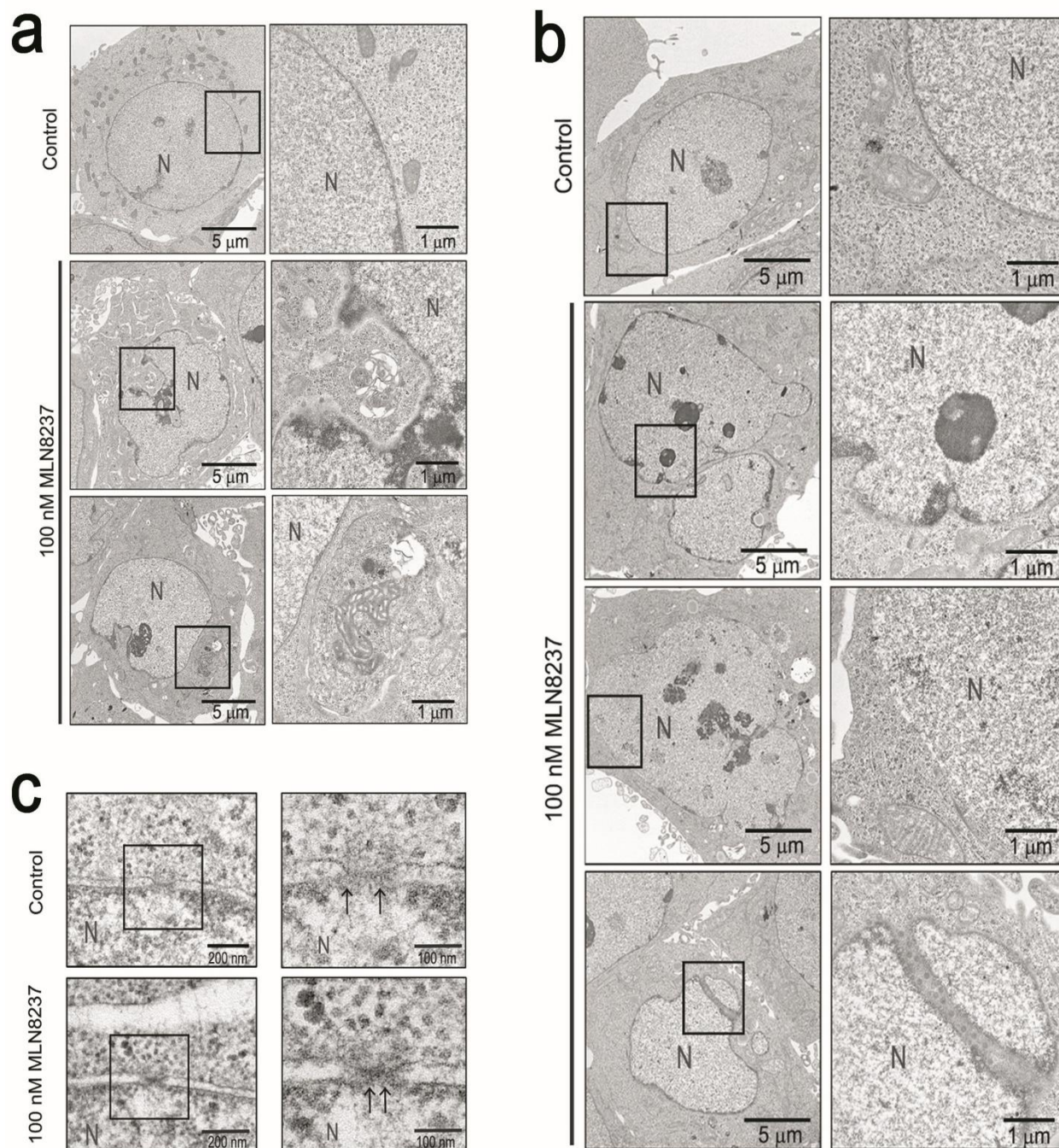
### 3. Mechanism of MLN8237

We determined the molecular mechanism of MLN8237 treatment; which induced p53-p21 oncogene-induced senescence pathway (78) (Figure 14a) and induced the autophagy biomarker LC3 (Figure 12, Figure 13b, Figure 10a). Therefore, the FG-Nups levels (Figure 14a) were reduced and the selective-flexible barriers of the NPC lost, further pushing LC3 and other proteins to enter to the nucleus and facilitating physical interaction

between nuclear membrane protein Lamin B1(79) and other nucleoporins (Nups) (Figure 12, Figure 13b, Figure 10a, Figure 14). NE blebs, exocytosis, budding and nucleophagy were also noticed in dying cells. Furthermore, the endosomal sorting complexes for the transport III (ESCRT III) family were involved in the resealing of the NE during cell migration.(80) We found that the mRNA expression of ESCRT III were decreased in the dying cells ( Figure 14b), which might explain why the nuclear envelopes that were ruptured after MLN8237 treatment could not be repaired. Taken together, these data showed that MLN8237 is a suitable drug for studying nuclear dynamics and NPC changes, because it can change the nuclear morphology and change NE and NPC normal activities cancer cells (26).

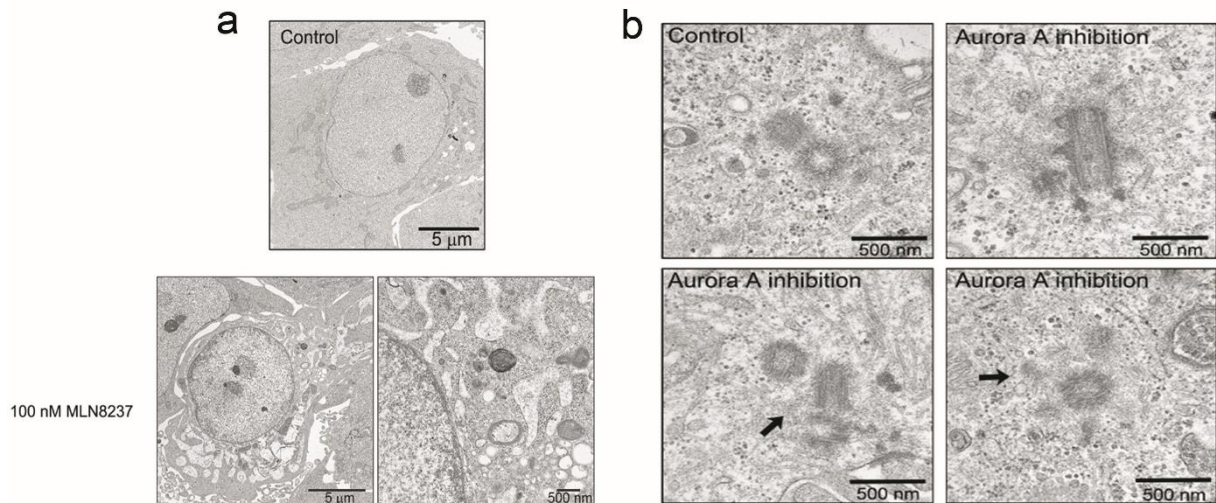
#### **4. Visualization of dying NPCs in cancer cells on the nanoscale using HS-AFM**

Standing on the basis of the obtained results, we further investigated the possibility of using HS-AFM to visualize the structure of individual NPCs at nano-scale after treating GFP-Nup358 HCT116 cells with 100 nM MLN8237 for 48 hours. The HS-AFM results showed that MLN8237 treatment can strongly affects the nano-structural normal architecture of the NPC. The NPC outer ring in MLN8237-treated cells showed different abnormal structures, which most likely indicate that the cytoplasmic filaments were non-globular than those of NPCs in control cells,

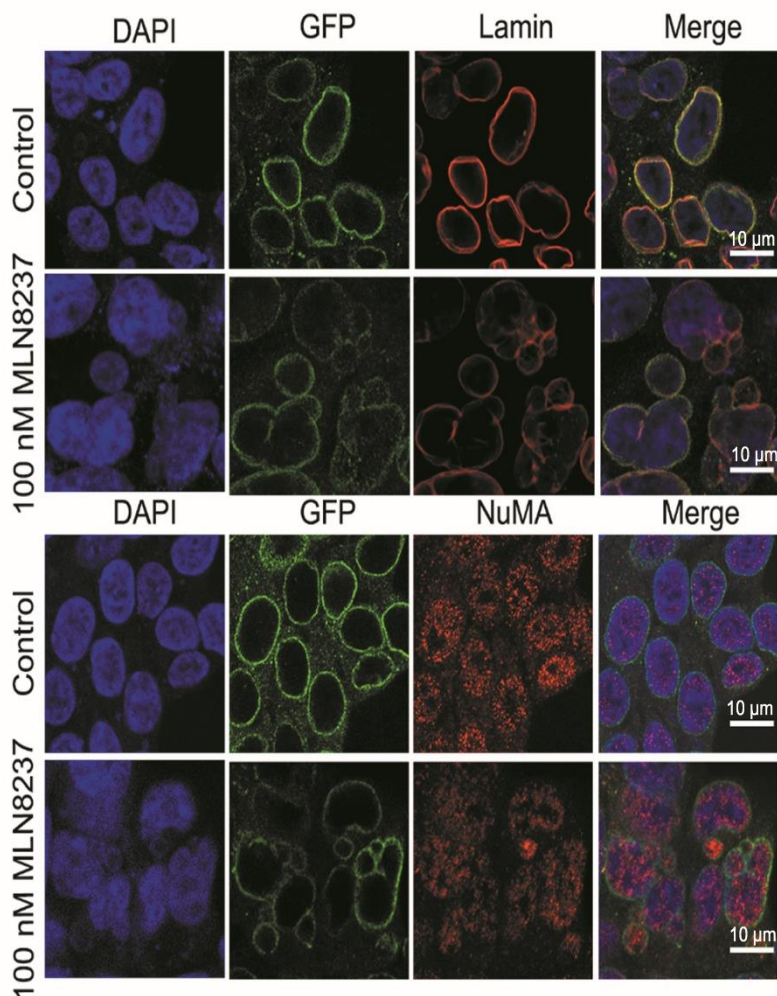


**Figure 9. Effects of MLN8237 drug treatment on nuclei in HCT116 cells.** (a) Electron micrographs of control or MLN8237-treated HCT116 mitotic cells. N refers to the nucleus. (b) Micrographs of control and MLN8237-treated HCT116 mitotic cells. (c) Micrographs of control and MLN-treated HCT116 cells.

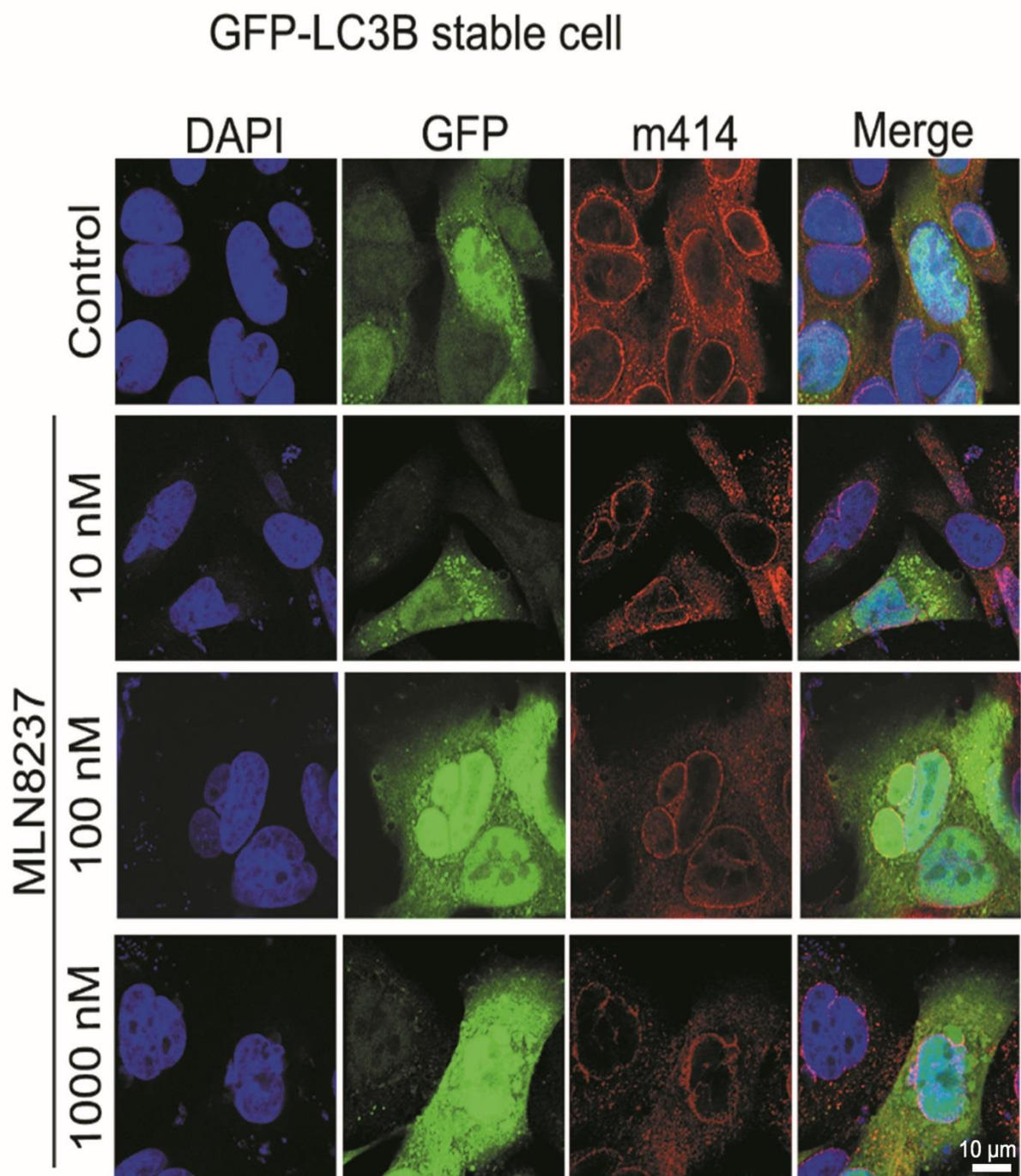




**Figure 10. Autophagic vacuoles and abnormal centrosomes in dying CRC cells.** (a) Electron micrographs of control and MLN8237-treated HCT116 cells. Insets are magnified areas of the vacuolated regions in the observed cells. (b) Electron microscopic images of control or MLN8237-treated HCT116 mitotic cells. Black arrow indicates abnormal configuration of centrosomes Scale bars, 500 nm.

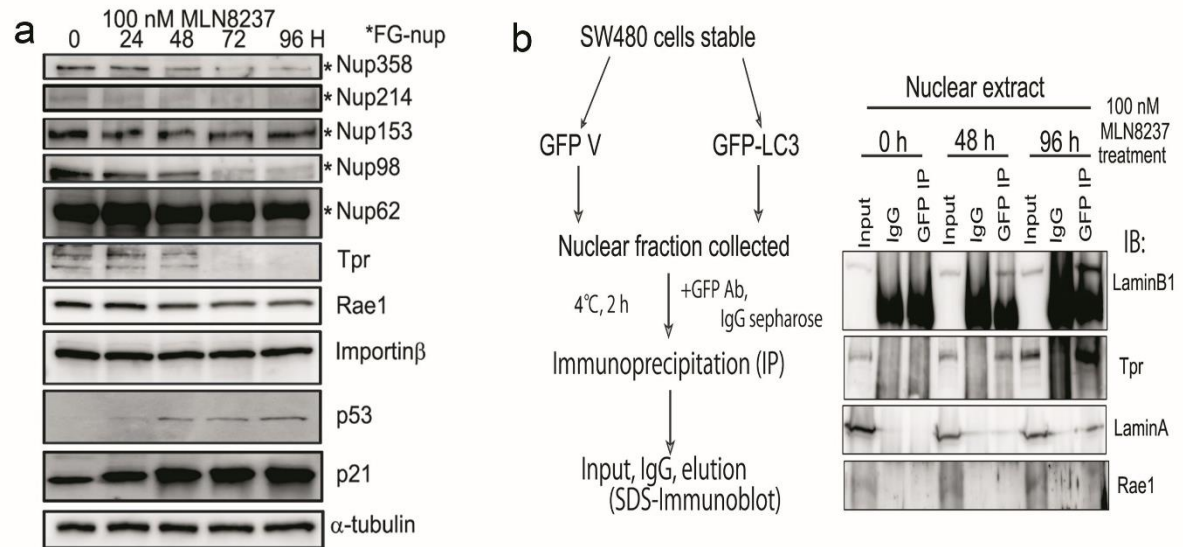


**Figure 11. Effects of MLN8237 drug treatment in HCT116 cells visualized by confocal live imaging.** (a) Confocal images of MLN8237-treated GFP-Nup358 HCT116 cells, which immunostained with GFP (green) and Lamin A/C (red, upper) or NuMA (red, lower) at the shown concentrations. DNA was counterstained using DAPI stain. Scale bar is 10 μm.

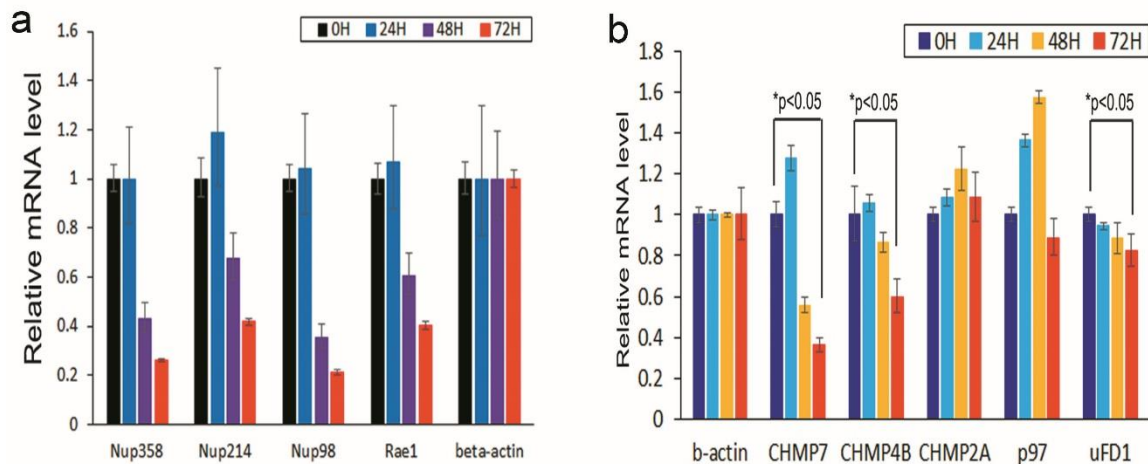


**Figure 12. Oncogene-induced senescence (OIS) enhanced cytoplasmic LC3 nuclear influx interacting with Tpr and Lamin B1 facilitated by NE and NPC rupture in dying CRC cells.** Representative confocal microscopic images of MLN8237-treated GFP-LC3 SW480 cells, stained with GFP (green) and m414 (red) at the shown concentrations.

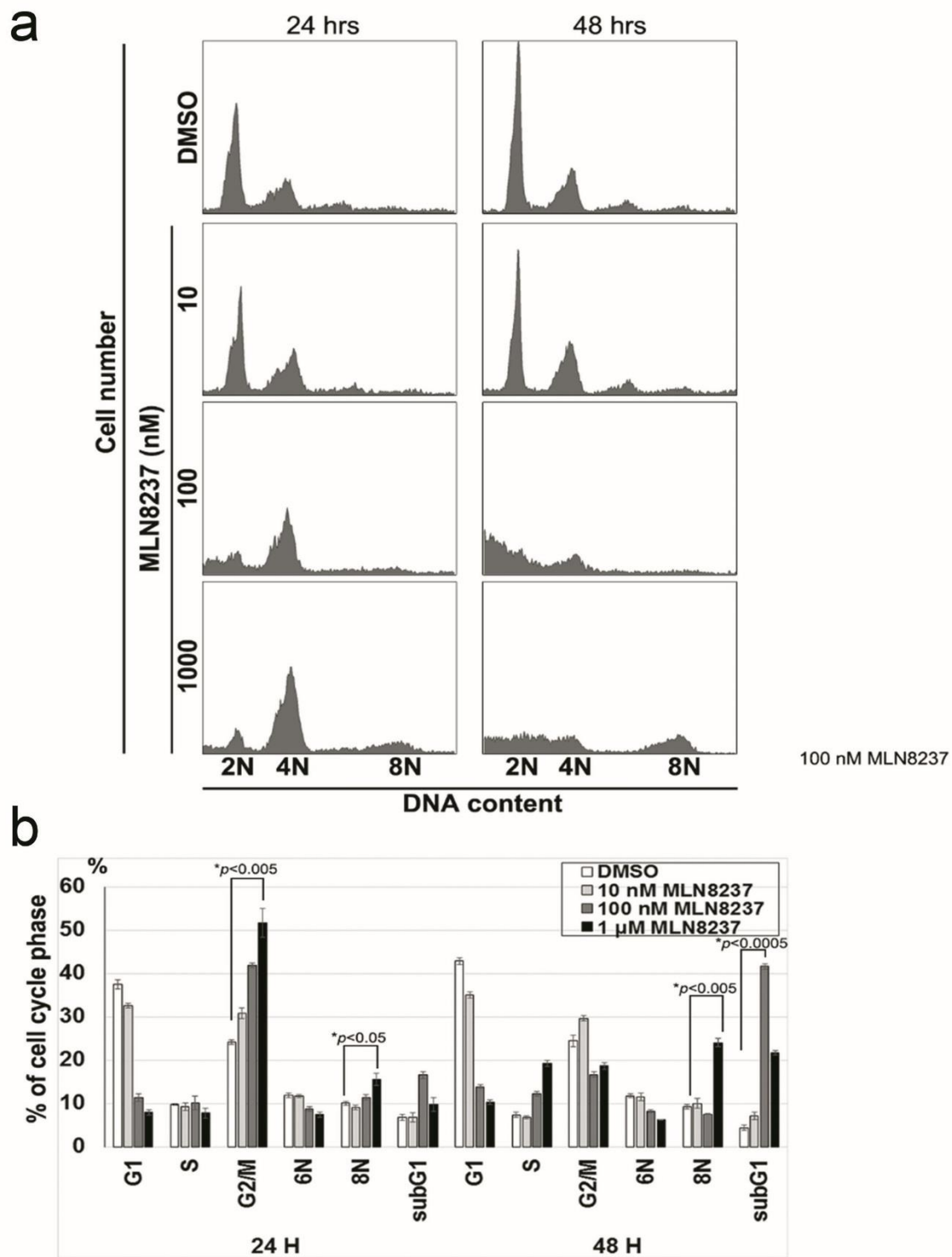




**Figure 13. FG Nups protein levels.** (a) HCT116 cells were treated with MLN8237 drug for 24, 48, 72, or 96 h with concentration of 100 nM and analyzed by immunoblot (b) Nuclear extracts containing GFP or GFP-LC3 were incubated with anti-GFP antibody-sepharose resin for 2 h at 4 °C to immunoprecipitate GFP or GFP-LC3 protein complexes (IP). IP fractions were washed three times and then eluted from the beads. The input, IgG, and eluted IP fractions were then analysed by immunoblotting. IP fractions from nuclear SW480 extracts were resolved by SDS-PAGE and immunoblotted with the indicated antibodies.

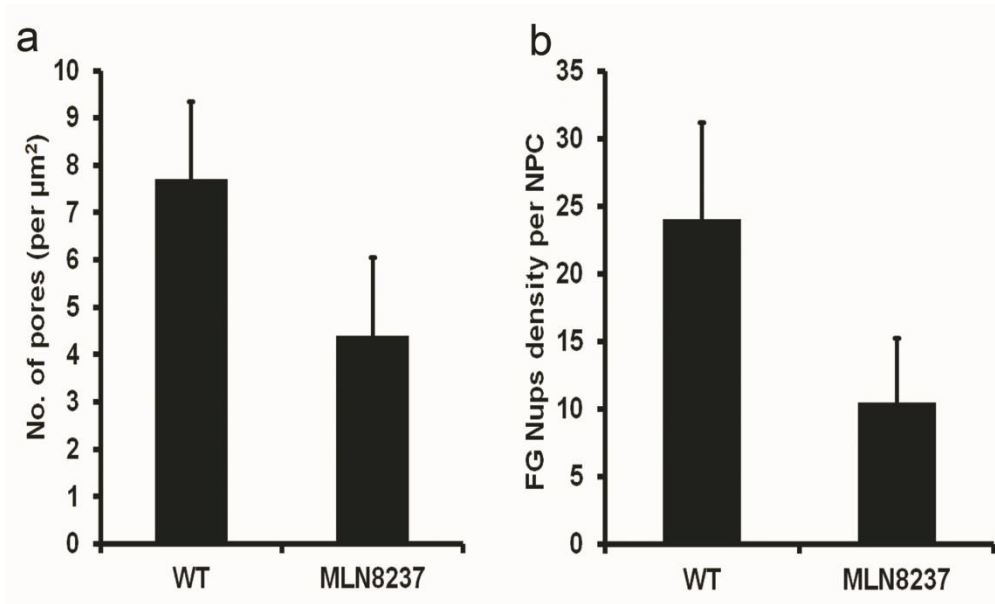


**Figure 14. QPCR analysis.** (a) HCT116 cells were treated with MLN8237 for 24, 48, 72, or 96 h at 100 nM concentration and then analyzed by qPCR. (b) HCT116 cells were treated with DMSO (control) or MLN8237 for 0, 24, 48, or 72 h, and the mRNA levels of ESCRT III factors were subsequently assayed by quantitative PCR. The data are presented as the means  $\pm$  S.D. for triplicate experiments. Bars, S.D. \* $p < 0.05$ .



**Figure 15. Effect of MLN8237 on the cell cycle.** (a) HCT116 cells were treated with MLN8237 for 24 or 48 h, and cell-cycle was analysed by flow cytometer (b) The percentages of G1, G2/M, S, and sub-G1 cells were calculated based on the results shown in (a). Asterisks indicate significant *p*-values (\**p* < 0.05 or \*\**p* < 0.005).

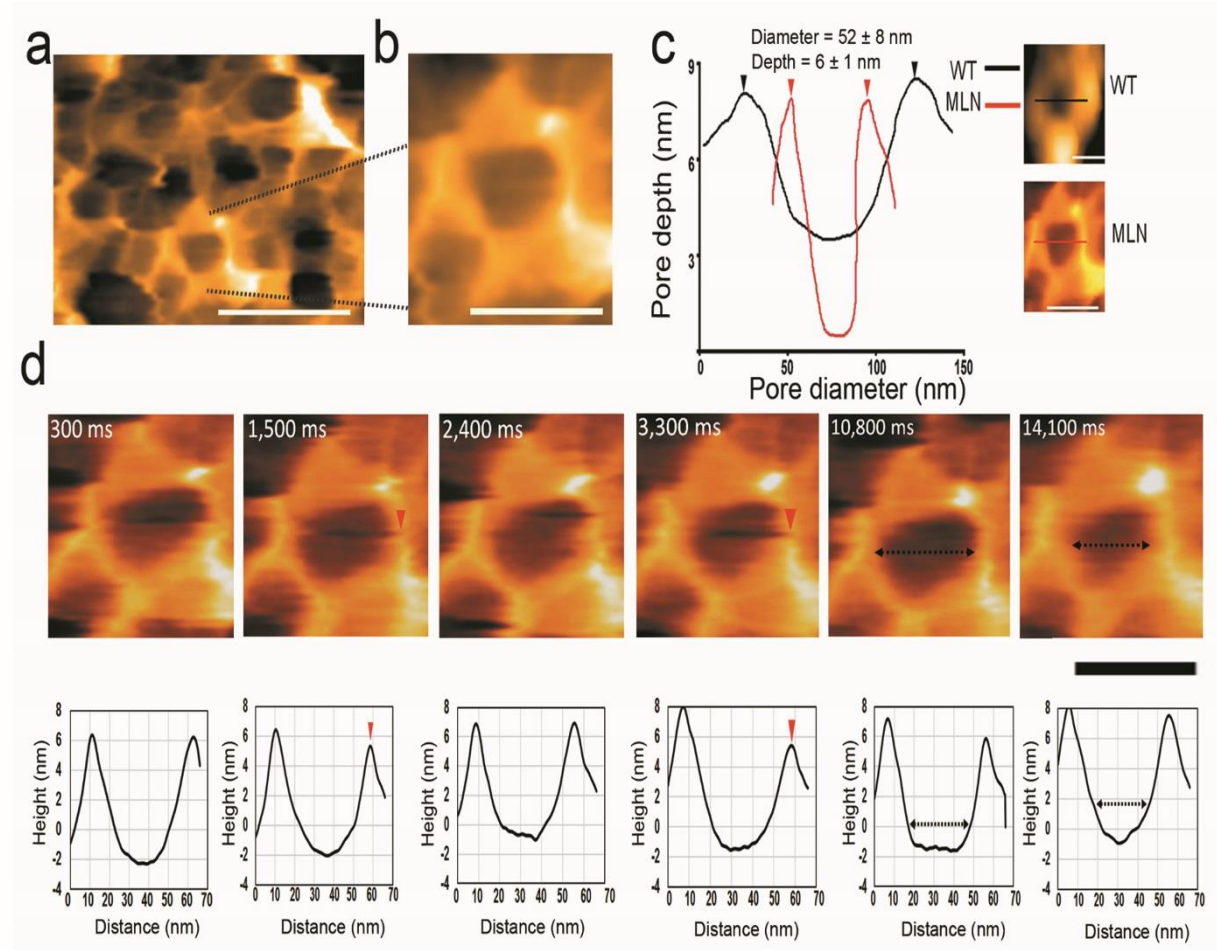




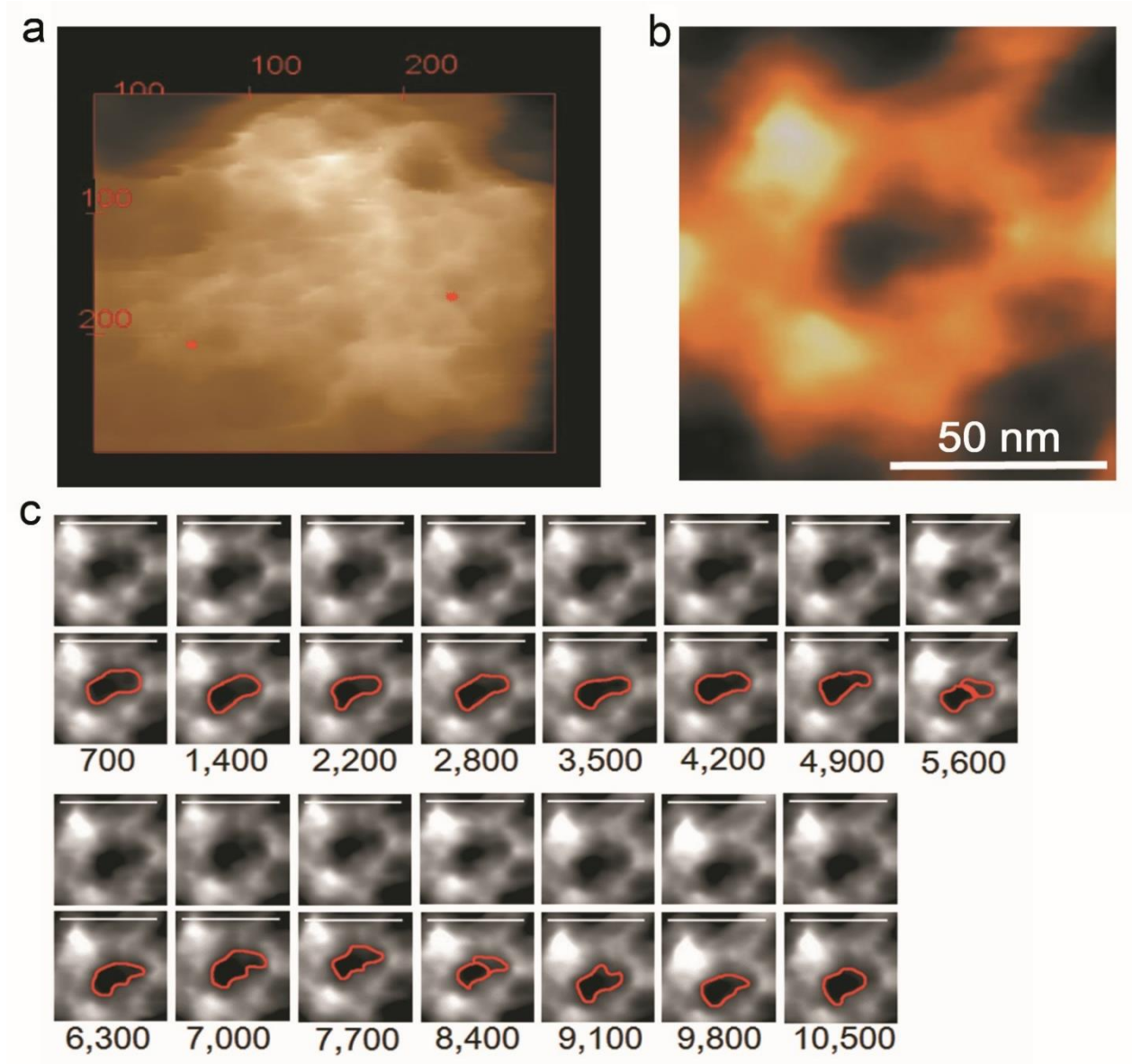
**Figure 16. Distribution of NPCs and FG-Nups.** (a) The distribution of NPCs on the NE surface of WT and MLN8237-treated cells. The graph showing the number of pores per  $\mu\text{m}^2$ . (b) The density of FG-Nup filaments in WT and MLN8237-treated NPCs. The graph showing the number of single FG-Nup filaments observed by HS-FM in a single NPC central channel, N=10.

probably due to the degradation of the cytoplasmic filaments of the damaged NPC after the drug treatment (Figure 17a,b). HS-AFM analysis of NPCs also determined that the outer ring diameter of MLN8237-treated NPCs (N = 85) was smaller ( $53 \pm 9$  nm), but the depth was deeper ( $7 \pm 1$  nm) than that of the control NPCs (N = 110) (Figure 17c). Furthermore, the data acquired from HS-AFM are paralleled by the immunoblotting and EM micrographs, which indicated degradation and reduction of Nups and a narrowing of the central channel (Figure 14a, Figure 9c). By performing precise analysis of the recorded movies, dynamic conformational changes were also noticed when I checked the cross-sectional analysis (Figure 17d). The selected images highlight the sequential changes in the nano-motion of cytoplasmic faces at 300 ms/frame in other different recordings of outer nuclear rings. The severe morphological changes observed in the nuclear membranes in EM micrographs, also confirmed by HS-AFM images (Figure 18a) which showing a  $300 \times 300$  nm<sup>2</sup> area with many clear damaged pores (red stars) and abnormal nuclear surface appearance. This HS-

AFM recording showing another pattern of dying NPCs in which the central channel lost its normal flexible motion as appeared in Figure 18b, c.



**Figure 17. HS-AFM imaging of NPC conformational changes in dying HCT116 cells.** (a) Dynamics of the native HCT116 NPCs after treatment with MLN8237 (100 nM, 48 h) (Z-scale = 20 nm, speed = 3.3 frames/s) with  $200 \times 200$  pixels; scale bar, 100 nm. (b) Single representative NPC in the dying cells (Z-scale = 20 nm, speed = 3.3 frames/s) with  $200 \times 200$  pixels; scale bar, 50 nm. (c) Comparison diagram showing differences in diameter and depth between wild-type (WT,  $N = 110$ ) and MLN8237-treated NPCs ( $N = 85$ ). The pore diameter of the treated NPCs is  $53 \pm 9$  nm, the depth is  $6.5 \pm 1$  nm, and the central channel diameter is  $28 \pm 5$  nm. (d) HS-AFM images recorded at different time points to show the dynamic changes of dying NPC after MLN8237 treatment. The NPC diameter is indicated by black dotted arrows. Red arrows refer to changes in the NPC filaments. Z-scale = 20 nm, speed = 3.3 frames/s with  $200 \times 200$  pixels; scale bar, 50 nm.

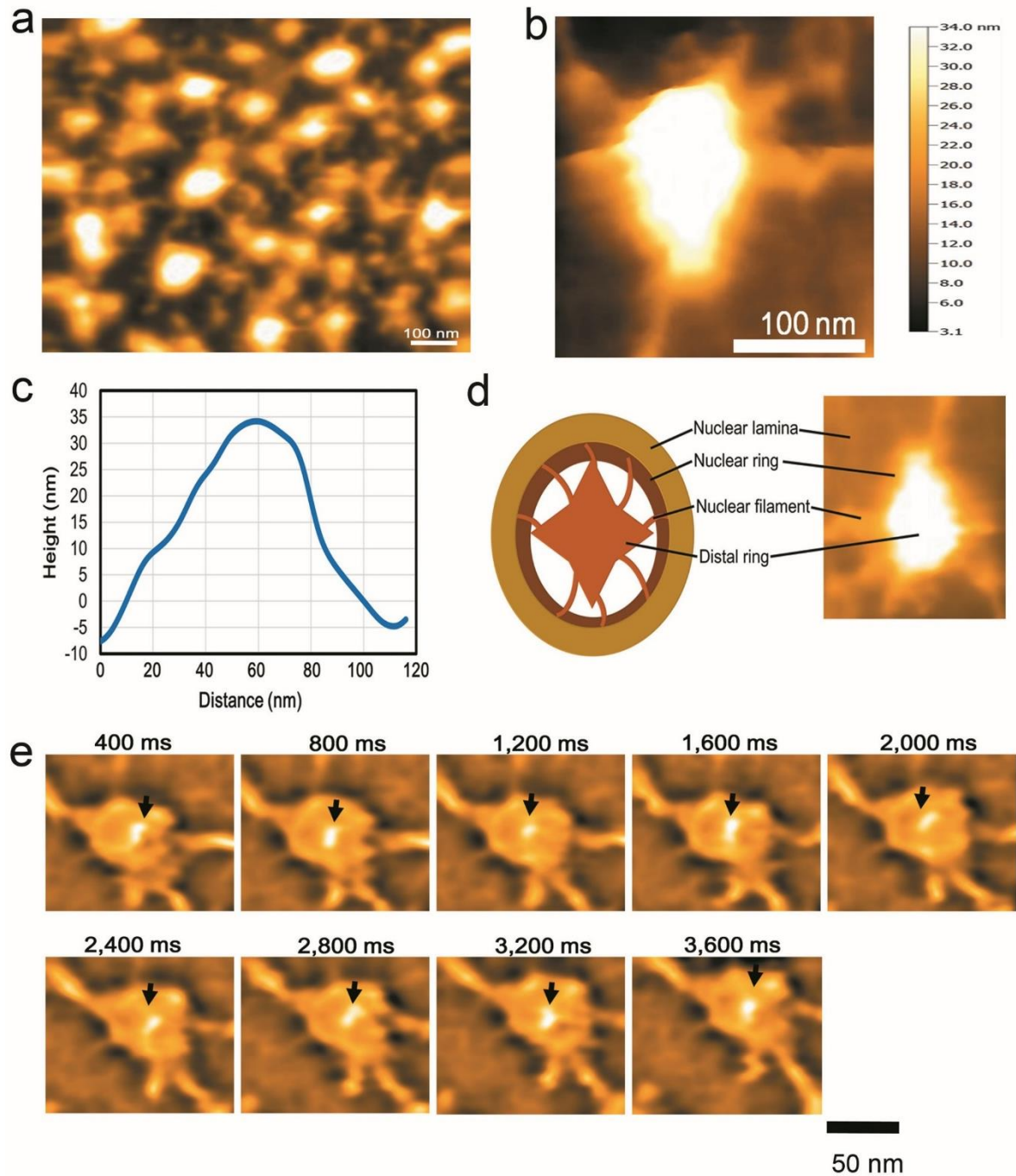


**Figure18. HS-AFM imaging of other patterns of MLN8237-treated NPCs.** (a)NE surface of MLN8237-treated HCT116 cells with many NPCs. This area showing the severe damage appeared after the 100 nM-MLN8237. Red stars refer to some NPCs. Z-scale=24 nm, speed=1 frames/s with 200×200 pixels; the red bars 100 means in nm scale. (b)A Single NPC from the same area in **a** imaged in a separate recording, showing another pattern of NPCs structure due MLN8237 treatment. Overall pore diameter is  $55\pm3.1$  nm, pore depth is  $7\pm1$  nm and central channel diameter is  $27\pm4$  nm (N=13). Z-scale=24 nm, speed=1.4 frames/s with 200×200 pixels. Scale bar; 50 nm. (c)Successive HS-AFM frames of the NPC (shown in **b**) central channel showing the dynamic changes of the channel shape and diameter over the time which became a narrow channel compared with the WT. The overall structure of the NPC seen in the WT is almost lost in this pattern. The numbers below each frame refer to the elapsed time (Z-scale=24 nm, speed is 1.4 frames per second), scale bar; 50 nm.

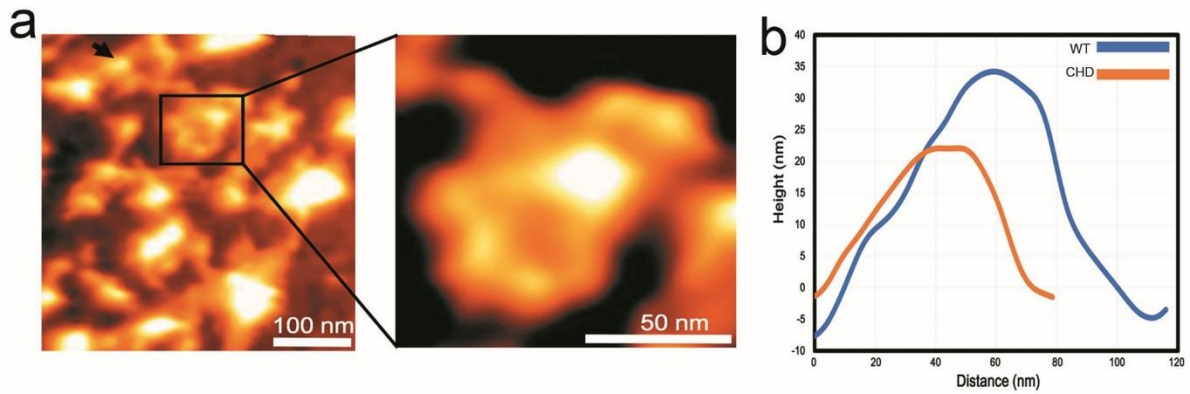
## 5. Observation of native nuclear basket dynamics in HCT116 cells

I investigated the native structure and the spatiotemporal dynamics of the nuclear basket. Since the nuclear basket dynamics with a significant role in nucleocytoplasmic transport. The overall structure of the basket of NPC has a diameter of  $102 \pm 23$  nm and the average height  $\sim 34 \pm 6$ , (N=27), whereas the distal ring was approximately  $\sim 50$  nm in the diameter as shown in Figure 4a-d. The HS-AFM observations showed the average thickness of the native nuclear ring  $\sim 12 \pm 2.8$ , (N=20). I concentrated the HS-AFM observation on  $200 \times 200$  nm<sup>2</sup> with a scan speed 400 ms/frame, to reveal the dynamics of the distal ring which shown in Figure 19e. Furthermore, I tried to change the conformations of the nuclear basket by using 3% 1,2 hexanediol (specific inhibitor for FG Nups). After the inhibitor treatment, the distal ring appeared in an open pattern (black arrows) in Figure 20a. The average diameter of the nuclear basket diameter is reduced to  $75 \pm 13$  nm, (N=27) and the height  $\sim 21 \pm 5$ , (N=27) as shown in Figure 20b. Figure 21 is showing the live conformational changes of the open-pattern distal ring under the effect of 1,2 hexanediol. Taken together, these data determined the native structural dynamic of mammalian nuclear basket. In addition, the distal ring opening and closing mechanism visualized by using CHD treatment (Figure 22).

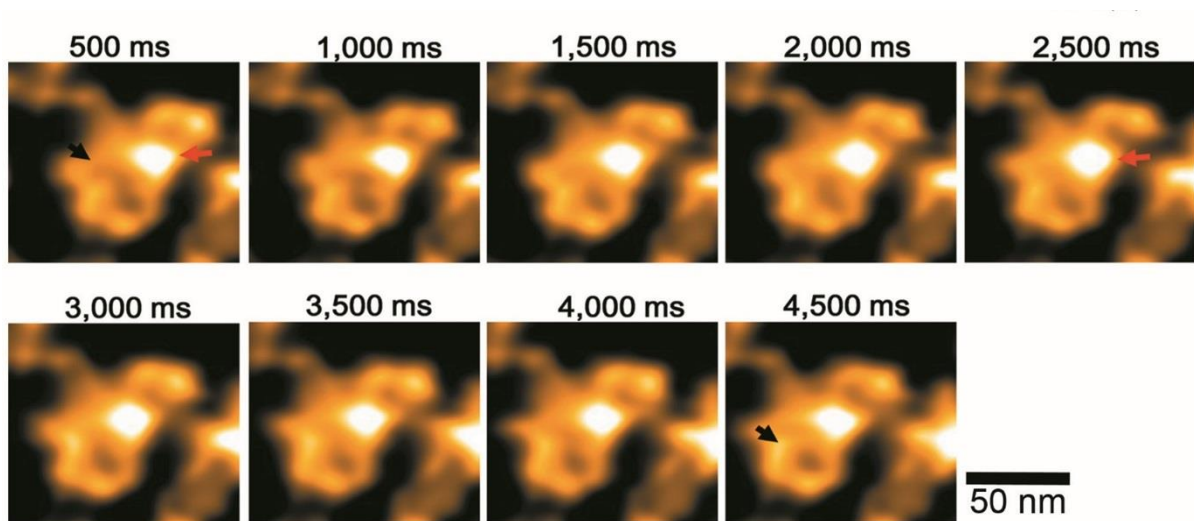




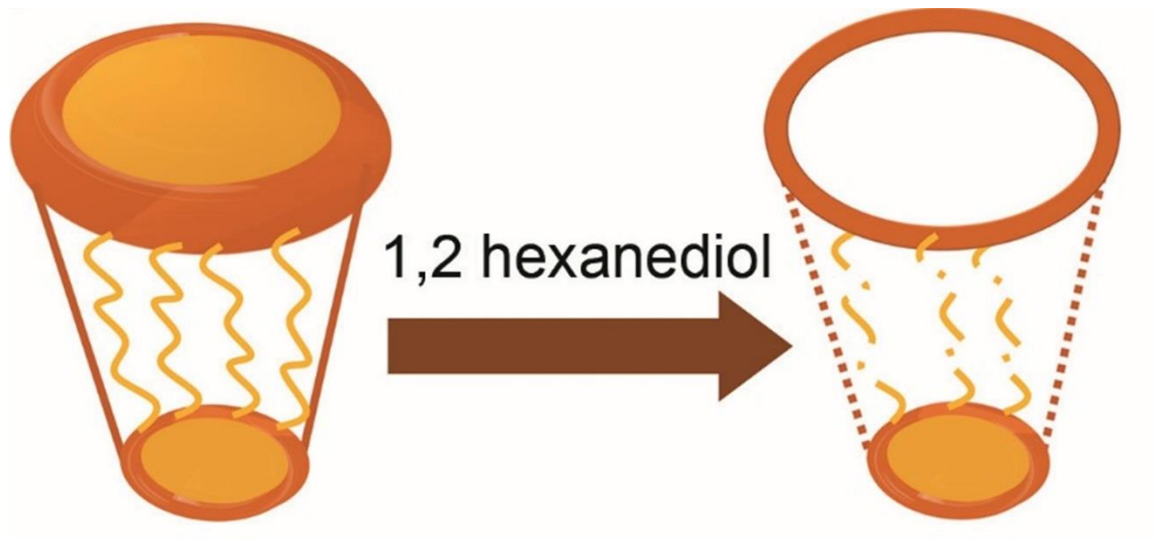
**Figure 19. HS-AFM observation of native nuclear basket dynamics in HCT116 cells.** (a) HS-AFM image of 600×600 nm scan area showing the native nuclear baskets of colorectal cancer cells. Z-range = 34 nm, scanning speed is 2.5 frame per second. (b) HS-AFM image rendered in 3D format showing a single native native nuclear basket with stretched nuclear filaments surrounding the distal ring. Z-range = 34 nm, scanning speed is 2.5 frame per second. (c) Average diameter of native nuclear basket  $\sim 102 \pm 23$  nm and the average height  $\sim 34 \pm 6$ , (N=27). (d) Illustration showing the structure of the nuclear basket protruding from the nuclear lamina. The HS-AFM observations showed the average thickness of the native nuclear ring  $\sim 12 \pm 2.8$ , (N=20). (e) HS-AFM images showing the rapid changes of the distal ring (black arrow) together with the nuclear filaments of a native nuclear basket. Z-range = 34 nm, scanning speed is 2.5 frame per second.



**Figure 20. HS-AFM observation live degradation of nuclear basket after 1,2 hexanediol treatment.** (a) HS-AFM live observation of nuclear basket conformations after adding 3% of 1,2 hexanediol (CHD). The drug added during imaging process into the imaging buffer. Many baskets degraded and lost their nuclear filaments, some other baskets appeared with an opened distal ring (magnified). The distal ring conformations observed 15 min after adding the drug. (b) The average diameter of nuclear basket decreased after 1,2 hexanediol treatment to be  $\sim 75 \pm 13$ , (N=27) and the height  $\sim 21 \pm 5$ , (N=27).



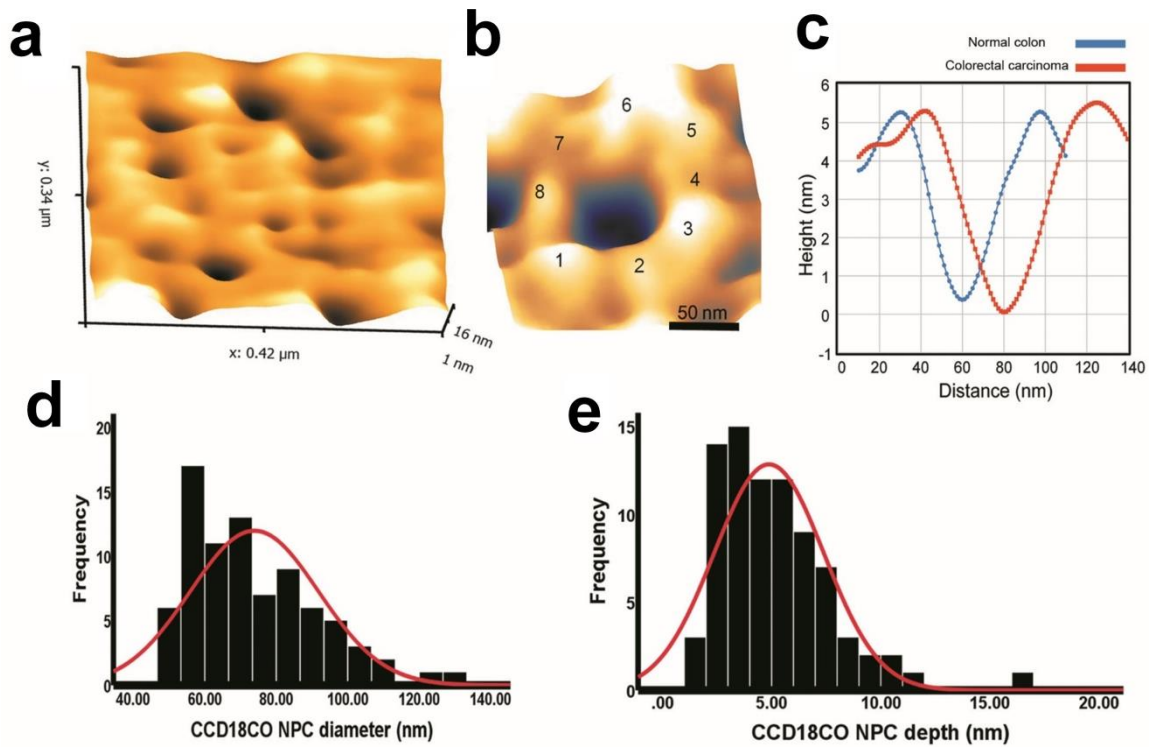
**Figure 21. HS-AFM observation live degradation of nuclear basket after 1,2 hexanediol treatment.** HS-AFM images of the dying nuclear basket showing rapid conformational changes including opened pore (black arrow) and degraded cap-like distal ring. Z-range = 34 nm, scanning speed is 2 frame per second.



**Figure 22. HS-AFM observation live degradation of nuclear basket after 1,2 hexanediol treatment.** Illustration showing the conformations of the nuclear basket after the 1,2 hexanediol treatment including degradation of nuclear filaments and the opened distal ring.

## 6. Visualization of native NPCs in normal colon cells (CCD18CO)

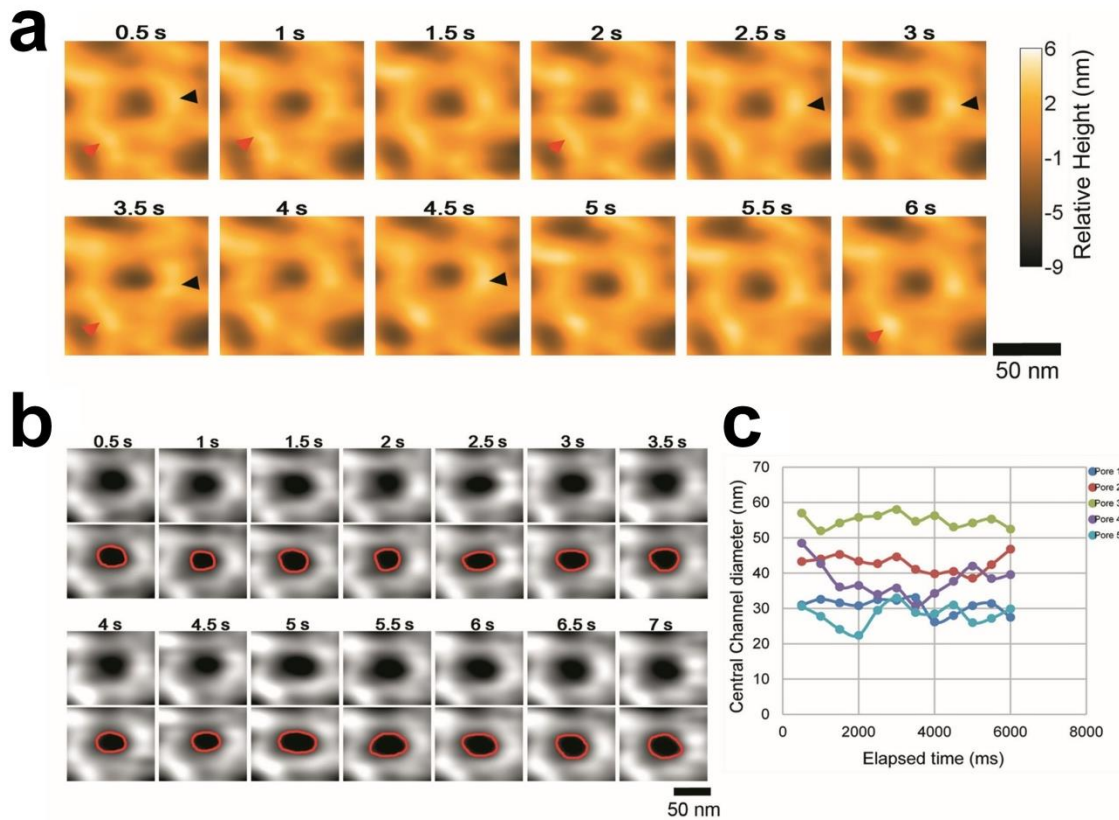
Figure 23a shows a single HS-AFM image from movie of the cytoplasmic face of nuclear membrane with many NPCs in normal colon cells. A single representative NPC is shown in Figure 1b, which was recorded at 2 frames/s. I often found individual NPCs with approximately eight globular-like features facing the cytoplasmic region (Figure 23a,b) consistent with results shown HCT116 cells. After averaging the NPC diameter and depth, I found no significant difference between normal and cancer cells under the current approach as shown in Figure 1c. CCD18CO NPC showed average diameter of  $74 \pm 18$  nm and average depth of  $5 \pm 2.5$  nm (N=81).



**Figure 23. HS-AFM observation of native NPCs of normal colon cells.** (a) HS-AFM image showing of the cytoplasmic face of the native nuclear envelope of CCD18CO cells. Z-range = 16 nm, scanning speed is 2 frame per second. (b) HS-AFM image rendered to 3D format showing average structure native NPCs appeared in **a**. (c) Plot showing the average diameter and depth of NPC as  $74 \pm 18$  nm and  $5 \pm 2.5$  nm respectively (N=81). The average diameter is a little smaller than colorectal cancer NPCs. (d) Normal distribution curve of NPC diameter. (e) Normal distribution curve of NPC depth



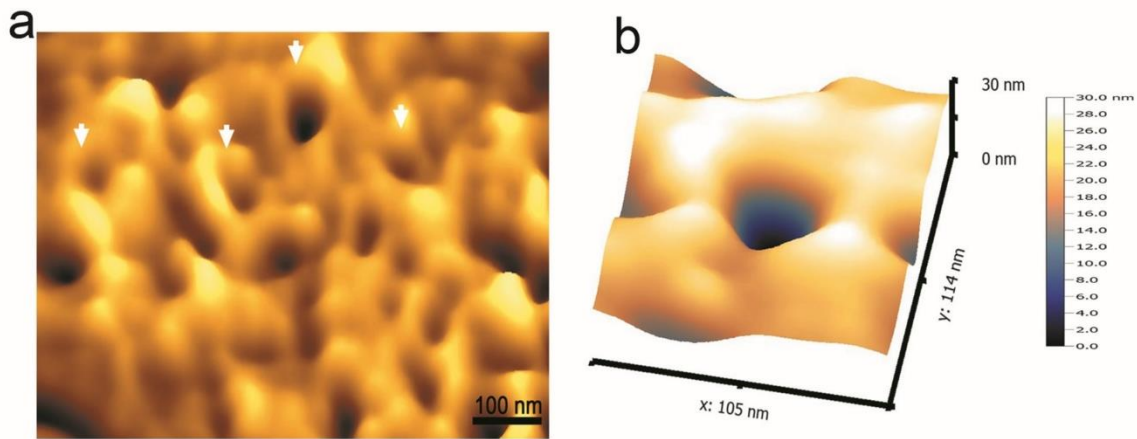
Figure 24a is showing sequential images of the same region of an outer scaffolding ring, determining the dynamic changes in the motion of cytoplasmic faces recorded at 500 ms/frame in another HS-AFM recording. Indeed, the inner nuclear central channel also showed many successive conformational changes in motion, probably caused by FG-Nups, under the elapsed time of 500 ms/frame (Figure 1b). I further investigated these sequential HS-AFM frames and determined a significant dynamic behaviour in five different representative central NPC channels (Figure 24b). Taken together, these data revealed the native nano-spatiotemporal dynamic of NPCs in normal colon cells.



**Figure 24 Inner channel conformational changes in normal colon cells.** (a) HS-AFM successive frames showing the dynamic changes of NPC cytoplasmic filaments (red and black arrows) of CCD18CO cells. Z-range = 16 nm, scanning speed is 2 frame per second, scale bar is 50 nm. (b) HS-AFM successive frames showing the dynamic changes of NPC central channel. Z-range = 16 nm, scanning speed is 2 frame per second, scale bar is 50 nm. (c) Central channel diameter of five different pores plotted against the elapsed time to show the rapid dynamic changes in the central channel diameter and shape. The average diameter of central channel is  $39 \pm 10$  nm (N=81).

## 7. Intact structure of NPC in 3D tumour colonic organoids (AKTP)

I wondered whether NPC dynamics are the same in 3D organoids which isolated from colonic tissues with further mutations. These organoids have the tumour characteristics. I isolated the nuclei and visualized the cytoplasmic face of the NE as shown in [Figure 25a](#) with many NPCs with globular appearance as determined in [Figure 25b](#).



**Figure 25. HS-AFM observation of native NPCs of AKTP colonic organoids.** (a) HS-AFM image showing of the cytoplasmic face of the native nuclear envelope of AKTP organoids. Z-range = 30 nm, scanning speed is 2 frame per second. (b) HS-AFM image rendered to 3D format showing average structure native NPCs appeared in **a**.

## DISCUSSION

Previously, HS-AFM has been developed and used for the imaging of single biomolecules in a dynamic process at a high spatial-temporal resolution without breaking their normal structure and function; (84) however, the observation of live dynamics of intracellular organelles, such as the nucleus or mitochondria, is still very difficult due to cantilever tip size, intact sample immobilization techniques, measurement conditions, and other nano-mechanical parameters. In the current study, I succeeded to visualize the native structure of NPCs in different mammalian colon cells including colorectal cancer cells, normal colon cells and tumour colonic 3D organoids. Although, it was very challenging to observe mammalian NPCs at work, but I revealed that HS-AFM can be used as a promising tool to visualize the dynamic processes of such large protein complexes in its native state. Not just revealing the dynamics of the cytoplasmic face but also, I showed the nuclear basket dynamics and the distal ring open and close states in dynamic motions. Taken together, the mammalian NPCs in very dynamic and flexible protein complex as shown by HS-AFM on the nanometer resolution.

## CONCLUSIONS

In the current study, HS-AFM movies strongly consistent with the hypothesis that the resilience of NPCs is lost in the dying nuclei of colorectal cancer cells, which facilitates nuclear deformation and blebbing. As a conclusion, by mainly using HS-AFM observations and other integrated imaging methods with an inhibitor of Aurora A in human colorectal cancer cells, I determined that the loss of the nanoscopic structural conformations of NPC is another hallmark or a dying code in cancer cells. In addition, I visualized the live dynamics of normal colon NPCs and AKTP colonic organoid which showed a similar pattern of colorectal cancer NPCs. Together, I demonstrated that HS-AFM allows the direct visualization and resolving of structural dynamics of native NPCs in its native environment. Also, HS-AFM may act as a novel and promising intracellular nano-endoscopy that can be used to visualize other native organelles inside the cell.

## **Chapter II: Tracking of intrinsically disordered FG Nups inside the nuclear pore**

### **ABSTRACT**

Nearly one-third of nucleoporins contain natively unstructured domains, intrinsically disordered phenylalanine-glycine repeats (FG-Nups), which mediate the transport selectivity. The selective barrier model of work has so far remained unresolved because the FG Nups have eluded direct structural analysis within NPCs. In this study, I show that high-speed atomic force microscopy (HS-AFM) can be used to as a strong toll for the direct visualization of nano-changes of the nuclear pore inner channel in normal and tumour cells. Furthermore, using MLN8237/alisertib, which used as apoptosis and autophagy inducer, I showed that the functional abnormality of nucleoporins, particularly the deformation of the FG-Nups barrier, in dying cancer cells. In addition, I precisely proposed a new biophysical model for the single FG filament bending and extension in healthy and cancer based on my HS-AFM nano-observations and calculations. Therefore, these data revealed new patterns of those intrinsically disordered FG Nups in their native environment. The current HS-AFM observations of native FG Nups provide a tentative explanation of the biophysical motion model of FG Nups inside the central channel. The current data explain how the single FG filaments form the central selective network. Furthermore, this model explains how the IDP-FG Nups turnover from one state to another on in the native NPCs. Also, this model revealed that IDP-FG filaments under certain conditions, twist over each other to form a thick aggregate which gradually may form a central granule. Taken together, these results unveiled different nano characteristics of FG Nups in different mammalian cells.

## INTRODUCTION

The molecular organization of the FG filaments and nuclear central plug remains poorly understood. However, the central NPC channel still awaits for deep nanomechanical and structural characterization, because its intrinsically disordered behaviour is not amenable to techniques that are based on *X-ray* crystallography, and because its central location deep within the NPC structure has remained invisible with the current surface techniques such as atomic force microscopy (AFM). The nature of the selective barrier is still unclear, and it has been proposed that Nups act as a dynamic polymer brush or form a cross-linked network (hydrogel) or spider cobweb

### 1. Intrinsically disordered proteins (IDPs)

Recently, the term of “Intrinsic Disorder” in proteins has gained a great care and importance as the functional roles of IDPs are being increased and identified in eukaryotic proteomes (96). Structured proteins can adopt energetically stable three-dimensional conformational changed with the minimum free energy. However, IDPs, due to their special amino acid sequence arrangements, cannot adopt energetically the same needed conformations; thus, they lack stable secondary structures (97). This unique structural plasticity allows IDPs to be functionally working in different signaling pathways, conferring multiple regulatory functions (98, 99). In fact, the dysregulation of IDPs are associated with many diseases including cancer (100), giving insights that IDPs play key roles in many functional pathways.

Even they do not have a stable tertiary structure; IDPs have important biological functions in many tissues and organs. Recently, using a promising data mining tool for more than 200,000 proteins from the Swiss-Prot database showed that many protein functions are related to some disordered domains (101, 102).

AFM has previously determined the surface topography of fixed and unfixed NPCs in the purified nuclear envelopes, which still maintain physiological selectivity and rate of transport mainly from *Xenopus laevis* oocytes. Additionally, AFM has been used to study recombinant Nups tethered in artificial mimicked environment to understand their interactions with nuclear transport receptors.

## **2. IDPs in diseases and cancer**

In fact, a wide range of human diseases known as protein conformation or protein-misfolding diseases comes from the failure of a particular protein to adopt its functional conformational state. The typical consequences of misfolding are the protein aggregation, loss of the normal function, and convert to abnormal function (97-101). In each of these abnormal states, a specific protein converts from its natural soluble state into insoluble fibrils, which as a result can accumulate in a variety of organs and tissues (96).

Amyloid fibrils show different properties including a core cross- $\beta$ -sheet structure (102). They are composed of 2 to 6 unbranched protofilaments 2 to 5 nm in diameter linked laterally or twisted together to form fibrils 4 to 13 nm in diameter (103). However, recent results showed that many proteins changed to diseases can form fibrils (104). Probably, any protein can fibrillate if found in the suitable conditions.

Numerous well-known cancer-related proteins with confirmed IDPs include p53 (105), BRCA1 (106), HPV protein (107), PTEN (108), and an massive majority of the Cancer/Testis Antigens (CTAs) (109).

## **3. The disordered nature of FG Nups**

It has been reported that the FG-domains are intrinsically unfolded domains (110). This study is well-known in the field, and no doubts that the contributions to the permeability



barrier are coming from disordered regions of the Nups. Previous studies have indicated that, at higher concentrations, FG-domains can aggregate to form amyloid-like shapes (111) or form some amyloid fibers. However, the physiological function of these amyloid fibers is still unclear. Under special conditions, FG-domains may convert to prone-type to form amyloid structures (112). However, if one determines the variability of FG-domains and the rather low conservation between species, it is clear that many mechanisms included in the NPC regulation remain unrevealed, even if the field could agree on a one working model of the transport barrier. It would be typically very important to reconstitute the NPC in vitro, so that its function could be revealed. The formation of synthetic nanopores (113, 114), and the design of functional NPCs in cells with a small number of FG proteins (115) are important steps to solve the complexity of the full NPC transport machine. Another particularly powerful tool is single-molecule live observation of the NPC machinery, as it affords a direct image in cells of how single transport events are occurred.

In this study, I directly visualized the conformations of IDP FG-Nups and central plugs of NPCs using high-speed atomic force microscopy (HS-AFM) that can observe proteins in action at high spatiotemporal resolution. Unlike the conventional static views of central plugs from EM, the dynamic mobility of central plug within nuclear pores in cancer cells such as HCT116 are shown. HS-AFM images of FG-Nups from aggressive cancer cell lines reveal highly diverse and transient oligomeric loop-knot formation reminiscent of central plug formation. HS-AFM images of single FG-Nup filament-tracking inside NPC turnstile revealed highly elastic bending motions in cancer cells which were rarely found in normal cell.

## MATERIALS AND METHODS

### 1. FG-Nups Analysis

Ultra-high speed was used to image the FG-Nups inside the NPC central channel to determine the behaviour of this selective barrier in mammalian cells. Reaching a maximum speed of 100 ms/frame was used to scan a  $40 \times 40 \text{ nm}^2$  scan area inside the central channel of NPC. The FG Nup results shown here were representative of my best resolved data. A fast Fourier transform (FFT) bandpass filter was used with a maximum of 20 pixels for large structures, a minimum of 3 pixels for small structures, and a tolerance of 5%. FFT processing method was used only to filter large and small structures to see the fine FG-Nups. Later processing of the original data was used to observe the FG-Nups over elapsed time using image lookup tables (26).

### 2. Image Processing

The HS-AFM movies were processed to remove thermal drift in x, y and z-directions and to reduce the high frequency noise in x, y direction (z-scanner noise) by Image J software. First, the horizontal noise was reduced by the median filter with 2.0-radius. Second, the z-directional drift was removed by background subtraction of each frame with the primary functions in x- and y-directions, which resulted in no difference in average height between frames. At last, the horizontal drift was removed by using the template-match algorithm, where each frame was translated in xy-plane to maximize a normalized cross correlation coefficient between the frame being translated and the reference frame.

### 3. Measuring the bending angles of single FG Nup filaments

The bending angle calculated using *Gwyddion* software, measuring how much bending away from the NPC scaffold axis by using the line tool, then measuring the angle of this line which is parallel with the FG Nup filament. I selected the very clear single filaments only and excluded the entangled filaments from my measurements.

#### **4. Single filament dissection**

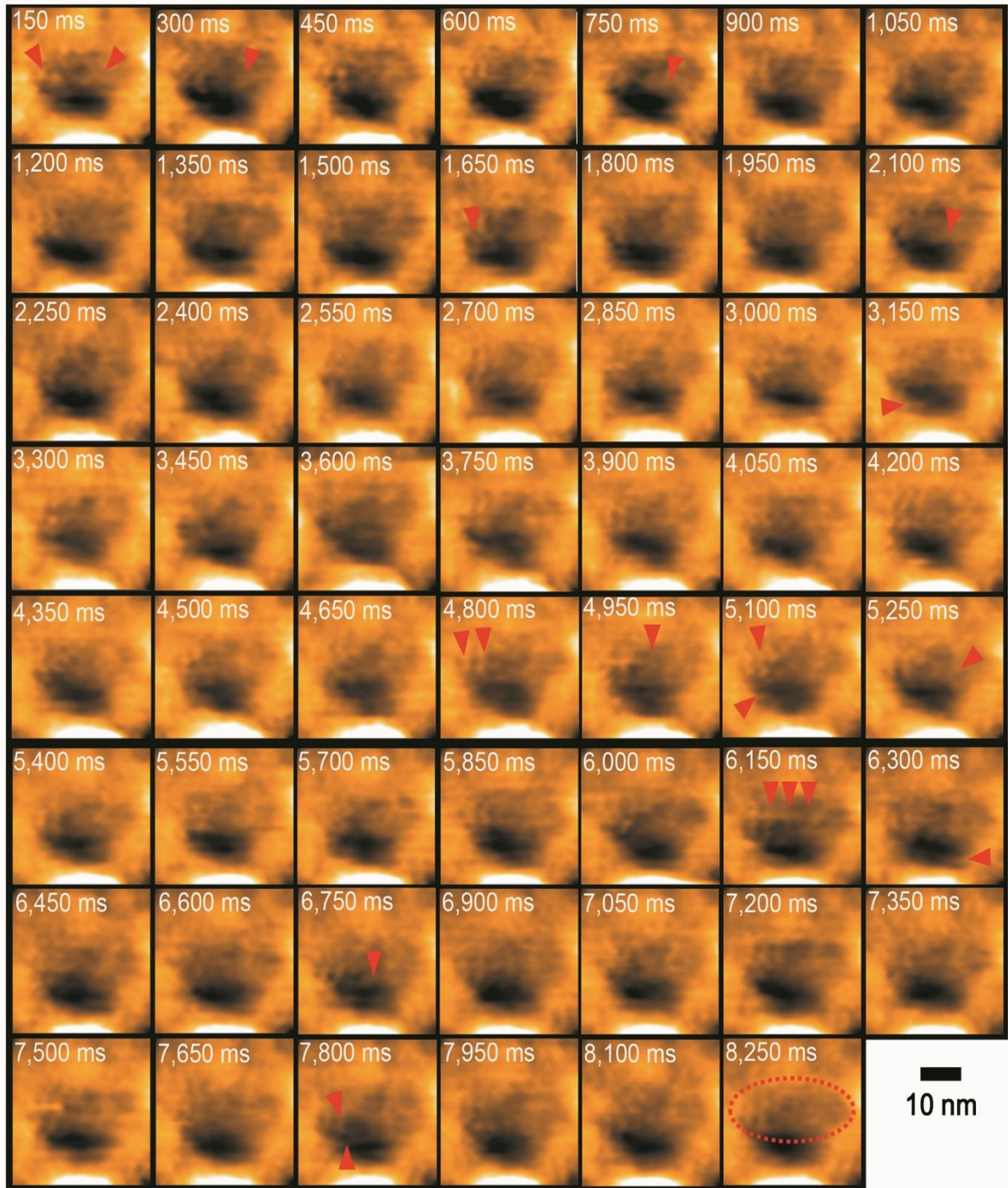
The single filament dissection performed by taking 5 cross sections at different positions along the entire FG filament starting from the point near to the tethering point reaching to the free end inside the central channel. Then, comparing the different cross sections from different points to show the thin and thick points along the filament entire length.

## RESULTS

### 1. Tracking of FG Nups inside native NPCs of colon cancer cells

To resolve FG-Nup behaviour that form the selective barrier, I focused on the central channel enclosed by the cytoplasmic outer ring and increased the scan rate to 6.7 frames/s (150 ms/frame). A post-experiment image processing was then performed to align successive images in the x–y plane and to rectify for drift in the z direction (65). I revealed both; native and drug-treated FG-Nup networks by HS-AFM. The extended and retracted FG-Nups appeared to have brush-like conformational changes (Figure 26, 27). I contemplate that FG-Nups pattern during transport with different physical properties of both entropic (“brush-like”) and enthalpic/cohesive hydrophobic (“gel-like”) concepts may be revealed in the near future.(81).

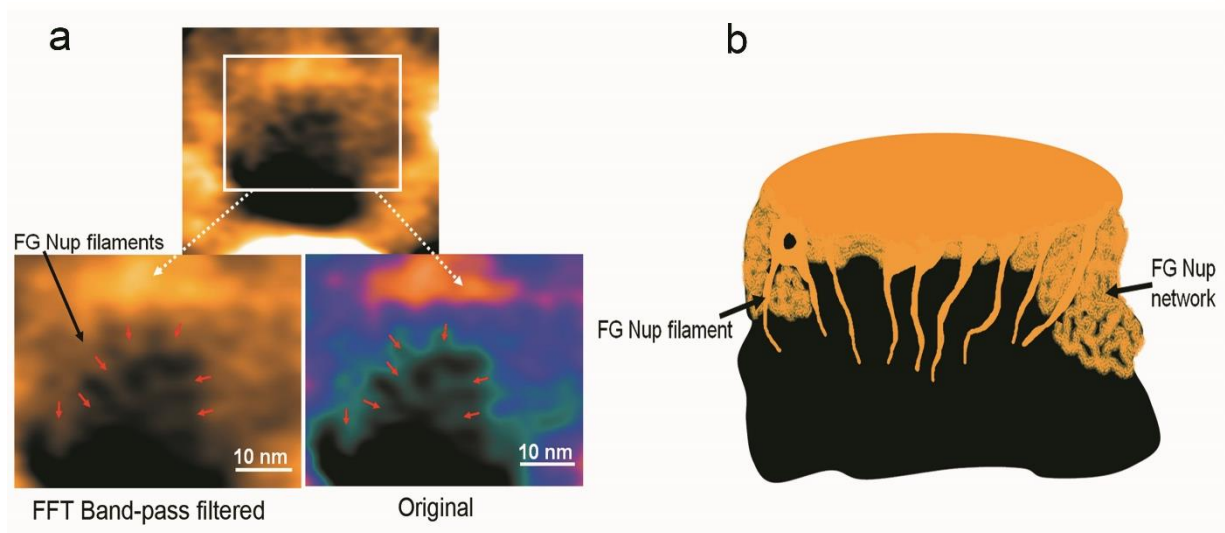
Precise basic image filtrations revealed a flexible fast motion of FG-Nups that frequently extended and retracted inside the central channel of NPC (Figure 28a). This data is similar to those observed by HS-AFM in studies of intrinsically disordered proteins (82) and of *Xenopus* NPC FG-Nups(65). FG-Nups appeared as short, stiff, hair-like, filaments that have a brush-like pattern or form a broken cobweb mesh from their tethering points (10), which suggests the same characteristics of virtual gating.(83) The average length of FG-Nup filaments ranged from 5.1 nm (during contracted state) to 20.9 nm (during extended state) in the control, but I determined that after MLN8237 treatment the sequential changes of FG-Nups were noticed infrequently (ranging from 5 to 11 nm) even under the time of 300 ms/frame (Figure 21b).



**Figure 26. HS-AFM imaging of FG-Nups.** Sequential HS-AFM frames recorded at 6.7 frames/s of a  $40 \times 40 \text{ nm}^2$  region inside the central NPC channel of wild-type HCT116 cells with  $200 \times 200$  pixels. The original HS-AFM images were processed using an FFT bandpass filter to show only the tiny FG filaments interacted inside the central channel. Red arrows refer to FG-Nup filaments entangled inside the channel and in many images forming a network, like the one that appeared at time point 8250 ms; scale bar is 10 nm.

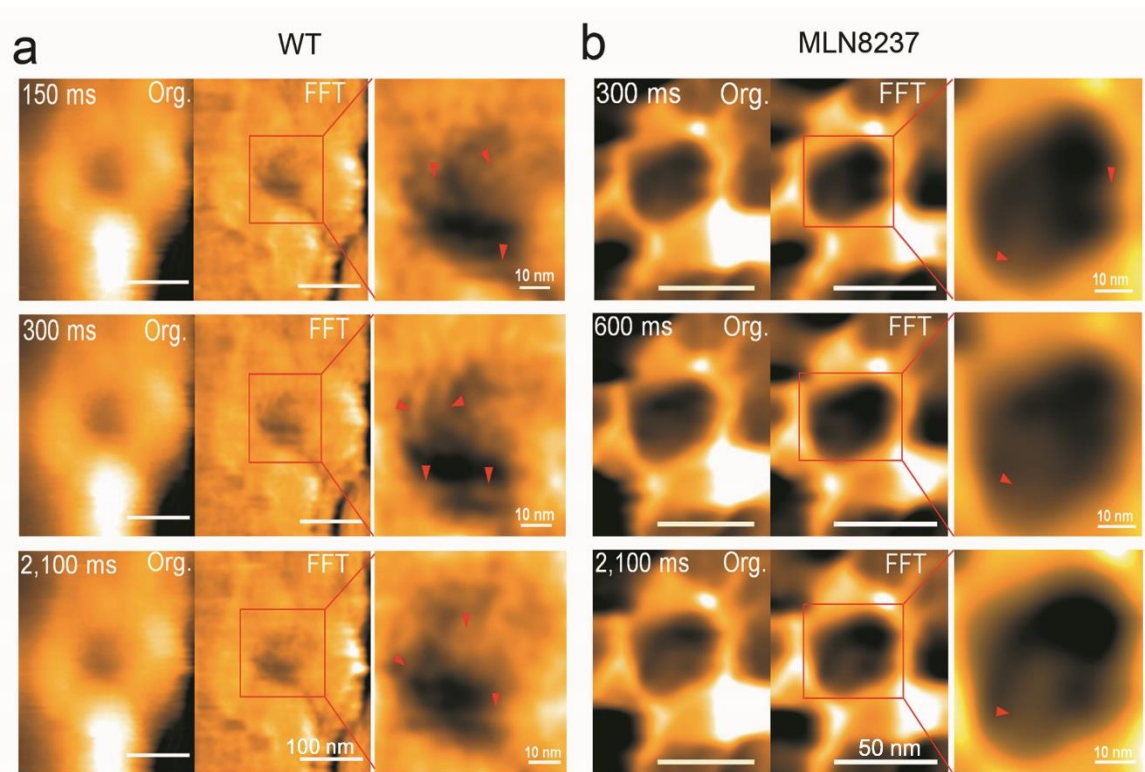
## 2. Spatiotemporal averaging of native FG Nups of colon cancer cells

To deeply resolve FG-Nup dynamic patterns, I concentrated on a  $40 \times 40 \text{ nm}^2$  scan size squarely on the central channel of NPC. The HS-AFM playbacks showed a remarkable abnormal changes in the spatiotemporal pattern and a tractability loss of the FG-Nups network inside the central channel (Figure 29a,b). The single FG-Nup thickness was measured by cross-sectional analyses as  $0.6 \pm 0.3 \text{ nm}$  (in control pores;  $N = 20$ ) compared with  $0.2 \pm 0.2 \text{ nm}$  (in MLN8237-treated pores;  $N = 20$ ) (Figure 30a,b). In MLN8237-treated NPCs, the FG-Nup thickness over time was strongly reduced (Figure 30c). In addition, the FG-Nup original points and flexibility appeared to be lost in these dying NPCs. Therefore, the data of cross-sectional analyses inside the central channel indicated that the spatiotemporal behaviour of the single FG-Nups and FG-Nups density is decreased upon the treatment with MLN8237 (Figure 30).

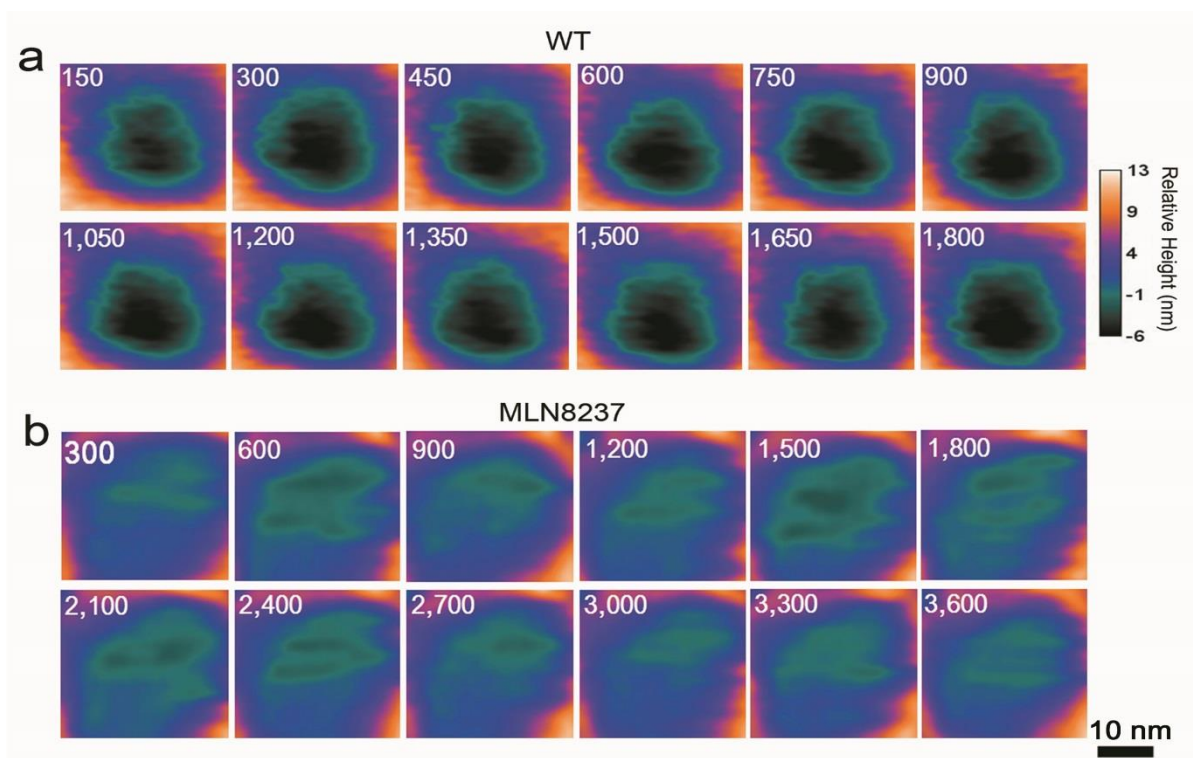


**Figure 27. Live tracking of FG-Nups inside the inner channel.** (a) HS-AFM image magnified to indicate the extended FG-Nup filaments tethered from the NPC inner ring. (b) Illustration of the FG-Nup filaments in (b) indicating their extension inside the NPC central channel.



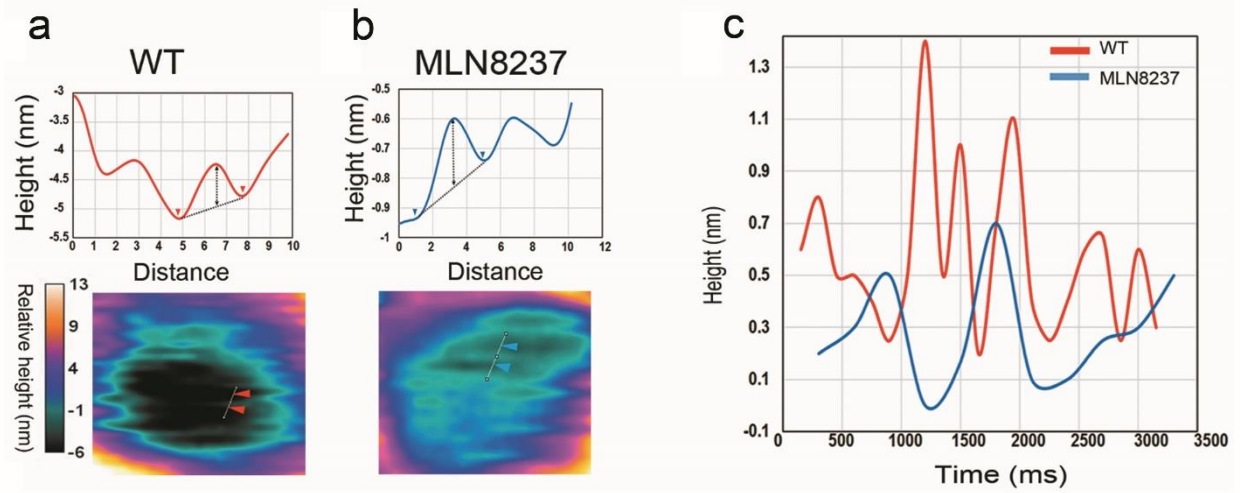


**Figure 28. FG-Nups tracking by HS-AFM.** (a) Original and FFT-filtered images are shown in this figure to show the presence of FG-Nups inside the central channel. Red arrows indicate fast changes in FG-Nups in three different images of WT NPC (Scan speed = 6.7 frames/s). (b) Original and FFT-filtered images of MLN8237-treated NPC are indicated to show the loss of FG-Nups inside the central channel after the cell death induction. Red arrows show the remaining FG-Nups, observed in only few images (Scan speed = 3.3 frames/s).

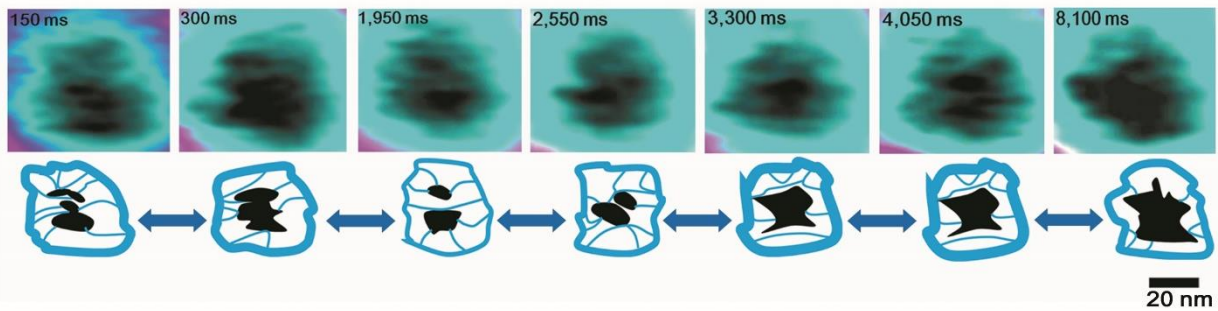




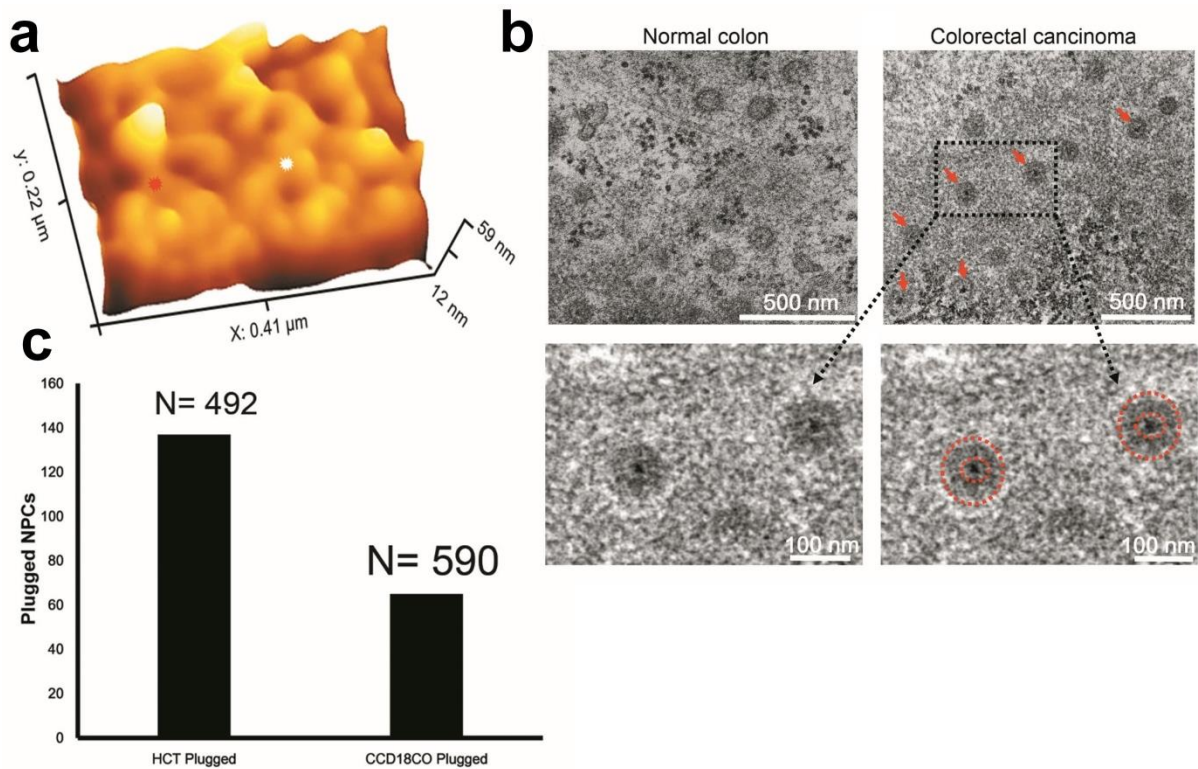
**Figure 29. HS-AFM imaging of FG-Nups after MLN8237 treatments in HCT116 cells.** (a) HS-AFM image showing the conformational changes inside the central channel including the single FG-Nups barrier of WT pore showing flexible changes of FG-Nups networks inside the channel over the elapsed time with rapid arrangements in the entangled FG-Nups threads (Z-scale = 19 nm, speed = 6.7 frames/s) with  $200 \times 200$  pixels. (b) MLN8237-treated pore showing a loss of the FG-Nups network in different successive frames (Z-scale = 19 nm, speed = 3.3 frames/s) with  $200 \times 200$  pixels; scale bar, 10 nm. The numbers on each frame refer to the elapsed time in milliseconds.



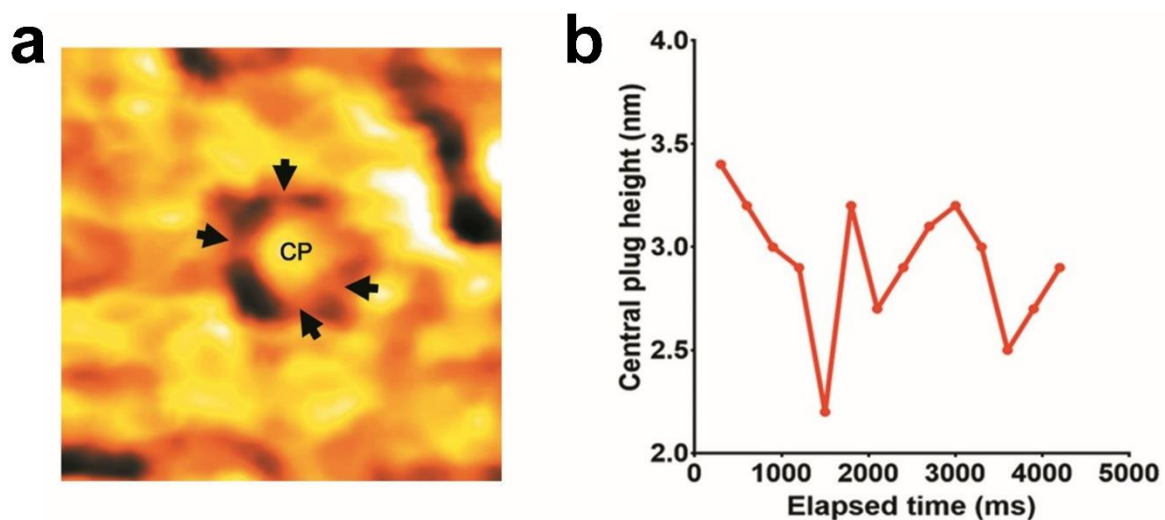
**Figure 30. Cross-sectional analysis of FG-Nups in HCT116 cells.** (a) Cross-sectional analysis inside the central channel showing the average height profile of FG-Nup threads in the WT NPC ( $n = 20$ ). Average height (thickness) =  $0.6 \pm 0.3$  nm. (b) Cross-sectional analysis inside the central channel showing the average height profile of FG-Nup threads in the MLN8237-treated NPC ( $n = 20$ ). Average height (thickness) =  $0.2 \pm 0.2$  nm. (c) Heights of FG-Nups measured at different time points plotted against the elapsed time to show the dynamic changes of individual threads in a time-dependent manner in WT and MLN8237-treated NPCs.



**Figure 31. FG Nup-Cobweb conformational sequential conformations.** HS-AFM images showing an extension of the FG-Nups analysis in. A  $40 \times 40$  nm<sup>2</sup> area (Z-scale = 19 nm) of the central channel was imaged using the higher speed of 6.7 frames/s to show the behavior of the FG-Nups network. Different frames show conformational changes of FG threads retracting and diffusing and sometimes forming a network that looks like a cobweb.



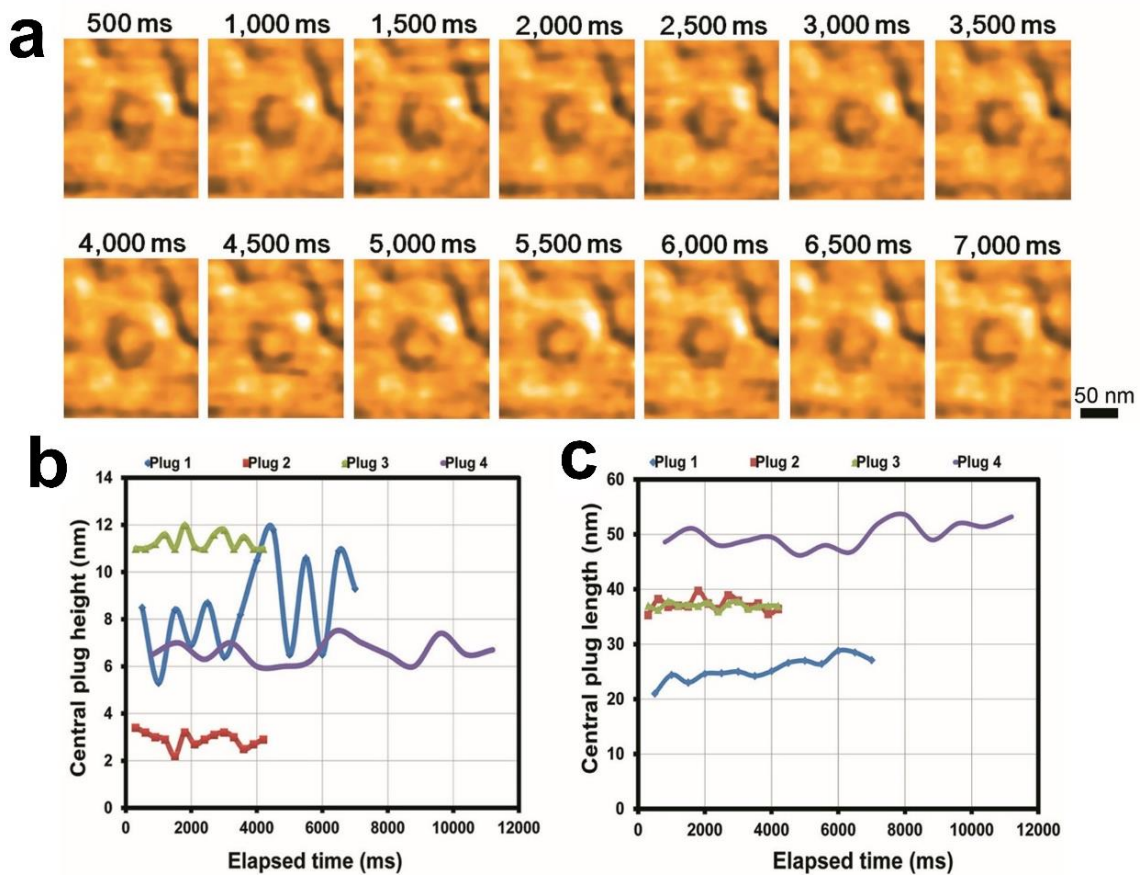
**Figure 32. Central plug in colorectal carcinoma vs normal colon cells.** (a) HS-AFM image rendered in 3D format for the cytoplasmic face of nuclear envelope of HCT116 cells showing plugged and plug-free NPCs. (b) EM micrograph showing NPCs of CCD18CO cells and EM micrograph of HCT116 cells showing many plugged NPCs (red arrows). The below panels showing magnification of some plugged NPC from HCT116 cells (red circles). (c) Percentage of plugged NPC in both HCT116 and CCD18CO cells, N = 492 and 590 respectively.



**Figure 33. Central plug dynamics.** (a) HS-AFM image showing plugged NPC and CP in clear connections with FG filaments to the tethering points (b) Central plug height plotted against elapsed time to show the dynamic conformations of CP inside the central channel.

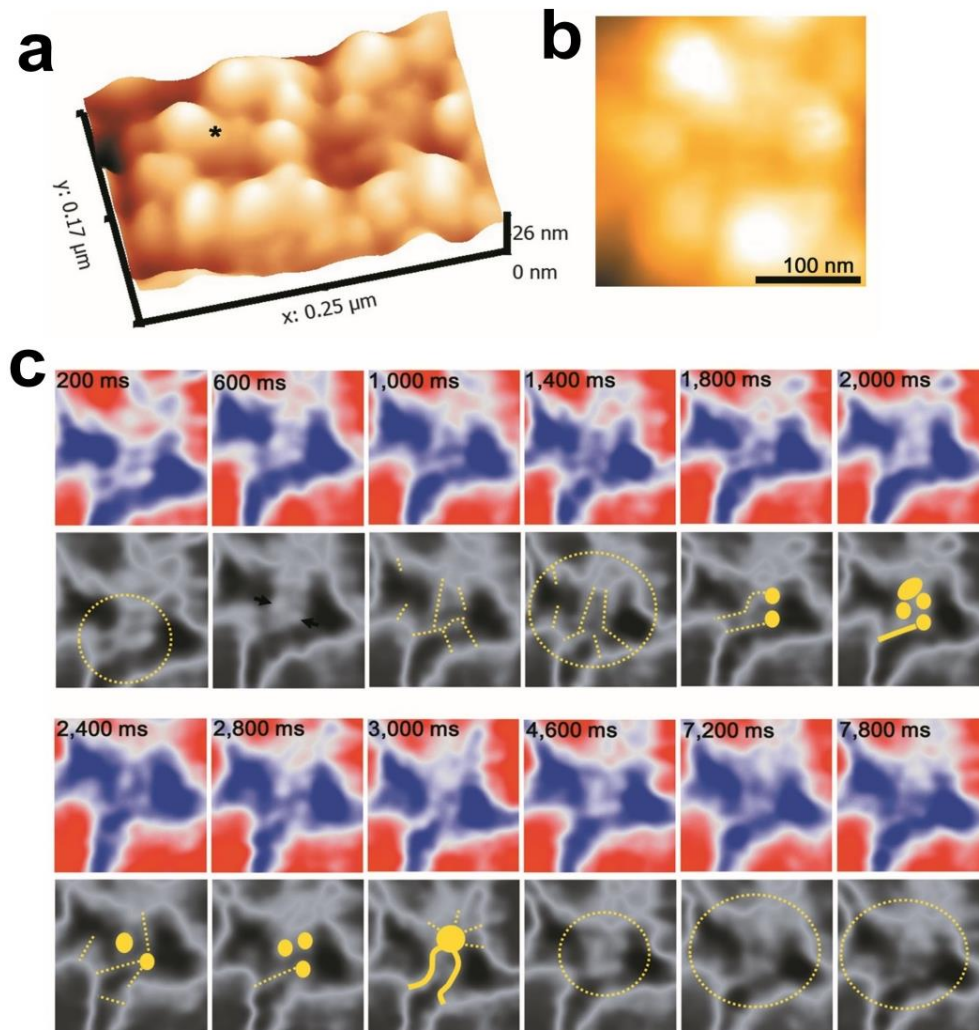
### 3. Central plug (central transporter) dynamics inside the central channel in colon cancer cells

In HCT116 cells, I found the existence of central granules inside a part of nuclear pores as shown in [Figure 32](#) about 25% of NPCs are plugged in HCT116 and 10% in normal colon cells CCD18CO. To determine the central plug dynamic in nanoscale, I first observed structural dynamics of central plug at a sub-molecular level by HS-AFM, which is capable to visualize protein complexes and organelles in action at a good spatiotemporal resolution. I found that the central plug shape was changed ([Figure 33](#)). I found that the FG filaments thickness had rapid conformation which connected CP to the NPC outer ring. [Figure 34](#) showing successive conformational changes of HCT116 CP, which means that CP has no specific size of shape. This is confirmed by cross-sectional analysis in [Figure 34b, c](#) showing the changes of CP heights and lengths over the elapsed time in different NPCs.





**Figure 34. Central plug dynamics resolved by HS-AFM.** (a) HS-AFM Successive images of plugged NPC showing the dynamics of the central plug inside the central channel. Z range = 60 nm, scanning speed is 2 frames per second. (b) Plot of Height of four different plugs plotted against the elapsed time to show the dynamics of individual plugs. (c) Plot of length or diameter of four different plugs plotted against the elapsed time to show the dynamics of individual plugs.

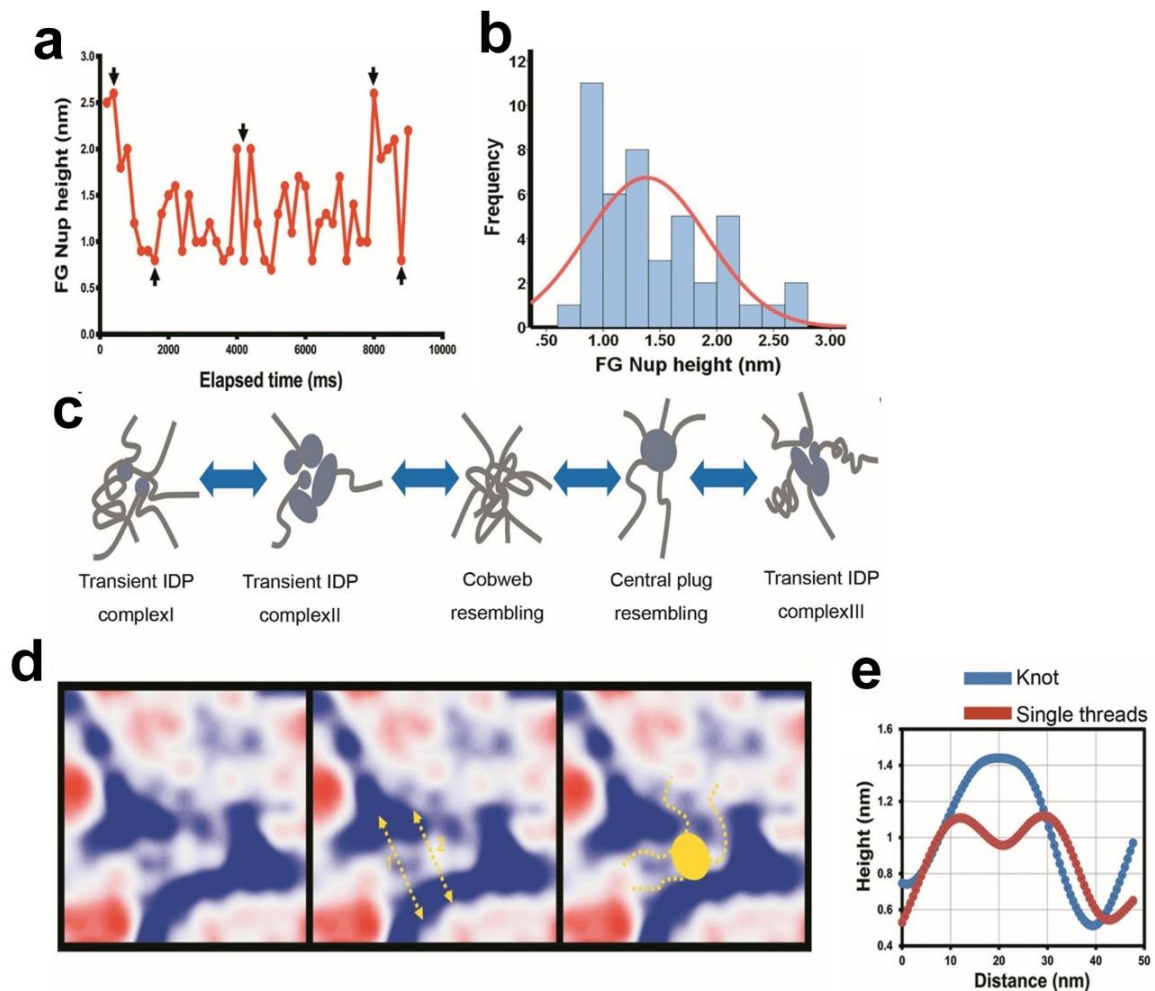


**Figure 35. Transient IDP-FG conformations inside the central channel resembling central plug.** (a) HS-AFM image of the cytoplasmic face of nuclear envelope of HCT116 cells rendered in 3D mode, showing intact symmetric NPCs. Z-range is 26 nm, scanning speed is 1.7 frames per second, 200×200 pixels. (b) Single representative NPC, Z-range is 13 nm, scanning speed is 5 frames per second, 200×200 pixels. (c) Successive HS-AFM images showing rapid conformations of native FG-IDP Nups inside the central channel. Many transient FG-IDP complexes appearing for few milliseconds and then turning to another IDP complex.

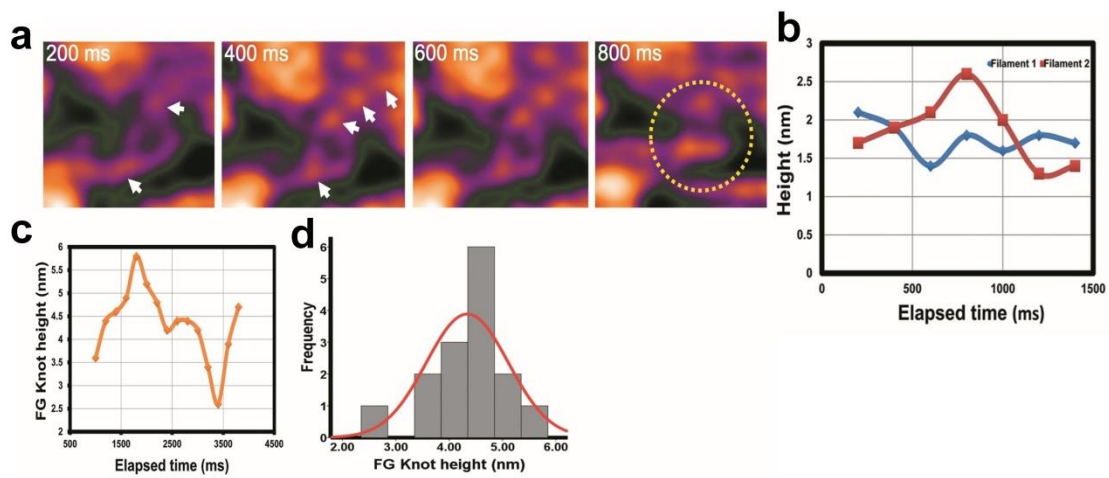
#### 4. Transient conformations of IDP-FG Nups

Indeed, I did observe transient loops and knots rapidly formed (Figure 35).

I measured the height and frequency of FG-Nups was actively under different conformation (Figure 35c). I showed two single FG Nup filaments twisting over each other forming FG-knot (Figure 36). These data indicate that transient rapid confirmation of IDP FG-Nups complexes inside the native NPCs. Similar to the diffusive motion of IDP and our recent observation, I found the swaying motion of polypeptide chains being the FG Nups that repeatedly extend and retract in the central writhe like turnstile; FG Nups were forming bristle in a writhe like cobweb manner from their tethering points.



**Figure 36. FG knot formation and CP resembling.** (a) Heights of entangled FG Nups measured at different time points plotted against the elapsed time to show dynamic and rapid conformations of Cobweb network, black arrows refer to highest and lowest FG Nup heights observed at different conformational patterns. (b) Shows the normal distribution curve of FG Nup filaments height shown in a. (c) Diagram showing different conformational changes of Cobweb network; including different transient FG-IDP complexes. (d) HS-AFM images showing two single FG Nup filaments twisting over each other forming FG-Knot (indicated by the solid yellow circle). (e) The plot showing the cross sections taken on the single filaments and the FG-Knot, which demonstrate the mechanism of Cobweb formation inside the central channel.



**Figure 37. FG Knot formation visualization by HS-AFM.** (a) HS-AFM sequential frames showing the live twisting 2 FG filaments to form a thick FG knot. (b) Cross-sectional analysis showing the height profile of the twisted filaments over the elapsed time. (c) Height profile of FG knot over elapsed time. (d) Normal distribution curve of FG knot height ~ 5 nm.

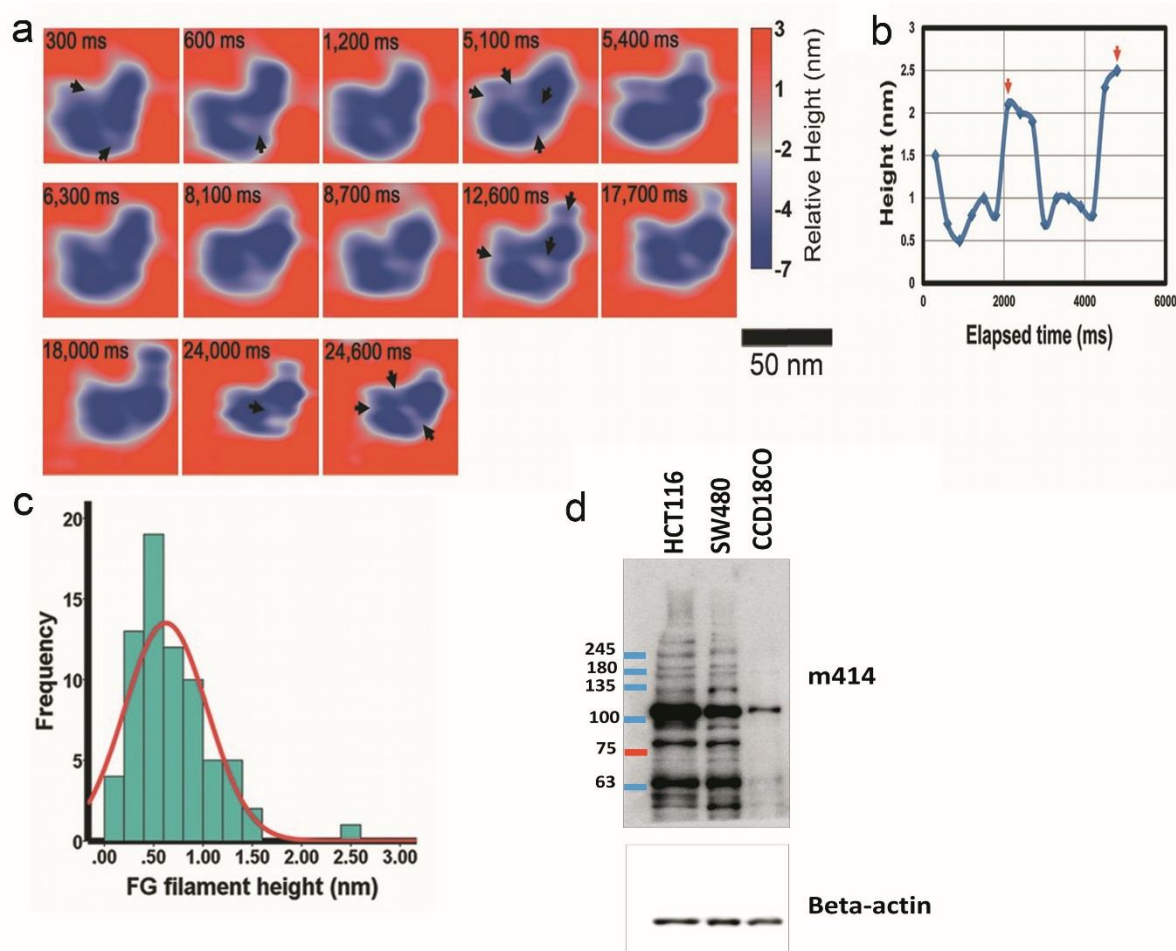
Even though the molecular fluctuations occur on the microsecond timescale (26, 65), so the exact trajectories of individual FG-Nup remain inaccessible at current HS-AFM scan speed. Remarkably, I found that the HS-AFM images exhibited distinct structures of FG Nups in the central after I raised the scan rate to 6.7 frame/s (150 ms/frame)/max. limit. In particular, extended FG Nups that coincide and intermingle in the central whip-like turnstile showed the appearance of a transient cobweb-central plug (Figure 35, 36). Next, to take a close look of these FG “flagellar knots”, I calculated the height and distance of these transient FG-Nups threads knots (Figure 36, Figure 37), I found that these ~5nm threads knots were considerably

smaller in size ( $1.7 \pm 0.5$  nm) than the hydrodiameters of a karyopherin (karyopherin $\beta$ 1 ~10nm) (65) or larger cargo (>5nm) and should not be misguided for cargoes in transit. Together, these HS-AFM movies clearly showed that the individual IDP FG Nup undergoes a extend and retract writhing in the central NPC cobweb and recalled one of the most controversial feature of the NPC- the central plug biogenesis, a large mass observed in the centre of many but not all NPCs ( 26 ).

## **5. HS-FM observations of FG Nups in normal colon cells**

In colon cancer cells, I found highly dynamic FG Nup filaments inside the central channel. In addition, I found many complex conformations of the IDP-FG Nups forming knots and twisting over each other. Also, I found a percentage of central plugs blocking some pores and interaction of the FG filaments. I further investigated the pattern of FG Nups distribution in the normal colon cells and made a comparison with the tumour cells. I found that FG Nup density in normal colon NPCs is lower that of tumour ones as shown in Figure 14. The FG Nup thickness was consistent with colon cancer cells as shown in [Figure 38c](#)  $\sim 0.6 \pm 0.4$  nm (N=71). Red arrows in [Figure 38b](#) indicate two thick FG Nup aggregates which observed near the inner channel wall.

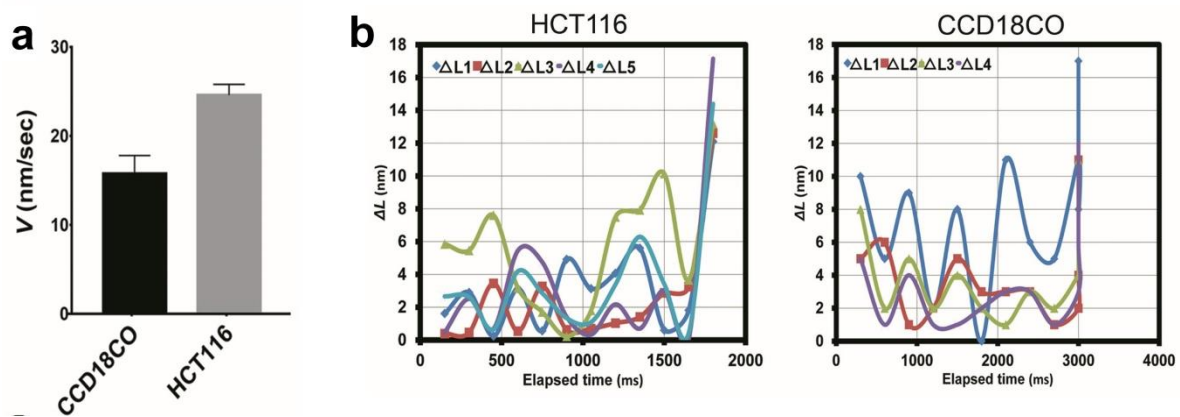




**Figure 38. FG-IDP single filament-tracking in healthy native NPCs.** (a) Successive HS-AFM images showing FG filaments dynamics inside the native central channel of CCD18CO cells. Black arrows referring to single filaments extending form their tethering points at the NPC scaffold. Z-range is 13 nm, scanning speed is 3.3 frames per second, 200×200 pixels. (b) Single FG filament height plotted against the elapsed time in CCD18CO NPCs. The average height  $\sim 0.6 \pm 0.4$  nm (N=71). Red arrows indicate two thick FG Nup aggregates which observed near the inner channel wall. (c) Shows the normal distribution curve of FG Nup filaments height shown in b. (d) Western blot analysis of m414 antibody in colorectal cancer and normal colon cells.

## 6. Extension velocity of single FG filaments

After I determined a difference in FG Nups density and distributions between normal and colon cancer cells. I tried to go more deeply to distinguish the single filament behaviour in both normal and cancer. Individual FG filament length-change velocity measured by calculating the length-change over different time points as shown in Figure 39a,b. The extension velocity of single FG filaments in cancer cells was significantly higher than in normal cells. Taken together, these results gave an indication of FG Nups behaviour in normal and cancer cells.

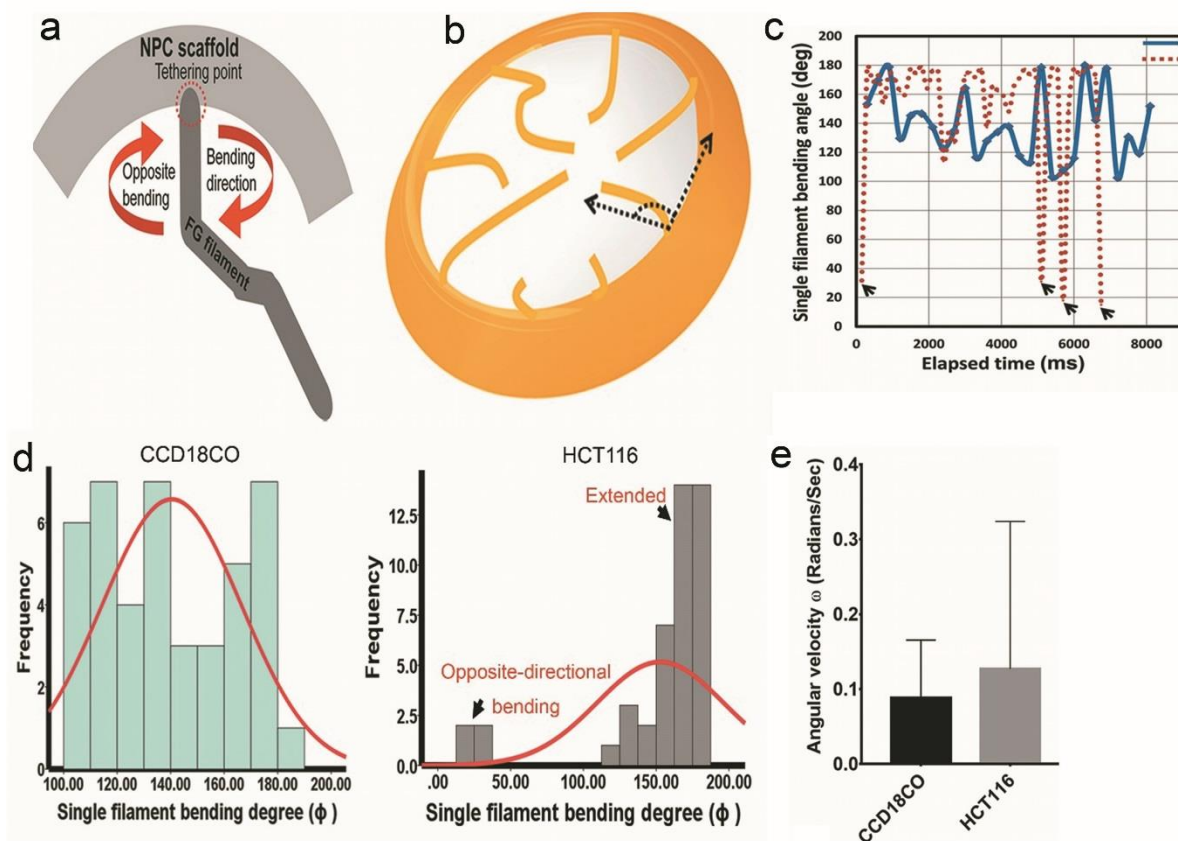


**Figure 39. Single FG filament extension velocity.** (a) Individual FG filament length-change velocity measured by calculating the length-change over different time points. (b) Graphs showing FG filament length-change over elapsed time in both cancer and normal cells.

## 7. Single FG filament bending angle

To investigate more about the behaviour and dynamics of single FG filaments in both normal and cancer, I did measure the bending angles of single filaments inside the central channel. Figure 40 a,b is a diagram showing the bending possibilities of FG Nup filaments in two different directions away from their tethering points. And the angle measurements shown in the diagram on the right; shows the extending and retracting FG filaments inside the central channel of NPC. The bending angle calculated using Gwyddion software in the shown

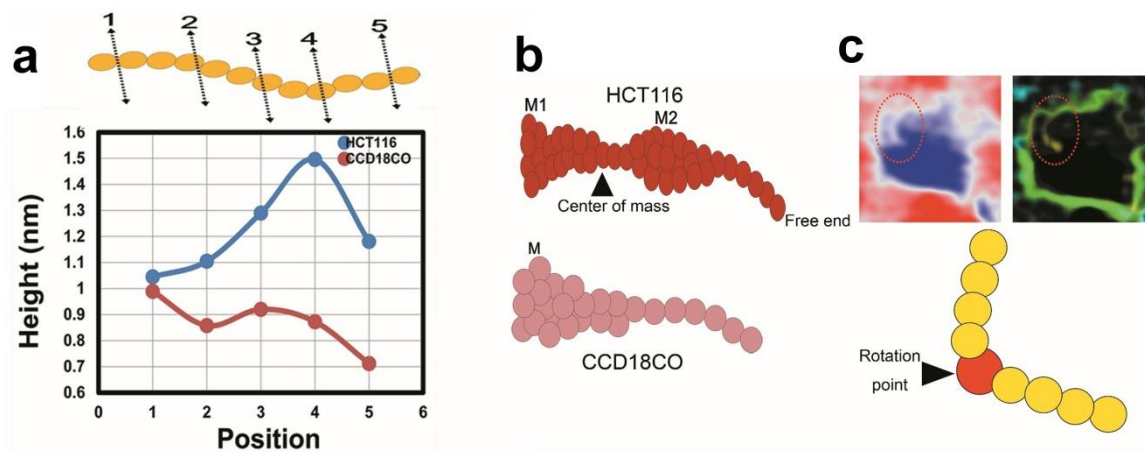
method, measuring how much bending away from the NPC scaffold axis. FG Nup filament bending angle plotted against the elapsed time to track the bending of single filaments away from the scaffold NPC. This plot in [Figure 40c](#), showing the different bending angles of HCT116 and CCD18CO. The average bending angle was  $\sim 153 \pm 43$  degree in HCT116 (N=45) and  $\sim 140 \pm 25$  degree in CCD18CO (N=45). Black arrows indicate some points the bending happened at the opposite direction of all other bending points. Also, the normal distribution curve of FG Nup filament bending angle in CCD18CO and HCT116. In HCT116, the highest frequency noticed in the fraction 170 – 180 degree which corresponds to the extended FG filaments. A small fraction of very narrow bending angles noticed which correspond to the opposite-directional bending of FG filaments, which indicate the high flexibility of FG filaments in HCT116. [Figure 40e](#) is a plot showing the angular velocity of individual FG filaments in both CCD18CO and HCT116 as calculated from the same filaments shown in c.



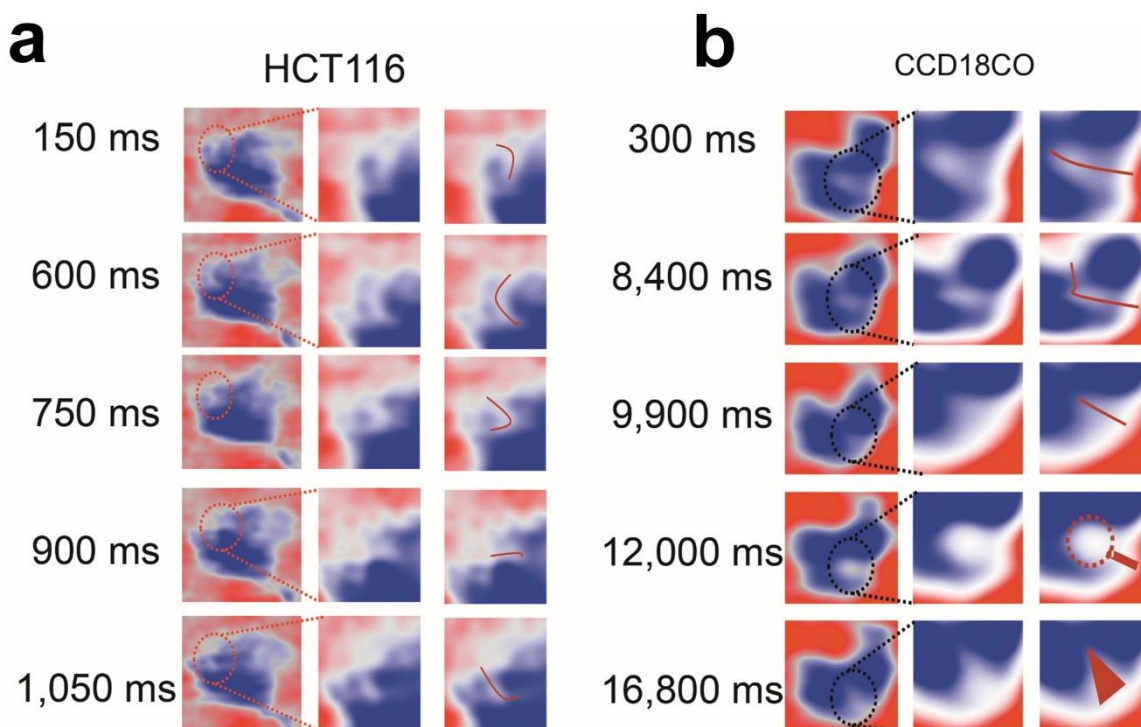
**Figure 40. Bending abilities of single FG filaments measured in normal and cancer.** (a) Diagram showing the bending possibilities of FG Nup filaments in two different directions away from their tethering points. (b) The angle measurements shown in the diagram on the right; shows the extending and retracting FG filaments inside the central channel of NPC. The bending angle calculated using Gwyddion software in the shown method, measuring how much bending away from the NPC scaffold axis. (c) FG Nup filament bending angle plotted against the elapsed time to track the bending of single filaments away from the scaffold NPC. This plot showing the different bending angles of HCT116 (red dotted line) and CCD18CO (blue line). The average bending angle was  $\sim 153 \pm 43$  degree in HCT116 (N=45) and  $\sim 140 \pm 25$  degree in CCD18CO (N=45). Black arrows indicate some points the bending happened at the opposite direction of all other bending points. (d) Shows the normal distribution curve of FG Nup filament bending angle in CCD18CO and HCT116. In HCT116, the highest frequency noticed in the fraction 170 – 180 degree which correspond to the extended FG filaments. A small fraction of very narrow bending angles noticed which correspond to the opposite-directional bending of FG filaments, which indicate the high flexibility of FG filaments in HCT116. (e) A plot showing the angular velocity of individual FG filaments in both CCD18CO and HCT116 as calculated from the same filaments shown in c.

## 8. Single FG filament dissection model

The different abilities of bending of FG filaments in both normal and cancer cells prompted me to investigate the mechanism behind this interesting behaviour of the single nano-IDP filaments. Thus, I performed a single filament dissection along the entire length of FG filaments in both normal and cancer cells as shown in Figure 41a. So, to confirm that, I did a single filament dissection by taking 5 cross sections at different positions along the entire FG filament starting from the point near to the tethering point reaching to the free end. Interestingly, I found that FG filaments of HCT116 have two thick points or I called masses (M1, M2) along the entire filament. However, in CCD18CO, the FG filaments have only one thick point (M) near the tethering point. In HCT116; having two thick point is giving an advantage to make an stability for the entire filaments and controls different bending directions in a different way from CCD18CO which has only one thick point near the tethering point, which has few bending motions as shown in Figure 41b, c is a representative example for HCT116 FG Nup filament which has a bending ability (red circle). The point M2 shown in b, possibly working as a rotation point. Also, single filament bending and conformations shown in Figure 42a,b in both normal and cancer cells.



**Figure 41. Single FG filament bending model.** (a) FG filaments entire length dissection. (b) FG filament dissection result schematic showing thick points working as a rotation points. (c) HS-AFM representative image of single FG filaments captured in HCT116 NPCs.



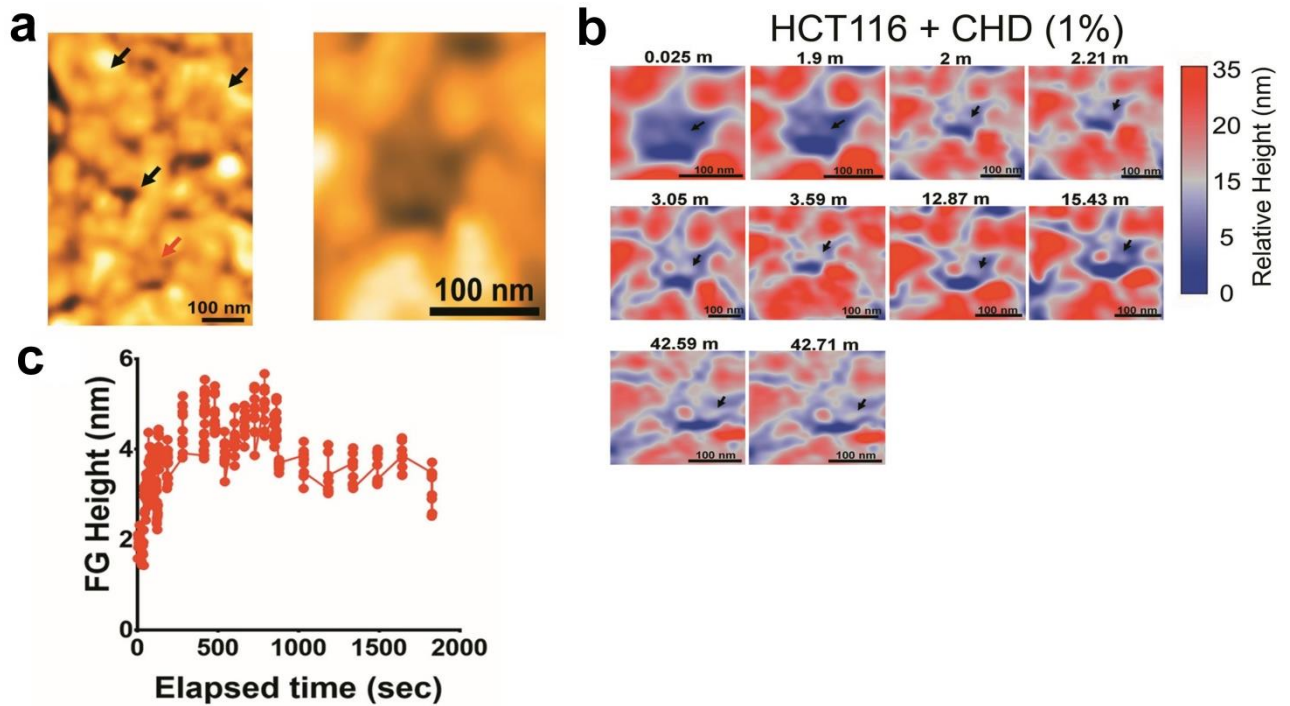
**Figure 42. Single FG filament bending and conformations in normal and cancer cells.** (a) HS-AFM successive images of single FG filaments bending inside the central channel in HCT116 cells. (b) HS-AFM successive images of single FG filaments in CCD18CO cells.

### 9. Effect of specific FG-inhibitor 1,2-hexanediol (CHD) on FG Nups behaviour

Next, I treated the NPCs with FG inhibitor, (CHD). HS-AFM image of the cytoplasmic face of nuclear envelope of HCT116 cells were treated with 1% 1,2-hexanediol/CHD (Figure 43). I used 1% concentration in these experiments to allow me to see the slow effect of this specific inhibitor on the behaviour of single FG filaments in its native state and environment. Because, in the higher concentration the effect was too fast (3% CHD caused 80% of cells detached in culture after 30 minutes). To visualize the effect of CHD treatment NPCs, I recorded the successive HS-AFM images showing live tracking of the effect of 1% 1,2-hexanediol on the single FG Nups inside the central channel, as the time increase, I found that many FG Nups aggregate gradually and small particles passively accumulate inside (Figure 43c). Next, I measured the heights of single FG Nups measured at different time points



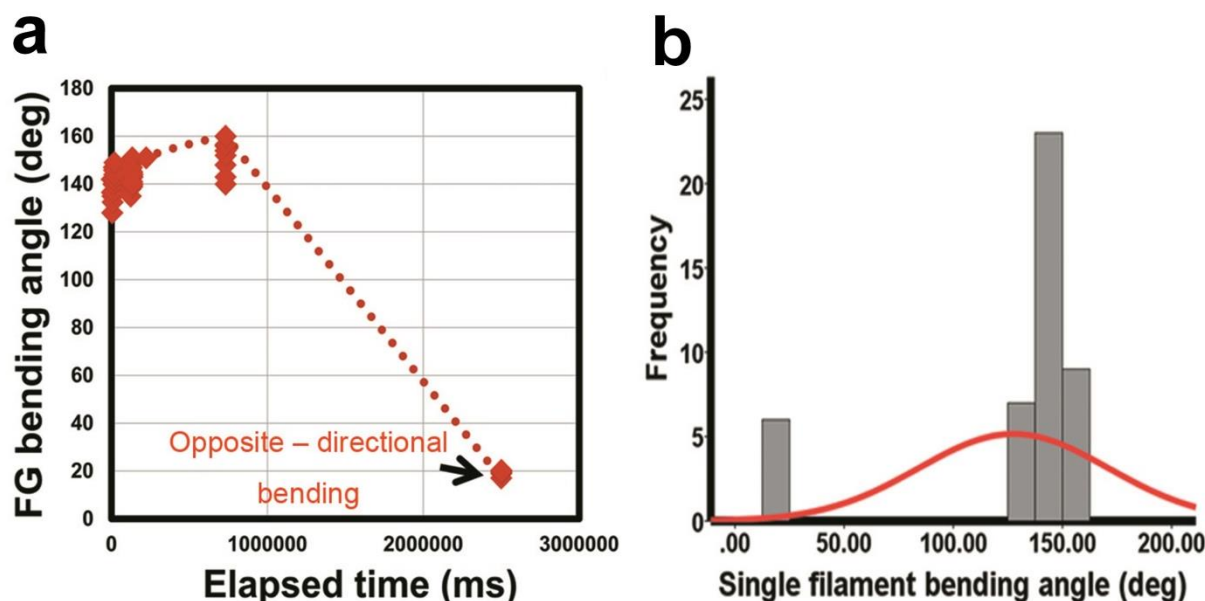
plotted against the elapsed time to demonstrate the effect of 1,2-hexanediol over 42 minutes. FG Nups appeared to be aggregated over the elapsed time reaching ~ 5 nm height and then started to degrade and decrease the height.



**Figure 43. Single FG Nups tracking after 1,2 hexanediol treatment.** (a) HS-AFM images showing several NPCs treated with 1,2 hexanediol (1%). The drug was added during the imaging to track the live changes in NPCs. Black arrows showing some representative dying NPCs, red arrow showing dilated NPC with aggregated FG Nups inside the central channel. Z-range = 110 nm, scanning speed is 0.7 frame per second. (b) HS-AFM successive images of 45 min recordings to track the changes of single FG Nup filaments upon adding 1,2 hexanediol (1%). The time-lapse movies showing significant increasing in the filament height. Black arrows showing a representative FG Nup filament tracking. Several conformational changes noticed including the NPC overall dilation, cytoplasmic filaments degradation and FG Nup aggregation. Z-range = 110 nm. (c) FG Nup height plotted against elapsed time to determine the sequential changes of FG Nup thickness under CHD treatment.

Besides, I also found the bending angle of single FG Nups plotted against elapsed time to show the effect of 1,2-hexanediol on the bending ability of individual FG Nups. FG Nups bend in one direction only under the CHD effect. However, after the time increased, it lost its ability to bend, and then bended in the opposite direction as it is already degraded (Figure 44).

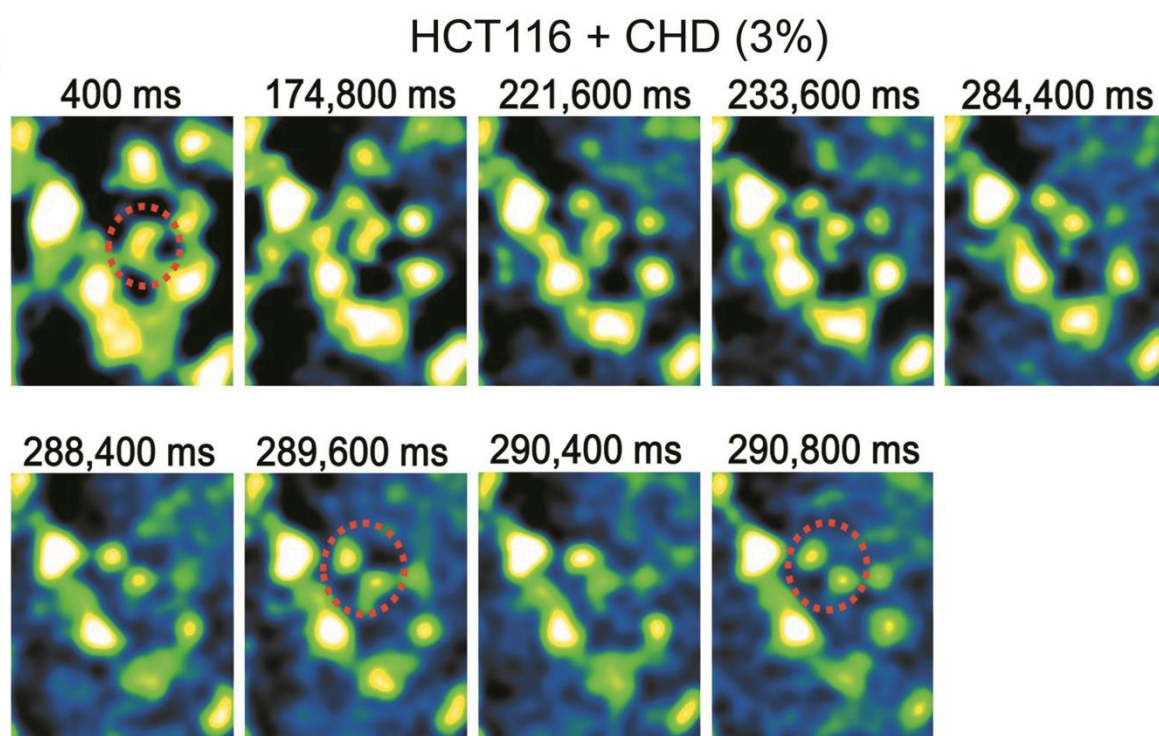




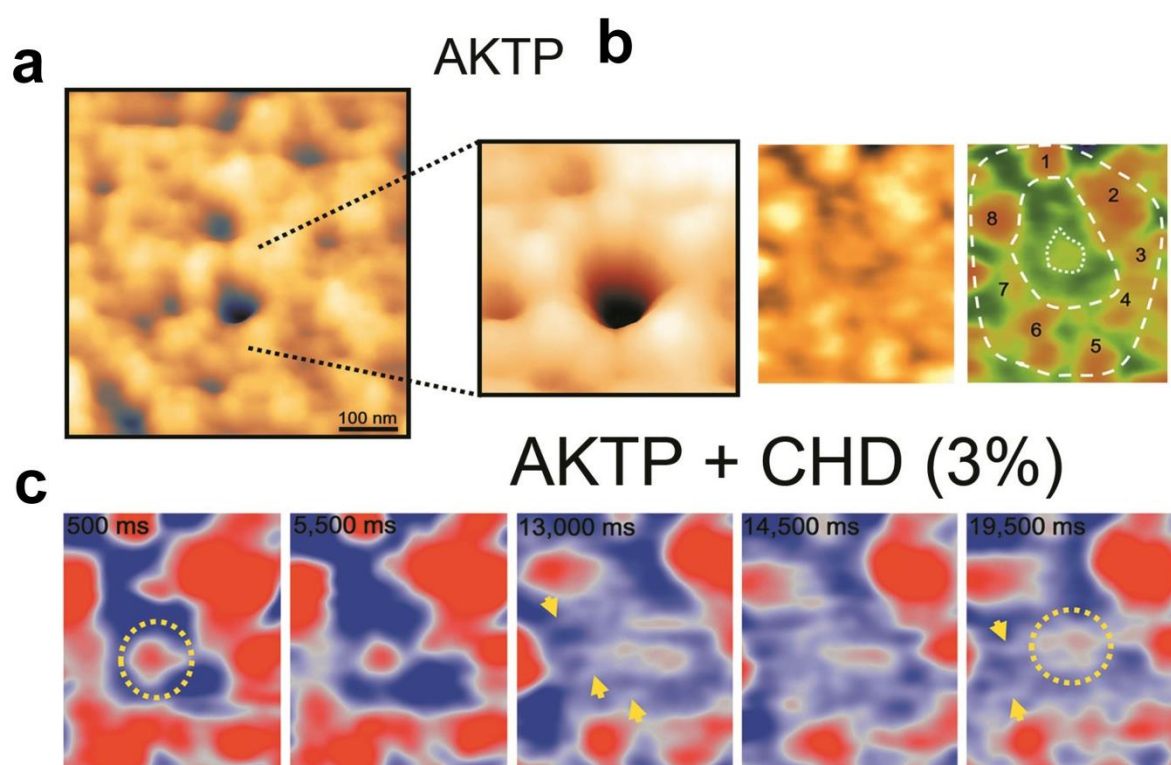
**Figure 44. Bending angle of FG filaments under the effect of 1% CHD.** (a) Single FG Nup filament bending angle is plotted against the elapsed time to show the effect of 1,2 hexanediol (1%) on the single filament bending dynamics. Black arrow is showing the significant decrease in the bending angle which correspond to the opposite-directional bending which noticed at a late stage of the dying process of NPCs. (b) Normal distribution curve of bending angles.

## 10. Testing the effect of FG-specific inhibitor (CHD) on central plug dynamics

Next, to investigate the effect of CHD on central plug, I recorded HS-AFM image showing a plugged NPC observed at the cytoplasmic face of HCT116 cells (Figure 45). Strikingly, I found that reduction of central plug. I therefore conclude that the central plugs are (at least partially) formed by IDP FG-Nups. Further, to investigate the feature of FG filaments and central plug in AKTP organoids, I monitored the in the presence of CHD by HS-AFM. Successive HS-AFM images showed the effect of 3% 1,2-hexanediol on the plugged NPC organoid (Figure 46). Consistently, for the first time, I also found the central plug was degraded after two hours CHD treatment with elapsed time and single FG Nup filaments started to appear clearly after central plug degradation (Figure 46c).



**Figure 45. Central plug degradation after CDH treatment.** Successive HS-AFM images showing the effect of 3% 1,2-hexanediol on the plugged NPC shown in I. Z-range is 12 nm, scanning speed is 2.5 frames per second, 200×200 pixels. The time-lapse imaging showing the degradation of the central plug by the 3% 1,2-hexanediol.

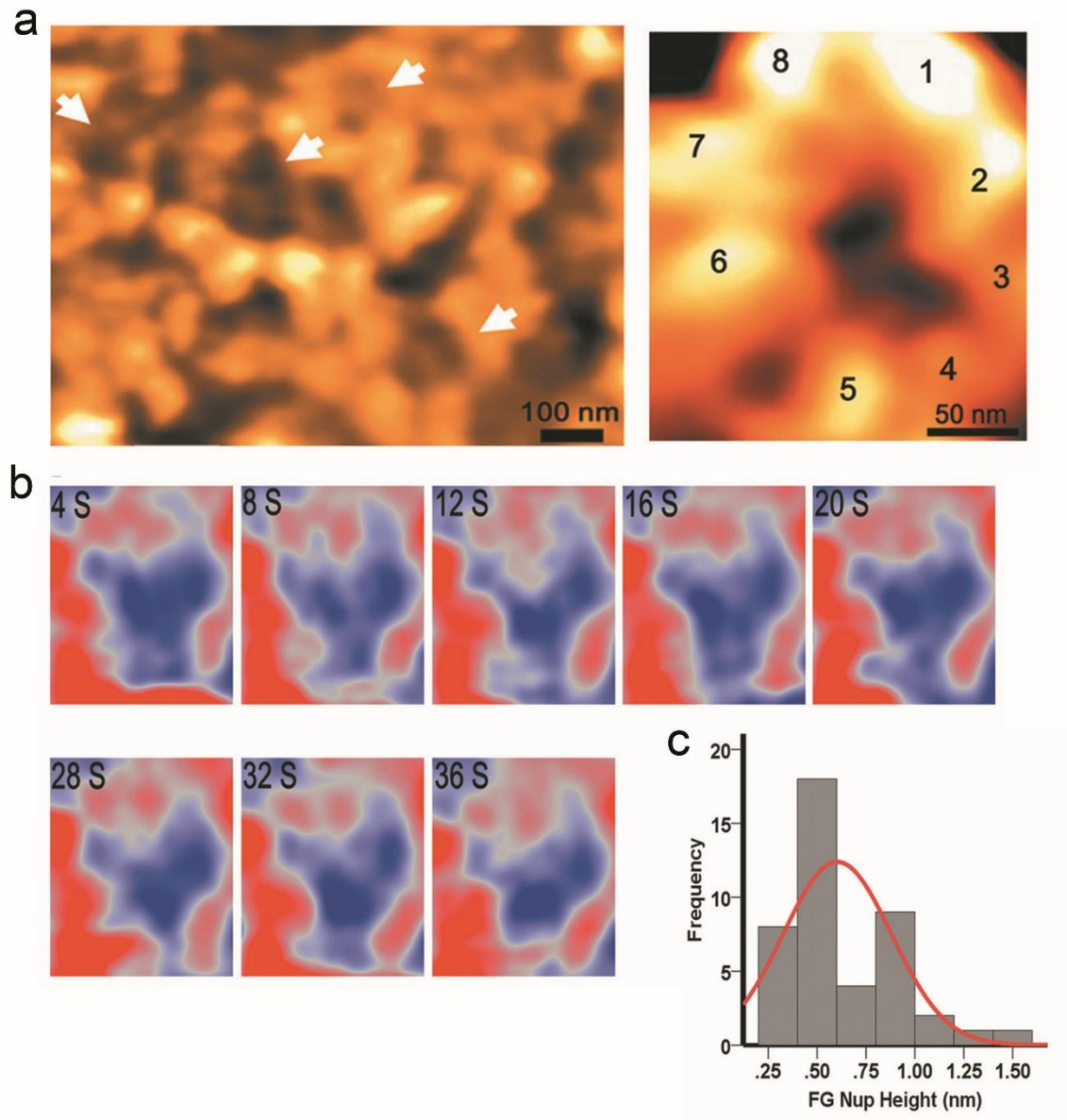


**Figure 46. Central plug degradation after CDH treatment in AKTP organoids.** (a) HS-AFM image of nuclear envelope surface with many globular NPCs. (b) Single NPC cropped from a. On the right panel HS-AFM image showing a plugged NPC. (c) The central plug degraded after adding CHD (yellow dotted circle). Under CHD treatment, single FG Nup filaments (yellow arrows) started to appear clearly after CP degradation.

Overall, our results reinforce the link between transient aggregation of FG-Nups proteins involved in central plug biogenesis and nucleocytoplasmic transport with human disease especially cancers. These results indicate that the central plugs in aggressive colon cancer cells have more dynamic motions than normal colon cells.

### **11. HS-AFM observation of shNUP214 KD-NPCs**

We established shRNA-mediated NUP214 KD cells and investigated their malignant phenotypes. Depletion of NUP214 prevented both anchorage-dependent and –independent cell growth. I asked whether the depletion of NUP214 can affect the FG selective barrier dynamics and distribution. So, I performed NPC observation by HS-AFM in shNUP214 cells, I found that the FG fibres in the inner channel have abnormal distributions. Also, the cytoplasmic filaments symmetric distribution is almost changed after NUP214 depletion (Figure 47).



**Figure 47. HS-AFM observation of shNUP24 KD NPCs.** (a) HS-AFM image of the cytoplasmic face of nuclear envelope of HCT116 cells Nup214 KO. Z-range is 15 nm, scanning speed is 0.4 frames per second, 200×200 pixels. White arrows referring to abnormal NPCs. The NPC shown on the right hand showing the abnormal structure of cytoplasmic filaments. (b) Successive HS-AFM images showing the FG Nups pattern after Nup214 KD. FG Nups distribution in highly affected. Z-range is 15 nm, scanning speed is 0.4 frames per second, 200×200 pixels. (c) Shows the normal distribution curve of FG Nup filaments height after Nup214 KO. FG Nup height is  $0.6 \pm 0.3$  nm (N=43).

## DISCUSSION

HS-AFM has been developed and involved as a strong tool for the imaging of single biomolecules in dynamic action at a high spatial-temporal resolution without changing their normal structure;(84) but the observation of live dynamics of intracellular organelles, such as the nucleus, is still very difficult because of the cantilever tip sizes and topology, native sample immobilization techniques and optimization, measurement conditions, and other nano-mechanical factors. In the current study, I directly visualized intact and drug-treated FG-Nup networks by HS-AFM in their native overall environments. The HS-AFM recordings and analysis showed that FG-Nups have a brush-like pattern, and I further proposed an entangled cobweb model to explain the process of central channel transport of different cargoes or gene gating by the NPC (85) (Figure 48).

Although many groups have tried to resolve the native structural dynamics of intrinsically disordered FG-Nup filaments and their dynamic conformational changes and interactions inside the intact NPC, to determine the mechanism of nucleocytoplasmic trafficking, but still unclear (86-88). Various models proposed, such as saturated hydrogel, virtual gate/polymer brush, the forest, and reduction of dimensionality, have been proposed based on previous experimental evidences and approaches. However, these models are not completely split-up from each other (Figure 49). The NPC selective barrier is believed to be an integral overall meshwork,(45). Here, I proposed an alternative cobweb model clarify the neglected factors by other previous models. First, I resolved the dynamic behaviour of the native NPCs from human colon cancer cells, which have a selective barrier. After that, I considered that the fast motions of FG-Nup filaments inside the NPC channel are strongly affected by the NPC scaffold arrangements. Also, these data showed that the FG-Nup filaments can change their thickness over the elapsed time as shown in HS-AFM recordings (Figure 30, 31), which suggested a different mechanism



from those explained in the previous models. In addition, our HS-AFM live imaging showed the existence of a central granule blocking some NPCs, for which most biophysical and dynamic deep information have yet to be invested (Figure 33).

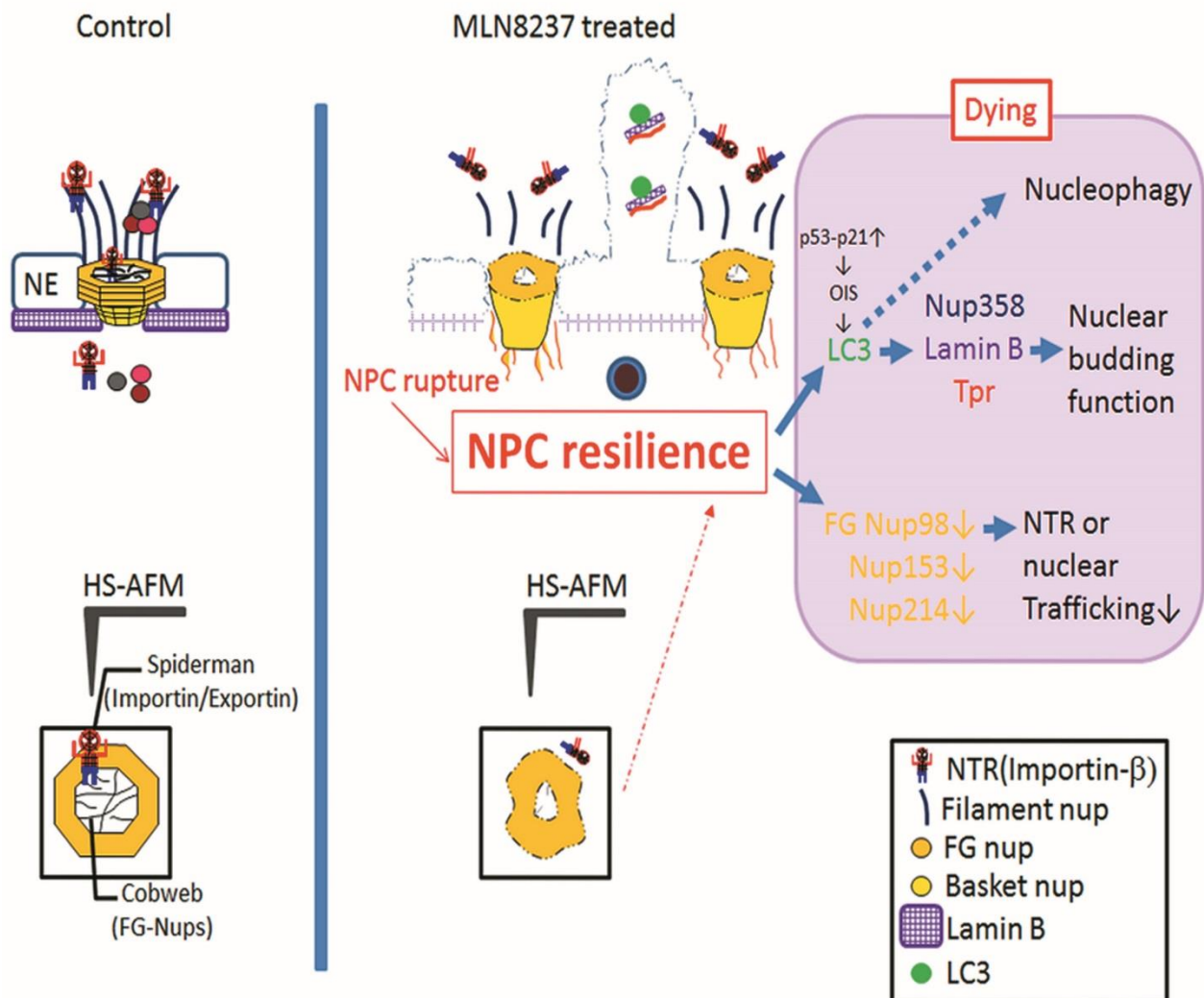
Even though the MLN8237 treatment results shown in Figure 29b and Figure 30c give an indication that the native pattern and conformations of these FG disordered proteins under some stress conditions, additional deep experimental investigations on this topic are needed. The current tentative cobweb model does not totally separated from the other proposed models (Figure 8 and Figure 49); the features of the complex cobweb network is similar to the main the virtual gating (83) and polymer brush(89, 90) models. Therewith, I showed the FG-Nup filaments twitching during their interaction with the central granule, as shown in Figure 33 a, and this pattern is not involved in the previous models (91-93).

Also, I showed the spontaneous native conformations of CP in cancer cells and organoid cells. CP appeared to block the NPC central channel. However, using FG-specific inhibitor resulted in the degradation of CP significantly in cancer 2D cells and converted the CP into fragmented filamentous structures featuring the FG Nup filamentous shape in 3D organoids.

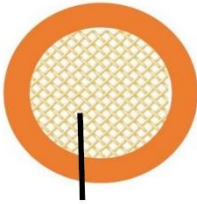
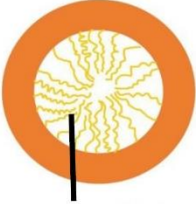

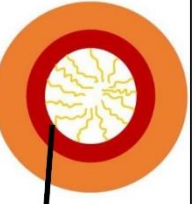
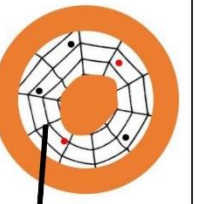
There are many evidences that the cellular activities which connected to tumorigenesis are dependent on the organization of the NE and NPC.(49, 94) Therefore, how the structure and function of NE/NPCs change in normal/healthy cells when they become tumour cells may directly contribute to tumorigenesis understanding. My current study of FG Nup patterns and dynamic behaviour in normal and cancer cells contribute not only to understanding their principal biomedical characteristics but also to developing promising diagnostic and therapeutic tools for colorectal cancer. Furthermore, Due to the

technical limits, IDP-FG single filament motions and dynamics still explained by the term of random motion or Brownian motion, because these single nano-filaments are highly dynamic, disordered and invisible in vitro. Thus, my current model is the a typical tentative biophysical model explaining the bending, extension and dynamic behaviour of single IDP-FG filaments in healthy and cancer cells based on typical experimental approaches. Therefore, my current model might open the door for many future advanced approaches to track the IDP-FG complexes in different species ([Figure 50](#)).





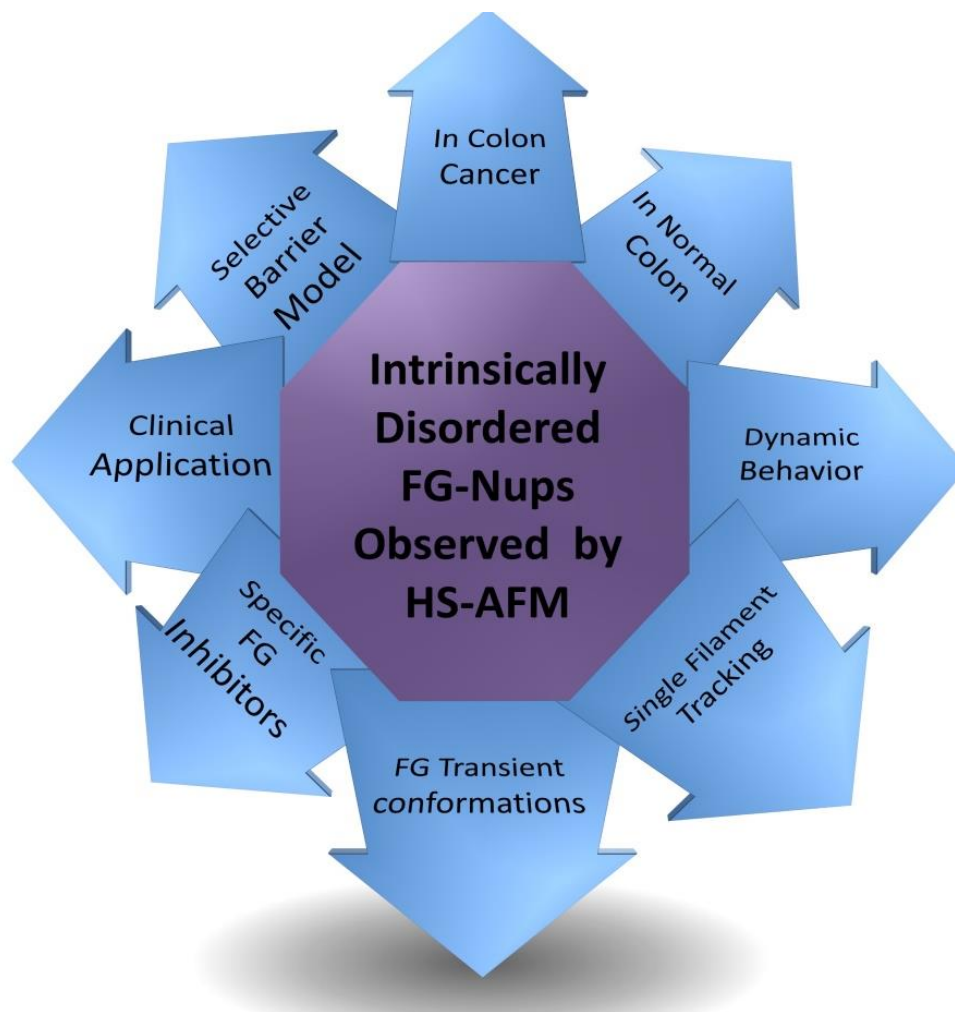
**Figure 48. Schematic illustration of the model that the loss of NPC resilience is an irreversible dying code.** Structurally, both the “brush model” and “hydrogel model” have been proposed for nuclear transport. I provide an alternative “spiderman-cobweb model” based on our HS-AFM observations (in millisecond scale). Nuclear transport factors (importins/exportins) act as “spidermen”, and the cobwebs are mainly composed of FG-Nups. The ultrafast nuclear translocation of cargo occurs by repelling inert material (>5 nm) or melts through the cobweb with waves of salt and pepper (Ran GTP gradient waves). Nuclear transport is assumed to occur in a nanosecond scale; owing to current technical limitations, ultrafast or super-resolution-AFM and other sensitive nanoassays need to be developed before we can validate our “spider-cobweb” hypothesis. Mechanistically, I showed NPC rupture and FG-Nup reduction, which enhanced the LC3 nuclear influx, facilitating the formation of LC3-Lamin B1-Nups subcomplexes and consequently boosting reversible nuclear budding. Unlike other conventional snapshot or static measurements of “average-out” imaging techniques, based on our direct observation *via* high-resolution live cell imaging and HS-AFM videos, I propose that the nanoscopic loss of NPC resilience is an irreversible dying code in cancer cells.

Model	Hydrogel	Virtual gating/ Polymer brush	Forest	Reduction of dimensionality	Cobweb
References	Frey S et al., 2006. Frey S & Gorlich DA, 2007. Frey S & Gorlich DA, 2009. And others.	Rout MP et al., 2000. Rout MP et al., 2003. Lim RY et al., 2007. Sakiyama Y. et al., 2016. And others.	Patel SS et al., 2007. And others.	Peters R, 2005. And others.	Current study.
Diagram	 Sieve-like meshwork	 Polymer brush	 Area 1 Area 2	 FG domain coat	 Cobweb FG network

**Figure 49. A schematic illustration of various Nucleocytoplasmic transport models.** This figure illustrates in a simple diagram-pattern the main differences between the previously proposed models and the current studied model. In the hydrogel model, FG-repeats form a homogenous sieve-like meshwork inside the central channel. In the virtual gating/polymer brush model, FG-Nups extend inside the central channel as repulsive bristles or polymer brushes composing an entropic barrier. In the forest model, a two-gate model of NPC is proposed, in which a central diffusion gate composed of cohesive FG-Nup filaments (Area 1) and a peripheral gate composed by repulsive FG-Nup filaments (Area 2). In the reduction of dimensionality model, FG domains continuously form an inner coat (Red inner layer) on the inner wall of the NPC to provide a continuous site for NTRs and cargos. Reference *Weidong Yang, Nucleus, 2:1, 10-16 (2011)*.

## CONCLUSIONS

In the current study, HS-AFM movies strongly consistent with the hypothesis that the resilience of individual FG-Nups is lost in the dying nuclei of colorectal cancer cells, which facilitates nuclear deformation and blebbing. As a conclusion, by mainly using HS-AFM movies and other imaging methods with an inhibitor of Aurora A in human colorectal cancer cells, I determined and visualized that the loss of the nanoscopic structural conformations of NPC FG-Nups barrier is another hallmark or a dying code in cancer cells. The current HS-AFM observations of native FG Nups provide a tentative explanation of the biophysical motion model of FG Nups inside the central channel. The current data explain how the single FG filaments form the central selective network. Furthermore, this model explains how the IDP-FG Nups turnover from one state to another on in the native NPCs. Also, this model revealed that IDP-FG filaments under certain conditions, twist over each other to form a thick aggregate which gradually may form a central granule. Taken together, these results unveiled different nano characteristics of FG Nups in different mammalian cells.



**Figure 50. HS-AFM resolved FG Nups behaviour.** Diagram showing different IDP-FG Nup unknown characteristics that could be partially resolved by HS-AFM in the current study.

## REFERENCES

- 1- Hayama, R., M. P. Rout and J. Fernandez-Martinez (2017). "The nuclear pore complex core scaffold and permeability barrier: variations of a common theme." *Curr Opin Cell Biol* 46: 110-118.
- 2- Fernandez-Martinez, J., S. J. Kim, Y. Shi, P. Upla, R. Pellarin, M. Gagnon, I. E. Chemmama, J. Wang, I. Nudelman, W. Zhang, R. Williams, W. J. Rice, D. L. Stokes, D. Zenklusen, B. T. Chait, A. Sali and M. P. Rout (2016). "Structure and Function of the Nuclear Pore Complex Cytoplasmic mRNA Export Platform." *Cell* 167(5): 1215-1228 e1225.
- 3- Denning, D. P., S. S. Patel, V. Uversky, A. L. Fink and M. Rexach (2003). "Disorder in the nuclear pore complex: the FG repeat regions of nucleoporins are natively unfolded." *Proc Natl Acad Sci U S A* 100(5): 2450-2455.
- 4- Tu, L. C. and S. M. Musser (2011). "Single molecule studies of nucleocytoplasmic transport." *Biochim Biophys Acta* 1813(9): 1607-1618.
- 5- Lusk, C. P. and M. C. King (2017). "The nucleus: keeping it together by keeping it apart." *Curr Opin Cell Biol* 44: 44-50.
- 6- Mosalaganti, S., J. Kosinski, S. Albert, M. Schaffer, D. Strenkert, P. A. Salome, S. S. Merchant, J. M. Plitzko, W. Baumeister, B. D. Engel and M. Beck (2018). "In situ architecture of the algal nuclear pore complex." *Nat Commun* 9(1): 2361.
- 7- Bernhofer, M., T. Goldberg, S. Wolf, M. Ahmed, J. Zaugg, M. Boden and B. Rost (2018). "NLSdb-major update for database of nuclear localization signals and nuclear export signals." *Nucleic Acids Res* 46(D1): D503-D508.
- 8- Cook, A., F. Bono, M. Jinek and E. Conti (2007). "Structural biology of nucleocytoplasmic transport." *Annu Rev Biochem* 76: 647-671.
- 9- Twyffels, L., C. Gueydan and V. Kruys (2014). "Transportin-1 and Transportin-2: protein nuclear import and beyond." *FEBS Lett* 588(10): 1857-1868.
- 10- Kapinos, L. E., R. L. Schoch, R. S. Wagner, K. D. Schleicher and R. Y. Lim (2014). "Karyopherin-centric control of nuclear pores based on molecular occupancy and kinetic analysis of multivalent binding with FG nucleoporins." *Biophys J* 106(8): 1751-1762.
- 11- Stewart, M. (2007). "Molecular mechanism of the nuclear protein import cycle." *Nat Rev Mol Cell Biol* 8(3): 195-208.
- 12- Katahira, J. (2012). "mRNA export and the TREX complex." *Biochim Biophys Acta* 1819(6): 507-513.
- 13- Frenkiel-Krispin, D., B. Maco, U. Aebi and O. Medalia (2010). "Structural analysis of a metazoan nuclear pore complex reveals a fused concentric ring architecture." *J Mol Biol* 395(3): 578-586.
- 14- Eibauer, M., M. Pellanda, Y. Turgay, A. Dubrovsky, A. Wild and O. Medalia (2015). "Structure and gating of the nuclear pore complex." *Nat Commun* 6: 7532.
- 15- Bui, K. H., A. von Appen, A. L. DiGuilio, A. Ori, L. Sparks, M. T. Mackmull, T. Bock, W. Hagen, A. Andres-Pons, J. S. Glavy and M. Beck (2013). "Integrated structural analysis of the human nuclear pore complex scaffold." *Cell* 155(6): 1233-1243.

- 16- Grossman, E., O. Medalia and M. Zwerger (2012). "Functional architecture of the nuclear pore complex." *Annu Rev Biophys* 41: 557-584.
- 17- Maimon, T., N. Elad, I. Dahan and O. Medalia (2012). "The human nuclear pore complex as revealed by cryo-electron tomography." *Structure* 20(6): 998-1006.
- 18- Terry, L. J. and S. R. Wente (2009). "Flexible gates: dynamic topologies and functions for FG nucleoporins in nucleocytoplasmic transport." *Eukaryot Cell* 8(12): 1814-1827.
- 19- Zwerger, M., M. Eibauer and O. Medalia (2016). "Insights into the gate of the nuclear pore complex." *Nucleus* 7(1): 1-7.
- 20- Patel, S. S., B. J. Belmont, J. M. Sante and M. F. Rexach (2007). "Natively unfolded nucleoporins gate protein diffusion across the nuclear pore complex." *Cell* 129(1): 83-96.
- 21- Peters, R. (2005). "Translocation through the nuclear pore complex: selectivity and speed by reduction-of-dimensionality." *Traffic* 6(5): 421-427.
- 22- Rout, M. (2003). "Virtual gating and nuclear transport: the hole picture." *Trends in Cell Biology* 13(12): 622-628.
- 23- Hulsmann, B. B., A. A. Labokha and D. Gorlich (2012). "The permeability of reconstituted nuclear pores provides direct evidence for the selective phase model." *Cell* 150(4): 738-751.
- 24- Labokha, A. A., S. Gradmann, S. Frey, B. B. Hulsmann, H. Urlaub, M. Baldus and D. Gorlich (2013). "Systematic analysis of barrier-forming FG hydrogels from *Xenopus* nuclear pore complexes." *EMBO J* 32(2): 204-218.
- 25- Atkinson, C. E., A. L. Mattheyses, M. Kampmann and S. M. Simon (2013). "Conserved spatial organization of FG domains in the nuclear pore complex." *Biophys J* 104(1): 37-50.
- 26- Mohamed, M. S., A. Kobayashi, A. Taoka, T. Watanabe-Nakayama, Y. Kikuchi, M. Hazawa, T. Minamoto, Y. Fukumori, N. Kodera, T. Uchihashi, T. Ando and R. W. Wong (2017). "High-Speed Atomic Force Microscopy Reveals Loss of Nuclear Pore Resilience as a Dying Code in Colorectal Cancer Cells." *ACS Nano* 11(6): 5567-5578.
- 27- Hoelz, A., J. S. Glavy and M. Beck (2016). "Toward the atomic structure of the nuclear pore complex: when top down meets bottom up." *Nat Struct Mol Biol* 23(7): 624-630.
- 28- Stoffler, D., B. Feja, B. Fahrenkrog, J. Walz, D. Typke and U. Aebi (2003). "Cryo-electron Tomography Provides Novel Insights into Nuclear Pore Architecture: Implications for Nucleocytoplasmic Transport." *Journal of Molecular Biology* 328(1): 119-130.
- 29- Beck, M., V. Lucic, F. Forster, W. Baumeister and O. Medalia (2007). "Snapshots of nuclear pore complexes in action captured by cryo-electron tomography." *Nature* 449(7162): 611-615.
- 30- Toda, T., J. Y. Hsu, S. B. Linker, L. Hu, S. T. Schafer, J. Mertens, F. V. Jacinto, M. W. Hetzer and F. H. Gage (2017). "Nup153 Interacts with Sox2 to Enable Bimodal Gene Regulation and Maintenance of Neural Progenitor Cells." *Cell Stem Cell* 21(5): 618-634 e617.

- 31- Paulillo, S. M., E. M. Phillips, J. Koser, U. Sauder, K. S. Ullman, M. A. Powers and B. Fahrenkrog (2005). "Nucleoporin domain topology is linked to the transport status of the nuclear pore complex." *J Mol Biol* 351(4): 784-798.
- 32- Ben-Yishay, R., A. J. Ashkenazy and Y. Shav-Tal (2016). "Dynamic Encounters of Genes and Transcripts with the Nuclear Pore." *Trends Genet* 32(7): 419-431.
- 33- Walther, T. C., H. S. Pickersgill, V. C. Cordes, M. W. Goldberg, T. D. Allen, I. W. Mattaj and M. Fornerod (2002). "The cytoplasmic filaments of the nuclear pore complex are dispensable for selective nuclear protein import." *J Cell Biol* 158(1): 63-77.
- 34- Zeitler, B. and K. Weis (2004). "The FG-repeat asymmetry of the nuclear pore complex is dispensable for bulk nucleocytoplasmic transport in vivo." *J Cell Biol* 167(4): 583-590.
- 35- Rabut, G., V. Doye and J. Ellenberg (2004). "Mapping the dynamic organization of the nuclear pore complex inside single living cells." *Nat Cell Biol* 6(11): 1114-1121.
- 36- Griffis, E. R., N. Altan, J. Lippincott-Schwartz and M. A. Powers (2002). "Nup98 is a mobile nucleoporin with transcription-dependent dynamics." *Mol Biol Cell* 13(4): 1282-1297.
- 37- Knockenhauer, K. E. and T. U. Schwartz (2016). "The Nuclear Pore Complex as a Flexible and Dynamic Gate." *Cell* 164(6): 1162-1171.
- 38- Dange, T., D. Grunwald, A. Grunwald, R. Peters and U. Kubitschek (2008). "Autonomy and robustness of translocation through the nuclear pore complex: a single-molecule study." *J Cell Biol* 183(1): 77-86.
- 39- Chatel, G., S. H. Desai, A. L. Mattheyses, M. A. Powers and B. Fahrenkrog (2012). "Domain topology of nucleoporin Nup98 within the nuclear pore complex." *J Struct Biol* 177(1): 81-89.
- 40- Stolz, M., D. Stoffler, U. Aebi, B. Goldsbury (2014). "Monitoring biomolecular interactions by time-lapse atomic force microscopy." *J Struct Biol* 131(3): 171-80.
- 41- Bestembayeva, A., A. Kramer, A. A. Labokha, D. Osmanovic, I. Liashkovich, E. V. Orlova, I. J. Ford, G. Charras, A. Fassati and B. W. Hoogenboom (2015). "Nanoscale stiffness topography reveals structure and mechanics of the transport barrier in intact nuclear pore complexes." *Nat Nanotechnol* 10(1): 60-64.
- 42- Kramer, A., I. Liashkovich, Y. Ludwig and V. Shahin (2008). "Atomic force microscopy visualises a hydrophobic meshwork in the central channel of the nuclear pore." *Pflugers Arch* 456(1): 155-162.
- 43- Cardarelli, F., L. Lanzano and E. Gratton (2012). "Capturing directed molecular motion in the nuclear pore complex of live cells." *Proc Natl Acad Sci U S A* 109(25): 9863-9868.
- 44- Ma, J., A. Goryaynov, A. Sarma and W. Yang (2012). "Self-regulated viscous channel in the nuclear pore complex." *Proc Natl Acad Sci U S A* 109(19): 7326-7331.
- 45- Ando, T., T. Uchihashi, N. Kodera, D. Yamamoto, A. Miyagi, M. Taniguchi and H. Yamashita (2008). "High-speed AFM and nano-visualization of biomolecular processes." *Pflugers Arch* 456(1): 211-225.



- 46- Uchihashi, T., N. Kodera and T. Ando (2012). "Guide to video recording of structure dynamics and dynamic processes of proteins by high-speed atomic force microscopy." *Nat Protoc* 7(6): 1193-1206.
- 47- Uchihashi, T., R. Iino, T. Ando and H. Noji (2011). "High-speed atomic force microscopy reveals rotary catalysis of rotorless F(1)-ATPase." *Science* 333(6043): 755-758.
- 48- Miyagi, A., Y. Tsunaka, T. Uchihashi, K. Mayanagi, S. Hirose, K. Morikawa and T. Ando (2008). "Visualization of intrinsically disordered regions of proteins by high-speed atomic force microscopy." *Chemphyschem* 9(13): 1859-1866.
- 49- Funasaka, T. and R. W. Wong (2011). "The role of nuclear pore complex in tumor microenvironment and metastasis." *Cancer Metastasis Rev* 30(2): 239-251.
- 50- Panagiotakopoulou, M., M. Bergert, A. Taubenberger, J. Guck, D. Poulidakos and A. Ferrari (2016). "A Nanoprinted Model of Interstitial Cancer Migration Reveals a Link between Cell Deformability and Proliferation." *ACS Nano* 10(7): 6437-6448.
- 51- Chin, K., S. DeVries, J. Fridlyand, P. T. Spellman, R. Roydasgupta, W. L. Kuo, A. Lapuk, R. M. Neve, Z. Qian, T. Ryder, F. Chen, H. Feiler, T. Tokuyasu, C. Kingsley, S. Dairkee, Z. Meng, K. Chew, D. Pinkel, A. Jain, B. M. Ljung, L. Esserman, D. G. Albertson, F. M. Waldman and J. W. Gray (2006). "Genomic and transcriptional aberrations linked to breast cancer pathophysiologies." *Cancer Cell* 10(6): 529-541.
- 52- Moore, M. A. (2010). "A cancer fate in the hands of a samurai." *Nat Med* 16(9): 963-965.
- 53- Moore, M. A., K. Y. Chung, M. Plasilova, J. J. Schuringa, J. H. Shieh, P. Zhou and G. Morrone (2007). "NUP98 dysregulation in myeloid leukemogenesis." *Ann N Y Acad Sci* 1106: 114-142.
- 54- Moore, M. A. (2005). "Converging pathways in leukemogenesis and stem cell self-renewal." *Exp Hematol* 33(7): 719-737.
- 55- Shibata, M., T. Uchihashi, T. Ando and R. Yasuda (2015). "Long-tip high-speed atomic force microscopy for nanometer-scale imaging in live cells." *Sci Rep* 5: 8724.
- 56- Ando, T., T. Uchihashi and S. Scheuring (2014). "Filming biomolecular processes by high-speed atomic force microscopy." *Chem Rev* 114(6): 3120-3188.
- 57- Drouet, Y., I. Treilleux, A. Viari, S. Leon, M. Devouassoux-Shisheboran, N. Voirin, C. de la Fouchardiere, B. Manship, A. Puisieux, C. Lasset and C. Moyret-Lalle (2018). "Integrated analysis highlights APC11 protein expression as a likely new independent predictive marker for colorectal cancer." *Sci Rep* 8(1): 7386.
- 58- Ahmed, D., P. W. Eide, I. A. Eilertsen, S. A. Danielsen, M. Eknaes, M. Hektoen, G. E. Lind and R. A. Lothe (2013). "Epigenetic and genetic features of 24 colon cancer cell lines." *Oncogenesis* 2: e71.
- 59- Kobayashi, A., C. Hashizume, T. Dowaki and R. W. Wong (2015). "Therapeutic potential of mitotic interaction between the nucleoporin Tpr and aurora kinase A." *Cell Cycle* 14(9): 1447-1458.
- 60- Hashizume, C., A. Kobayashi and R. W. Wong (2013). "Down-modulation of nucleoporin RanBP2/Nup358 impaired chromosomal alignment and induced mitotic catastrophe." *Cell Death Dis* 4: e854.

- 61- Walde, S., K. Thakar, S. Hutten, C. Spillner, A. Nath, U. Rothbauer, S. Wiemann and R. H. Kehlenbach (2012). "The nucleoporin Nup358/RanBP2 promotes nuclear import in a cargo- and transport receptor-specific manner." *Traffic* 13(2): 218-233.
- 62- Hashizume, C., A. Moyori, A. Kobayashi, N. Yamakoshi, A. Endo and R. W. Wong (2013). "Nucleoporin Nup62 maintains centrosome homeostasis." *Cell Cycle* 12(24): 3804-3816.
- 63- Nakano, H., T. Funasaka, C. Hashizume and R. W. Wong (2010). "Nucleoporin translocated promoter region (Tpr) associates with dynein complex, preventing chromosome lagging formation during mitosis." *J Biol Chem* 285(14): 10841-10849.
- 64- Funasaka, T., E. Tsuka and R. W. Wong (2012). "Regulation of autophagy by nucleoporin Tpr." *Sci Rep* 2: 878.
- 65- Sakiyama, Y., A. Mazur, L. E. Kapinos and R. Y. Lim (2016). "Spatiotemporal dynamics of the nuclear pore complex transport barrier resolved by high-speed atomic force microscopy." *Nat Nanotechnol* 11(8): 719-723.
- 66- Elad, N., T. Maimon, D. Frenkiel-Krispin, R. Y. Lim and O. Medalia (2009). "Structural analysis of the nuclear pore complex by integrated approaches." *Curr Opin Struct Biol* 19(2): 226-232.
- 67- Beck, M. and E. Hurt (2017). "The nuclear pore complex: understanding its function through structural insight." *Nat Rev Mol Cell Biol* 18(2): 73-89.
- 68- Taylor, J. P. (2017). "A PR plug for the nuclear pore in amyotrophic lateral sclerosis." *Proc Natl Acad Sci U S A* 114(7): 1445-1447.
- 69- Shi, K. Y., E. Mori, Z. F. Nizami, Y. Lin, M. Kato, S. Xiang, L. C. Wu, M. Ding, Y. Yu, J. G. Gall and S. L. McKnight (2017). "Toxic PRn poly-dipeptides encoded by the C9orf72 repeat expansion block nuclear import and export." *Proc Natl Acad Sci U S A* 114(7): E1111-E1117.
- 70- Asally, M., Y. Yasuda, M. Oka, S. Otsuka, S. H. Yoshimura, K. Takeyasu and Y. Yoneda (2011). "Nup358, a nucleoporin, functions as a key determinant of the nuclear pore complex structure remodeling during skeletal myogenesis." *FEBS J* 278(4): 610-621.
- 71- Perez-Terzic, C., A. Behfar, A. Mery, J. M. van Deursen, A. Terzic and M. Puceat (2003). "Structural adaptation of the nuclear pore complex in stem cell-derived cardiomyocytes." *Circ Res* 92(4): 444-452.
- 72- Faustino, R. S., A. Behfar, J. Groenendyk, S. P. Wyles, N. Niederlander, S. Reyes, M. Puceat, M. Michalak, A. Terzic and C. Perez-Terzic (2016). "Calreticulin secures calcium-dependent nuclear pore competency required for cardiogenesis." *J Mol Cell Cardiol* 92: 63-74.
- 73- Venkatakrishnan, K., X. Zhou, J. Ecsedy, D. R. Mould, H. Liu, H. Danaee, H. Fingert, R. Kleinfeld and A. Milton (2015). "Dose selection for the investigational anticancer agent alisertib (MLN8237): Pharmacokinetics, pharmacodynamics, and exposure-safety relationships." *J Clin Pharmacol* 55(3): 336-347.
- 74- Melichar, B., A. Adenis, A. C. Lockhart, J. Bennouna, E. C. Dees, O. Kayaleh, R. Obermannova, A. DeMichele, P. Zatloukal, B. Zhang, C. D. Ullmann and C. Schusterbauer (2015). "Safety and activity of alisertib, an investigational aurora kinase A inhibitor, in patients with breast cancer, small-cell lung cancer, non-small-

- cell lung cancer, head and neck squamous-cell carcinoma, and gastro-oesophageal adenocarcinoma: a five-arm phase 2 study." *The Lancet Oncology* 16(4): 395-405.
- 75- Manfredi, M. G., J. A. Ecsedy, A. Chakravarty, L. Silverman, M. Zhang, K. M. Hoar, S. G. Stroud, W. Chen, V. Shinde, J. J. Huck, D. R. Wysong, D. A. Janowick, M. L. Hyer, P. J. Leroy, R. E. Gershman, M. D. Silva, M. S. Germanos, J. B. Bolen, C. F. Claiborne and T. B. Sells (2011). "Characterization of Alisertib (MLN8237), an investigational small-molecule inhibitor of aurora A kinase using novel in vivo pharmacodynamic assays." *Clin Cancer Res* 17(24): 7614-7624.
  - 76- Frey, S. and D. Gorlich (2007). "A saturated FG-repeat hydrogel can reproduce the permeability properties of nuclear pore complexes." *Cell* 130(3): 512-523.
  - 77- Kramer, A., I. Liashkovich, H. Oberleithner, S. Ludwig, I. Mazur and V. Shahin (2008). "Apoptosis leads to a degradation of vital components of active nuclear transport and a dissociation of the nuclear lamina." *Proc Natl Acad Sci U S A* 105(32): 11236-11241.
  - 78- Larsson, L. G. (2011). "Oncogene- and tumor suppressor gene-mediated suppression of cellular senescence." *Semin Cancer Biol* 21(6): 367-376.
  - 79- Kim, K. S., K. W. Kang, Y. B. Seu, S. H. Baek and J. R. Kim (2009). "Interferon-gamma induces cellular senescence through p53-dependent DNA damage signaling in human endothelial cells." *Mech Ageing Dev* 130(3): 179-188.
  - 80- Denais, C. M., R. M. Gilbert, P. Isermann, A. L. McGregor, M. te Lindert, B. Weigelin, P. M. Davidson, P. Friedl, K. Wolf and J. Lammerding (2016). "Nuclear envelope rupture and repair during cancer cell migration." *Science* 352(6283): 353-358.
  - 81- Vovk, A., C. Gu, M. G. Opferman, L. E. Kapinos, R. Y. Lim, R. D. Coalson, D. Jasnow and A. Zilman (2016). "Simple biophysics underpins collective conformations of the intrinsically disordered proteins of the Nuclear Pore Complex." *Elife* 5.
  - 82- Zhu, Y., H. Zeng, J. Xie, L. Ba, X. Gao and Z. Lu (2004). "Atomic force microscopy studies on DNA structural changes induced by vincristine sulfate and aspirin." *Microsc Microanal* 10(2): 286-290.
  - 83- Powers, M. A. and D. J. Forbes (2012). "Nuclear transport: beginning to gel?" *Curr Biol* 22(23): R1006-1009.
  - 84- Ando, T. (2014). "High-speed AFM imaging." *Curr Opin Struct Biol* 28: 63-68.
  - 85- Manhas, S., L. Ma and V. Measday (2018). "The yeast Ty1 retrotransposon requires components of the nuclear pore complex for transcription and genomic integration." *Nucleic Acids Res* 46(7): 3552-3578.
  - 86- Yang, W. (2011). "'Natively unfolded' nucleoporins in nucleocytoplasmic transport: clustered or evenly distributed?" *Nucleus* 2(1): 10-16.
  - 87- Weis, K. (2007). "The nuclear pore complex: oily spaghetti or gummy bear?" *Cell* 130(3): 405-407.
  - 88- Schmidt, H. B. and D. Gorlich (2016). "Transport Selectivity of Nuclear Pores, Phase Separation, and Membraneless Organelles." *Trends Biochem Sci* 41(1): 46-61.
  - 89- Lim, R. Y., N. P. Huang, J. Koser, J. Deng, K. H. Lau, K. Schwarz-Herion, B. Fahrenkrog and U. Aebi (2006). "Flexible phenylalanine-glycine nucleoporins as

- entropic barriers to nucleocytoplasmic transport." *Proc Natl Acad Sci U S A* 103(25): 9512-9517.
- 90- Hough, L. E., K. Dutta, S. Sparks, D. B. Temel, A. Kamal, J. Tetenbaum-Novatt, M. P. Rout and D. Cowburn (2015). "The molecular mechanism of nuclear transport revealed by atomic-scale measurements." *Elife* 4.
  - 91- Chattopadhyay, K., E. L. Elson and C. Frieden (2005). "The kinetics of conformational fluctuations in an unfolded protein measured by fluorescence methods." *Proc Natl Acad Sci U S A* 102(7): 2385-2389.
  - 92- Adams, J. D., B. W. Erickson, J. Grossenbacher, J. Brugger, A. Nievergelt and G. E. Fantner (2016). "Harnessing the damping properties of materials for high-speed atomic force microscopy." *Nat Nanotechnol* 11(2): 147-151.
  - 93- Moussavi-Baygi, R. and M. R. Mofrad (2016). "Rapid Brownian Motion Primes Ultrafast Reconstruction of Intrinsically Disordered Phe-Gly Repeats Inside the Nuclear Pore Complex." *Sci Rep* 6: 29991.
  - 94- Di Nunzio, F., A. Danckaert, T. Fricke, P. Perez, J. Fernandez, E. Perret, P. Roux, S. Shorte, P. Charneau, F. Diaz-Griffero and N. J. Arhel (2012). "Human nucleoporins promote HIV-1 docking at the nuclear pore, nuclear import and integration." *PLoS One* 7(9): e46037.
  - 95- Diguilio, A. L. and J. S. Glavy (2013). "Depletion of nucleoporins from HeLa nuclear pore complexes to facilitate the production of ghost pores for in vitro reconstitution." *Cytotechnology* 65(4): 469-479.
  - 96- Uversky, V. N., C. J. Oldfield and A. K. Dunker (2008). "Intrinsically disordered proteins in human diseases: introducing the D2 concept." *Annu Rev Biophys* 37: 215-246.
  - 97- Wright, P. E. and H. J. Dyson (2015). "Intrinsically disordered proteins in cellular signalling and regulation." *Nat Rev Mol Cell Biol* 16(1): 18-29.
  - 98- Fong, J. H., B. A. Shoemaker and A. R. Panchenko (2012). "Intrinsic protein disorder in human pathways." *Mol Biosyst* 8(1): 320-326.
  - 99- Gsponer, J. and M. M. Babu (2009). "The rules of disorder or why disorder rules." *Prog Biophys Mol Biol* 99(2-3): 94-103.
  - 100- Malaney, P., R. R. Pathak, B. Xue, V. N. Uversky and V. Dave (2013). "Intrinsic disorder in PTEN and its interactome confers structural plasticity and functional versatility." *Sci Rep* 3: 2035.
  - 101- Vucetic, S., H. Xie, L. M. Iakoucheva, C. J. Oldfield, A. K. Dunker, Z. Obradovic and V. N. Uversky (2007). "Functional anthology of intrinsic disorder. 2. Cellular components, domains, technical terms, developmental processes, and coding sequence diversities correlated with long disordered regions." *J Proteome Res* 6(5): 1899-1916.
  - 102- Xie, H., S. Vucetic, L. M. Iakoucheva, C. J. Oldfield, A. K. Dunker, Z. Obradovic and V. N. Uversky (2007). "Functional anthology of intrinsic disorder. 3. Ligands, post-translational modifications, and diseases associated with intrinsically disordered proteins." *J Proteome Res* 6(5): 1917-1932.
  - 103- Uversky, V. N. and A. L. Fink (2004). "Conformational constraints for amyloid fibrillation: the importance of being unfolded." *Biochim Biophys Acta* 1698(2): 131-153.

- 104- Dyson, H. J. and P. E. Wright (2005). "Intrinsically unstructured proteins and their functions." *Nat Rev Mol Cell Biol* 6(3): 197-208.
- 105- Wells, M., H. Tidow, T. J. Rutherford, P. Markwick, M. R. Jensen, E. Mylonas, D. I. Svergun, M. Blackledge and A. R. Fersht (2008). "Structure of tumor suppressor p53 and its intrinsically disordered N-terminal transactivation domain." *Proc Natl Acad Sci U S A* 105(15): 5762-5767.
- 106- Mark, W. Y., J. C. Liao, Y. Lu, A. Ayed, R. Laister, B. Szymczyna, A. Chakrabartty and C. H. Arrowsmith (2005). "Characterization of segments from the central region of BRCA1: an intrinsically disordered scaffold for multiple protein-protein and protein-DNA interactions?" *J Mol Biol* 345(2): 275-287.
- 107- Tamarozzi, E. R. and S. Giuliatti (2018). "Understanding the Role of Intrinsic Disorder of Viral Proteins in the Oncogenicity of Different Types of HPV." *Int J Mol Sci* 19(1).
- 108- Uversky, V. N., V. Dave, L. M. Iakoucheva, P. Malaney, S. J. Metallo, R. R. Pathak and A. C. Joerger (2014). "Pathological unfoldomics of uncontrolled chaos: intrinsically disordered proteins and human diseases." *Chem Rev* 114(13): 6844-6879.
- 109- Rajagopalan, K., S. M. Mooney, N. Parekh, R. H. Getzenberg and P. Kulkarni (2011). "A majority of the cancer/testis antigens are intrinsically disordered proteins." *J Cell Biochem* 112(11): 3256-3267.
- 110- Denning, D. P., S. S. Patel, V. Uversky, A. L. Fink and M. Rexach (2003). "Disorder in the nuclear pore complex: the FG repeat regions of nucleoporins are natively unfolded." *Proc Natl Acad Sci U S A* 100(5): 2450-2455.
- 111- Ader, C., S. Frey, W. Maas, H. B. Schmidt, D. Gorlich and M. Baldus (2010). "Amyloid-like interactions within nucleoporin FG hydrogels." *Proc Natl Acad Sci U S A* 107(14): 6281-6285.
- 112- Milles, S., K. Huy Bui, C. Koehler, M. Eltsov, M. Beck and E. A. Lemke (2013). "Facilitated aggregation of FG nucleoporins under molecular crowding conditions." *EMBO Rep* 14(2): 178-183.
- 113- Kowalczyk, S. W., L. Kapinos, T. R. Blosser, T. Magalhaes, P. van Nies, R. Y. Lim and C. Dekker (2011). "Single-molecule transport across an individual biomimetic nuclear pore complex." *Nat Nanotechnol* 6(7): 433-438.
- 114- Jovanovic-Taliman, T., J. Tetenbaum-Novatt, A. S. McKenney, A. Zilman, R. Peters, M. P. Rout and B. T. Chait (2009). "Artificial nanopores that mimic the transport selectivity of the nuclear pore complex." *Nature* 457(7232): 1023-1027.